# Spectral properties of adsorbates on metal surfaces via the embedding method


Simona Achilli

Department of Materials Science

University of Milan Bicocca

A thesis submitted for the degree of

*Dottore di ricerca*

3 May 2010

I would like to dedicate this thesis to my little Samuele.

# Contents

# Introduction

Surfaces, thin films and low dimensional systems represent a favourable scenario for physical phenomena of practical and fundamental interest.

In general solid-solid or solid-vacuum interfaces are the preferred context for chemical reactions, atomic rearrangement, diffusion. The surface is in addition the place where the interaction of the solid with the external realizes, for example through the creation of chemical bonding that is at the basis of many fundamental phenomena like nucleation, layer's growth, catalysis and others.

Among the factors that influence the surface specific phenomena, the electronic properties play a fundamental role. Indeed the electronic states of the system reflect the chemical nature of the constituent elements, their spatial extent and mutual interaction, and they have an active part in determining the physical properties. In particular when an interface is created, the electronic properties can change considerably with respect to the bulk case.

The primary point is that at the surface new electronic states arise, whose propagation in the bulk is prevented. Due to the spatial localization normal to the surface of their wave-function these states are sensitive to the chemical environment in proximity of the surface and they are strongly affected by the interaction with different external systems.

A challenging situation in which such interaction occurs is represented for example by the gradual growth of a thin film on a surface. Since the adsorption of a single atom up to the completion of one monolayer, the electronic properties of the system evolve continuously and the most evident changes pertain to the surface states.

The surface states have also an active role in electron-dynamics, being usually the channel for the electronic transport and for the decay processes involving

electrons. The efficiency of the surface state mediated processes depends on the lifetime of such states, i.e. on the time spent by the electrons on them. For the surface features this time can be considerably long, so that they can act as transient states in a large variety of phenomena.

These peculiarities make surface states suitable for applications in electronic devices and motivated their increasing relevance in the field of nano-physics.

The detailed understanding of the electronic properties of low dimensional systems in general is of primary importance in forming a coherent view of the interface phenomena and their perspective of application. During the last decades an intensive scientific research both experimental and theoretical has been devoted to surfaces and thin films.

Although accurate experimental techniques have been developed, the experimental results are often of difficult interpretation. For example the coexistence of many factors, sometimes not easily distinguishable, that contribute to the investigated properties can hinder an immediate understanding of the measured quantities.

On the other hand the theoretical analysis has been hindered by the great computational effort required for a realistic description of such complex systems. Electronic structure calculations suffer indeed from the reduced symmetry of the system that prevents the application of the Bloch condition, requiring an integration of the Schrödinger equation over an infinite volume. In addition the treatment of the electron-electron interaction constitutes a demanding task.

In order to deal with such difficulties many strategies and methods have been developed. For what concerns the electron-electron interaction, the Hartree-Fock approach and subsequently the Density Functional Theory have been adopted to reduce the problem to a single-particle one and to accede to the ground state properties.

The drawback to treat systems with reduced symmetry has been often tackled introducing a fictitious periodicity, using a supercell approach in which a slab of finite width, containing the interface, is considered and periodic boundary conditions are applied. Although this formalism gives an efficient estimation of some properties, for example the total energy, the adsorption configurations and the atomic arrangement, it is lacking of accuracy in the description of the surface

states. Indeed due to the finite size of the system the electronic features are discrete states along the surface normal direction. As a consequence no qualitative difference between bulk states and interface/surface ones can be evidenced, and they are only arbitrarily distinguished on the basis of the spatial localization of the wave function. Moreover the degree of hybridization between surface localized states and the bulk ones can not be correctly estimated.

The characterization of the spectral properties can be considerably improved by considering the semi-infinite character of the system. Different methods have been proposed to reach this goal.

We make use of the embedding method of Inglesfield that restricts the calculation to a limited region of space and introduces the effect of the semi-infinite solid through a non local energy dependent term in the Hamiltonian. This approach, which was developed within Density Functional Theory (DFT) framework, revealed really suitable for studying metal surfaces.

The aim of this thesis is to study how the spectral properties of a metal surface are modified by the interaction with different chemical species.

Two limiting cases will be analyzed: the simplest example of interaction represented by a single atom on a surface and the steady phase proper of the completion of the first monolayer.

A brief outline of the embedding method and a simple example of application will be given in Chapters 1 and 2, respectively.

The single atom adsorption will be the object of the first section of the thesis. The details of the implementation will be presented in Chapter 3 while the results will be discussed in Chapter 4.

The second part of this thesis will be devoted to ultra-thin films. The implementation of the embedding for realistic surfaces will be given in Chapter 5 while the results for three different ultra-thin films on metal surfaces will be shown in Chapters 6, 7, 8.

The analysis of the spectral properties of the studied systems will be performed both from a fundamental point of view by characterizing the physical nature of the electronic states, and also with an applicative aim, as a support of experimental findings. Unless stated otherwise, atomic units will be used ($e = m_e = \hbar = 1$) in this thesis.

# List of subjects developed during the thesis

Here we report a detailed list of the subjects developed during the PhD thesis and relative publications.

1. Calculation of electronic and magnetic properties of Fe/Cu(100).
   *"Ab initio electronic and magnetic properties of 1 ML Fe/Cu(001)"*,
   S. Achilli, S. Caravati and M. I. Trioni, *J. Phys. Condens. Matter*, **19**, 305021 (2007).
   *"Ultrathin Fe film on Cu(100): Exchange splitting of image states from first principles"*,
   S. Achilli, S. Caravati and M. I. Trioni, *Surf. Sci.*, **601**, 4048 (2007).

2. Electronic properties of O/Fe(100) and theoretical study of spin-polarized Scanning Tunneling Microscopy and Spectroscopy,
   *"Scanning tunneling spectroscopy of the Fe(001)-$p(1 \times 1)O$ surface"*,
   F. Donati, P. Sessi, S. Achilli, A. Li Bassi, M. Passoni, C. S. Casari, C. S. Bottani, A. Brambilla, A. Picone, M. Finazzi, L. Duó, M. I. Trioni and F. Ciccacci, *Phys. Rev. B*, **79**, 195430 (2009).
   *"Atomic corrugation in Scanning Tunneling Microscopy images of the Fe(001)-$p(1 \times 1)O$ surface"*,
   A. Picone, G. Fratesi, A. Brambilla, P. Sessi, F. Donati, S. Achilli, L. Maini, M. I. Trioni, C. S. Casari, M. Passoni, A. Li Bassi, M. Finazzi, L. Duó and F. Ciccacci, *Phys. Rev. B*, **81**, 115450 (2009).

3. Ab initio investigation of Helium scattering from surfaces,
   *"Dynamics of electron distributions probed by helium scattering"*,
   M. I. Trioni, G. Fratesi, S. Achilli and G. P. Brivio, *J. Phys. Condens. Matter*, **21**, 264003 (2009).

4. Electronic properties of a K overlayer on Cu(111),
   *"Electronic structure and lifetime broadening of a quantum-well state on $p(2 \times 2)$-K/Cu(111)"*,
   S. Achilli, G. Butti, M. I. Trioni and E. V. Chulkov, *Phys. Rev. B*, **80**, 195419 (2009).

*"Detailed features of the surface electronic states of K/Cu(111) by density functional theory"*,
S. Achilli, M. I. Trioni and G. P. Brivio, *Phys. Rev. B*, **81**, 165444 (2010).

5. Spectral properties of single Cs and Ba adatoms on Cu(111) surface,
   *"Spectral properties of Cs and Ba on Cu(111) at very low coverage: Two-photon photoemission spectroscopy and electronic structure theory"*,
   S. Achilli, M. I. Trioni, E. V. Chulkov, P. M. Echenique, V. Sametoglu, N. Pontius, A. Winkelmann, A. Kubo, J. Zhao and H. Petek, *Phys. Rev. B*, **80**, 245419 (2009).

6. Electronic properties of Bi/Cu(100),
   *"Bi ordered phases on Cu(100): periodic arrays of dislocations influence the electronic properties"*,
   P. Gargiani, M. G. Izzo, F. Bussolotti, M. G. Betti, S. Achilli and M. I. Trioni, *J. Chem. Phys.*, **132**, 174706 (2010).

7. Ab initio spectral properties of alkali adatoms on Cu(111), in preparation.

8. Image states of Cu(111) via the phase shift model and the embedding method, in preparation.

# Chapter 1

# The embedding method: general theory

The embedding method, that was developed by J. E. Inglesfield in 1981 (76), can be applied to the study of extended systems whose symmetry is reduced by the presence of a localized perturbation. There are many examples of such situation: impurities in bulk systems (75), atoms or molecules adsorbed on a surface, clean surfaces, multi-layers and interfaces in general. Since the publication of the above-mentioned paper of Inglesfield, the embedding method has found applications in non-relativistic solid-state physics (13; 36; 37; 51; 52; 82; 83; 86; 161; 162), in molecular theory (38; 39; 79), and to study electronic transport in nanowires (84). Moreover, the ideas forming the background of the method were applied by Inglesfield in electromagnetism (77), resulting in the application of the technique in the field of photonics (91). Finally, Crampin (35) has presented an extension of the embedding method to bound and continuum states of Dirac particles.

The method exploits the fact that in systems characterized by an efficient electronic screening, such as for example in metals, a whatever perturbation induced on the charge density has a limited extension in space. The Schrödinger equation can be solved then within such a region only, reducing the computational effort. Nevertheless in order to account for the unperturbed system beyond the embedded region and its effect on the solution, appropriate boundary conditions are imposed through an auxiliary term in the Hamiltonian, namely the embedding potential.

The embedding approach was developed within Density Functional Theory (DFT) (72; 94) for which the charge density is the key quantity and that allows to accede to the ground state electronic properties. In this thesis we maintain this single particle approach.

In order to solve the Kohn-Sham equation the Green's function formalism is adopted that results suitable for calculating the physical quantity of interest and for handling boundary conditions. In this chapter an outline of the method will be presented and the embedding equation will be derived. For more details on the embedding method formalism and its applications see Ref. (78).

## 1.1 The general formulation

In its general formulation the embedding method was developed for a wave-function defined as follows:

$$\Psi(\mathbf{r}) = \begin{cases} \phi(\mathbf{r}) & \mathbf{r} \in \mathrm{I} \\ \psi(\mathbf{r}) & \mathbf{r} \in \mathrm{II} \end{cases} \tag{1.1}$$

where $\phi(\mathbf{r})$ is a trial solution in the perturbed region I while $\psi(\mathbf{r})$ is the solution of the Schrödinger equation in the unperturbed system II at energy $\epsilon$:

$$[-\frac{1}{2}\nabla^2 + V(\mathbf{r})]\psi(\mathbf{r}) = \epsilon\psi(\mathbf{r}) \qquad \mathbf{r} \in \mathrm{II}. \tag{1.2}$$

The wave-functions $\psi(\mathbf{r})$ and $\phi(\mathbf{r})$ match on the surface $S$.

The derivation of the method is based on the variational principle which is used to minimize the total energy of the system. This one can be written as:

$$E[\phi,\psi] = \frac{\int_{\mathrm{I}} d\mathbf{r}\phi^* H\phi + \epsilon\int_{\mathrm{II}} d\mathbf{r}\psi^*\psi + \frac{1}{2}\int_S d\mathbf{r}_s(\phi^*\frac{\partial\phi}{\partial n_s} - \psi^*\frac{\partial\psi}{\partial n_s})}{\int_{\mathrm{I}} d\mathbf{r}\phi^*\phi + \int_{\mathrm{II}} d\mathbf{r}\psi^*\psi}. \tag{1.3}$$

where $n_s$ is the surface normal pointing out the region I.

The aim is to solve the problem in the perturbed region only. For this purpose all the terms containing the unperturbed solution $\psi(\mathbf{r})$ in Eq. (1.3) can be expressed as a function of $\phi(\mathbf{r})$ and of the unperturbed Green's function $G_0(\mathbf{r},\mathbf{r}';E)$ evaluated on the surface $S$.

The single particle Green's function is the solution of:

$$\big[-\frac{1}{2}\nabla^2 + V(\mathbf{r}) - E\big]G(\mathbf{r},\mathbf{r}';E) = \delta(\mathbf{r}-\mathbf{r}') \tag{1.4}$$

where $E$ is in general a complex energy, while $V(\mathbf{r})$ can be the Kohn-Sham effective potential $V_{eff}(\mathbf{r})$ in the Density Functional framework. The Green's function is related to the Kohn-Sham eigenstates $\psi_i(\mathbf{r})$ by its spectral relationship:

$$G(\mathbf{r},\mathbf{r}';E) = \sum_i \frac{\psi_i(\mathbf{r})\psi_i^*(\mathbf{r}')}{\epsilon_i - E}, \tag{1.5}$$

where $\epsilon_i$ are the Kohn-Sham eigenvalues.

In the following formulation of the embedding method the retarded Green's function is considered.

Coming back to the expression of the total energy, we can express $\frac{\partial\psi}{\partial n_s}$ in term of the surface inverse of the Green's function. Exploiting the arbitrarity of the boundary conditions we construct $G_0(\mathbf{r},\mathbf{r}';E)$ to have zero normal derivative on the embedding surface $S$:

$$\frac{\partial G_0(\mathbf{r},\mathbf{r}_s,\epsilon)}{\partial n_s} = 0. \tag{1.6}$$

This condition leads to the fundamental relationship:

$$\psi(\mathbf{r}) = -\frac{1}{2}\int_S d\mathbf{r}'_S G_0(\mathbf{r},\mathbf{r}'_S,E)\frac{\partial\psi(\mathbf{r}'_S)}{\partial n'_S}. \tag{1.7}$$

This important result of the theory shows that if we know the normal derivative of the wave-function on a closed surface and we know the Green's function $G_0$ within that region, we can find the wave-function everywhere. Finally introducing the definition of the surface inverse of the Green's function $G_0^{-1}$:

$$\int_S d\mathbf{r}_S G_0^{-1}(\mathbf{r}''_S,\mathbf{r}_S,E)G_0^{-1}(\mathbf{r}_S,\mathbf{r}'_S,E) = \delta(\mathbf{r}''_S-\mathbf{r}'_S), \tag{1.8}$$

we can invert Eq. (1.7), with $\mathbf{r}\in S$ :

$$\frac{\partial\psi(\mathbf{r}_S)}{\partial n_S} = -2\int_S d\mathbf{r}'_S G_0^{-1}(\mathbf{r}_S,\mathbf{r}'_S,E)\psi(\mathbf{r}'_S). \tag{1.9}$$

The remaining volume integral containing $\psi(\mathbf{r})$ in Eq. (1.3) can be eliminated differentiating the Eq. (1.2) with respect to $\epsilon$. Through a series of formal manipulation one obtains:

$$E[\phi,\epsilon] = \frac{\int_{\mathrm{I}} d\mathbf{r}\phi^* H\phi + \int_S d\mathbf{r}_s \phi^* \frac{\partial\phi}{\partial n_s} + \int_S d\mathbf{r}_s \int_S d\mathbf{r}'_s \phi^*(G_0^{-1} - \epsilon\frac{\partial G_0^{-1}}{\partial\epsilon})\phi}{\int_{\mathrm{I}} d\mathbf{r}\phi^*\phi - \int_S d\mathbf{r}_s \int_S d\mathbf{r}'_s \phi^*(\frac{\partial G_0^{-1}}{\partial\epsilon})\phi}, \qquad (1.10)$$

in which no more terms containing the unperturbed wave-function are present.

By minimizing $E[\phi,\epsilon]$ with respect to variations in $\phi$ and $\epsilon$ it is possible to obtain the solutions of the problem in region I which match both in amplitude and derivative onto the solution on II. If we vary Eq. (1.10) with respect to the trial function $\phi$, we obtain the following equation:

$$\begin{aligned}\Big[ -\frac{1}{2}\nabla^2 \;&+\; \frac{1}{2}\delta(\mathbf{r}-\mathbf{r}_s)\frac{\partial}{\partial n_s} + v_{eff}(\mathbf{r})\Big]\phi(\mathbf{r}) \\ &+\; \delta(\mathbf{r}-\mathbf{r}_s)\int_S d\mathbf{r}'_s \Big[G_0^{-1}(\mathbf{r}_s,\mathbf{r}'_s,\epsilon) + (E-\epsilon)\frac{\partial G_0^{-1}(\mathbf{r}_s,\mathbf{r}'_s,\epsilon)}{\partial\epsilon}\Big]\phi(\mathbf{r}'_s) \\ &=\; E\phi(\mathbf{r}) \qquad \mathbf{r}\in \mathrm{I}. \end{aligned} \qquad (1.11)$$

Varying $E[\phi,\epsilon]$ with respect to $\epsilon$ we have the following additional condition:

$$(E-\epsilon)\int_S d\mathbf{r}_s \int_S d\mathbf{r}'_s \phi^*(\mathbf{r}_s)\frac{\partial^2 G_0^{-1}(\mathbf{r}_s,\mathbf{r}'_s,\epsilon)}{\partial\epsilon^2}\phi^*(\mathbf{r}'_s) = 0. \qquad (1.12)$$

The Eq. (1.12) is fulfilled if:

$$\epsilon = E \qquad (1.13)$$

or otherwise

$$\frac{\partial^2 G_0^{-1}(\mathbf{r}_s,\mathbf{r}'_s,\epsilon)}{\partial\epsilon^2} = 0. \qquad (1.14)$$

It is possible to demonstrate that only the former gives both $\phi$ and $\psi$ that solve the Schrödinger equation in the region where they are defined, and that correctly join on the separation surface $S$. Inserting Eq. (1.13) in Eq. (1.11) one obtain the *embedding equation*:

$$\begin{aligned}\Big[ -\frac{1}{2}\nabla^2 \;&+\; \frac{1}{2}\delta(\mathbf{r}-\mathbf{r}_s)\frac{\partial}{\partial n_s} + v_{eff}(\mathbf{r})\Big]\phi(\mathbf{r}) \\ &+\; \delta(\mathbf{r}-\mathbf{r}_s)\int_S d\mathbf{r}'_s G_0^{-1}(\mathbf{r}_s,\mathbf{r}'_s,E)\phi(\mathbf{r}'_s) = E\phi(\mathbf{r}) \end{aligned} \qquad (1.15)$$

that gives the perturbed solution $\phi$. The surface inverse of the Green function is the so-called *embedding potential*.

We chose to deal with the Green's functions, due to the immediacy in the calculation of the physical quantity of interest, namely the Local Density of States (LDOS):

$$\sigma(\mathbf{r}, E) = \lim_{\delta \to 0} \frac{1}{\pi} \Im m G(\mathbf{r}, \mathbf{r}, E + i\delta) \tag{1.16}$$

and the charge density:

$$\rho(\mathbf{r}) = \frac{1}{\pi} \Im m \int_{-\infty}^{E_F} dE G(\mathbf{r}, \mathbf{r}, E). \tag{1.17}$$

Note that all the density of states we will show in the following chapters are LDOS integrated in a spatial volume.

The embedding equation can be rewritten as:

$$\begin{aligned} [-\frac{1}{2}\nabla^2 &+ v_{eff}(\mathbf{r}) - E] G(\mathbf{r}, \mathbf{r}', E) \\ &+ \delta(\mathbf{r} - \mathbf{r}_s) \left[ \frac{1}{2} \frac{\partial G(\mathbf{r}_s, \mathbf{r}', E)}{\partial n_s} + \int_S d\mathbf{r}_s'' G_0^{-1}(\mathbf{r}_s, \mathbf{r}_s'', E) G(\mathbf{r}_s'', \mathbf{r}', E) \right] \\ &= \delta(\mathbf{r} - \mathbf{r}') \qquad \mathbf{r}, \mathbf{r}' \in \mathrm{I}. \end{aligned} \tag{1.18}$$

The goal is then to solve this embedding equation in order to find $G$. In practice in our calculation we expand $G$ in a basis set $\{\chi_\mu(\mathbf{r})\}$

$$G(\mathbf{r}, \mathbf{r}', E) = \sum_{\mu\mu'} G_{\mu\mu'}(E) \chi_\mu(\mathbf{r}) \chi_{\mu'}^*(\mathbf{r}'). \tag{1.19}$$

Inserting this expansion in Eq. (1.18) and integrating over the embedding region, we obtain the matrix equation:

$$\sum_{\mu''} \{H_{\mu\mu''} + [G_0^{-1}(E)]_{\mu\mu''} - E O_{\mu\mu''}\} G_{\mu''\mu'}(E) = \delta_{\mu\mu'}, \tag{1.20}$$

where $H_{\mu\mu'}$ is the matrix element of the Hamiltonian plus the surface derivative term; $[G_0^{-1}(E)]_{\mu\mu'}$ is the matrix element of the embedding potential; $O_{\mu\mu'}$ is the overlap matrix element in the embedded region.

Once the Green's function is derived the LDOS of the system and the charge density can be easily computed as shown before.

The calculation of the LDOS and the charge density requires to handle with the energy dependence of $G$ through an appropriate choice of the energy contours. In the computation of LDOS the Green's function is evaluated on a path in the complex plane, with a small imaginary part $\delta$. This small imaginary contribution to $E$ causes the fictitious broadening of the discrete features in the Density of States. For the evaluation of the charge density the analyticity of the Green's function in the complex plane can be exploited. As a consequence any kind of contour can be chosen, as long as its end lies on the real axis. A very convenient choice consists in adopting a semi-circular contour so that a large part of this path lies far away from the real axis and the poles of the Green's function. In this way an accurate integration is possible using a limited number of sampling points. Although the integral in Eq. (1.17) extends from the lowest lying state up to the Fermi level, the semi-circular contour is commonly constructed starting from the lower edge of the valence band and the core states, that are discrete ones, are added with a summation.

# Chapter 2

# The one dimensional Chulkov potential: a simple model for metal surfaces

In this chapter we will apply the embedding method to a simple model potential for metal surfaces, in order to show the capabilities of the method and to familiarize with the physical quantities of interest in the study of the spectral properties.

The simplest model for metal surfaces is represented by the jellium in which a semi-infinite homogeneous background of positive charge replaces the atomic nuclei. Since the pioneering work of Bardeen (87), jellium was widely applied to produce a series of interesting results about ground state surface properties (14; 95; 97; 100), adsorption processes (80; 81; 96; 98; 101; 102; 103) and also to treat the fundamental problems of the electron-electron interaction resulting in the Local Density Approximation (27; 128; 133) in Density Functional Theory. Also the embedding method has been applied to jellium, confirming the results of Lang and Kohn for what concerns charge distribution and potential.

Nevertheless due to the extremely simplified potential used for the surface, the jellium model does not allow a realistic description of the surface electronic properties of the realistic bulk substrate.

The one dimensional potential proposed by E. V. Chulkov (32) improves the quality of the results, as will be presented in the following.

In this chapter, after a brief description of the model and of the details for the solution of the embedding equation, the calculation for a standard noble metal surface will be presented, namely Cu(111). In the discussion of the results we will place emphasis on the advantages in using the embedding approach instead of a supercell one.

## 2.1 One dimensional modulated potential

The description of the surface specific electronic properties can take advantage in the introduction of the modulation of the potential due to the atomic nuclei. The simplest solution is to include at first such a modulation perpendicular to the surface and to maintain a constant potential in the direction parallel to the surface. In this way one has to deal with a one-dimensional problem.

Recently a very suitable one dimensional potential has been proposed by E. V. Chulkov and co-workers (32). This potential is built in order to reproduce the surface specific properties. Due to its simplicity and efficiency the model has found large application in surface science physics. For a review see Ref. (44).

The 1D-Chulkov potential describes the surface through an effective pseudopotential which includes a cosine shape in the bulk and surface region, an exponential function out of the surface and an image tail in the vacuum:

$$V(z) = \begin{cases} A_{10} + A_1 \cos \frac{2\pi}{a_s} z, & z < 0 \\ -A_{20} + A_2 \cos \beta z, & 0 < z < z_1 \\ A_3 \exp[-\alpha(z - z_1)], & z_1 < z < z_{im} \\ \frac{\exp[-\lambda(z - z_{im})] - 1}{4(z - z_{im})}, & z > z_{im} \end{cases} \tag{2.1}$$

The potential has ten parameters whose meaning is clear from the Fig. 2.1. Four of them are independent, the other ones can be deduced requiring the continuity of the potential both in amplitude and derivative in the whole space. The potential reproduces the experimental band gap, work function and the surface states binding energies, through an appropriate choice of the adjustable parameters.

Among the approaches used to describe surfaces with the Chulkov model the supercell technique has been the most adopted one in last years. Within this

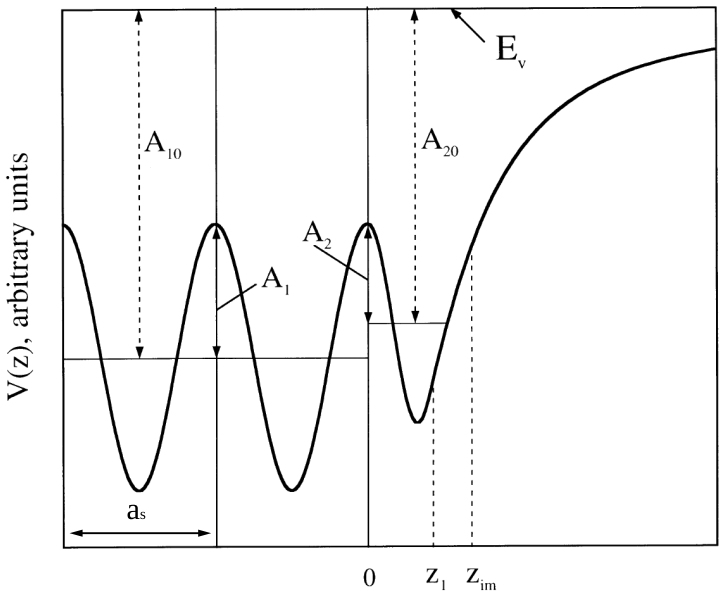


Figure 2.1: The Chulkov 1D model potential.

framework the quality of the results depends on the extension of the slab in the direction perpendicular to the surface and converges increasing the number of layer included in the calculation region. Good results for what concerns the resolution of surface resonances can be obtained including some tens of atomic layers and vacuum within the slab (29).

Differently, within the embedding approach the calculation can be performed in a small cell whose extension ($L$) includes few atomic layers and a vacuum region beyond the surface.

The properties of the semi-infinite bulk and vacuum are included through the embedding potential, defined on the embedding surfaces (points in one-dimensional problems) that limit the embedded region.

Before to analyze the results showing the main differences due to the two different approaches, let us focus on some technical aspects of the calculation.

In order to find the solution for this system, one has to solve the Eq. (1.20). All the matrix elements in Eq. (1.20) are obtained through an expansion on an appropriate basis set. The system geometry and the expression of the potential

suggest to adopt a basis set such as:

$$\chi_n(z) = \begin{cases} \cos(k_n z) & n \text{ even} \\ \sin(k_n z) & n \text{ odd} \end{cases} \tag{2.2}$$

where $k_n = n\pi/\tilde{L}$. Note that the basis set is defined on a region $\tilde{L}$ which is slightly larger than $L$, in order to avoid any constraint to the solution on the boundaries of the embedded region.

For what concerns the embedding potential, the following relationship can be derived from the Eq. (1.9):

$$G_0^{-1}(z_s, z_s, E) = 2\frac{\partial \log \psi_E(z)}{\partial z}\bigg|_{z_s} \tag{2.3}$$

that relates the embedding potential to the logarithmic derivative of the solution $\psi(z_s)$ of the Schrödinger equation on $S$ at a particular energy $E$.

On the bulk side, thanks to the periodicity of the potential ($V(z) = V(z+a_s)$, where $a_s$ is the lattice parameter), the Floquet analysis (1) can be applied and the transfer matrix technique is used to evaluate $\psi(z_s)$. For the formal details of this procedure see the Appendix A.

The calculation is performed by defining at first a discrete set of energy points in which the embedding potential is computed. From the bulk side the embedding surface is always fixed in correspondence of a maximum of the potential. The Schrödinger equation in the bulk is then solved with a standard numerical method and the coefficients of the transfer matrix are obtained. Consequently the eigenvalues and the eigenvectors of the Floquet-Bloch equation are determined.

Due to the periodicity of the bulk potential the two solutions $\psi_{1,2}(x)$ that can be derived satisfy:

$$\psi_{1,2}(z) = u_k(z)e^{\pm ikz} \qquad \text{with} : k = \sqrt{2(E - V_b)}. \tag{2.4}$$

However only plane waves traveling *inwards* the embedded region should be considered and therefore only the $\psi_2$ can be retained. There are two different subsets of solutions: for $E < V_b$ there will be complex values of $k$ with $\Im mk \neq 0$, leading to solutions non-integrable in bulk; for $E > V_b$, $k$ will assume real values through the dispersion relationship $E = \frac{k^2}{2} + V_b$.

Finally using the $\psi_2(z)$ in Eq. (2.3) the embedding potential is determined as:

$$G_0^{-1}(z_s, z_s, E) = ik + \left.\frac{d\log(u_k(z,E))}{dz}\right|_{z_s}. \tag{2.5}$$

On the vacuum side the embedding surface cuts the image potential tail. In order to determine the solution for the image potential in vacuum the Numerov algorithm is applied. The embedding potential is thus evaluated through the logarithmic derivative of the wave-function.

Recently a different approach for the application of the embedding method to the 1D Chulkov potential has been proposed by J. E. Inglesfield (2).

Once that the embedding potential is known, the matrix equation (1.20) can be solved, being the overlap matrix and the Hamiltonian matrix elements of easier calculation. The Green's function of the system is then used to compute the physical quantities of interest.

In the next section the results obtained for Cu(111) will be presented. The independent parameters of the Chulkov potential used to obtain these results are those reported in Ref. (32) for the clean Cu(111) surface ($A_{10} = -11.895$ eV, $A_1 = 5.14$ eV, $A_2 = 4.3279$ eV, $\beta = 2.9416$).

The width of the embedded region chosen for the calculation is 20 Å. It includes five atomic layers (interlayer spacing $a_S = 2.08$ Å) and about 5 Å of vacuum. Anyway it is worthwhile to stress here that in this particular application of the embedding method the width of the embedded region is not relevant in determining the solution for the problem.

The suggested requirement for the embedded region is that it should be large enough to allow a complete screening of the perturbation. Differently, in this case the effective potential is given *a priori* so that it already contains the screening effects. The solution is thus univocally determined. We will return on this important point in Section 2.2.

### 2.1.1 Results

The implementation of the embedding method for this one dimensional modulated potential is currently not self consistent. This means that once that the

analytic potential is given and the matrix embedding equation is solved, the Green's function is used to calculate the Density of States (DOS) and the charge density that are the final output of the calculation. Let us start from the one dimensional DOS per unit cell, i.e. the DOS at $k_{\parallel} = 0$ which is obtained from the imaginary part of the trace of $G(z, z', E)$:

$$\sigma_{1\mathrm{D}}(E) = \frac{1}{\pi} \int_0^{L_z} \Im m G(z, z, E)\, dz. \tag{2.6}$$

In the previous equation the Fourier component $G(z, z, E)$ has been used. In fact, due to the invariance along $x$ and $y$, the Green's function can be re-written as:

$$G(\mathbf{r}, \mathbf{r}', E) = \iint \frac{d_2 k_{\parallel}}{(2\pi)^2} e^{i\mathbf{k}_{\parallel}\cdot(\mathbf{R}-\mathbf{R}')} G_{\mathbf{k}_{\parallel}}(z, z', E), \tag{2.7}$$

being $\mathbf{R} = (x, y)$ and $\mathbf{k}_{\parallel} = (k_x, k_y)$. The dependence of $G_{\mathbf{k}_{\parallel}}(z, z', E)$ from the parallel momentum $\mathbf{k}_{\parallel}$ results extremely simple:

$$G_{\mathbf{k}_{\parallel}}(z, z', E) = G(z, z', E - k_{\parallel}^2/2). \tag{2.8}$$

In Fig. 2.2 the 1D-DOS of Cu(111) is reported. Such a DOS has been evaluated in the embedded region and it has been computed including a small imaginary part of Energy, equal to $2.7 \times 10^{-5}$ eV, in the calculation.

The 1D-DOS shows the projection of the bulk density of states on the (111) direction at $\overline{\Gamma}$. Two continuous bulk bands can be observed, one that extends from $-7.8$ eV to $-0.89$ eV, and the other at energies greater than 4.25 eV.

Between $-0.89$ eV and 4.25 eV an energy gap is visible, where no bulk solutions can be found. This gap is not absolute, but varies with $\mathbf{k}_{\parallel}$. Within the gap some discrete features are found that are two typical example of surface states: the Shockley state at $-0.39$ eV and the $n = 1$ image state at 4.12 eV.

The Shockley state results from the truncation of the crystal potential at the surface and it is typical of situations in which the electron orbitals on the atoms interact strongly.

The image potential induced states describe instead electrons that are bound to their own image in the solid (45).

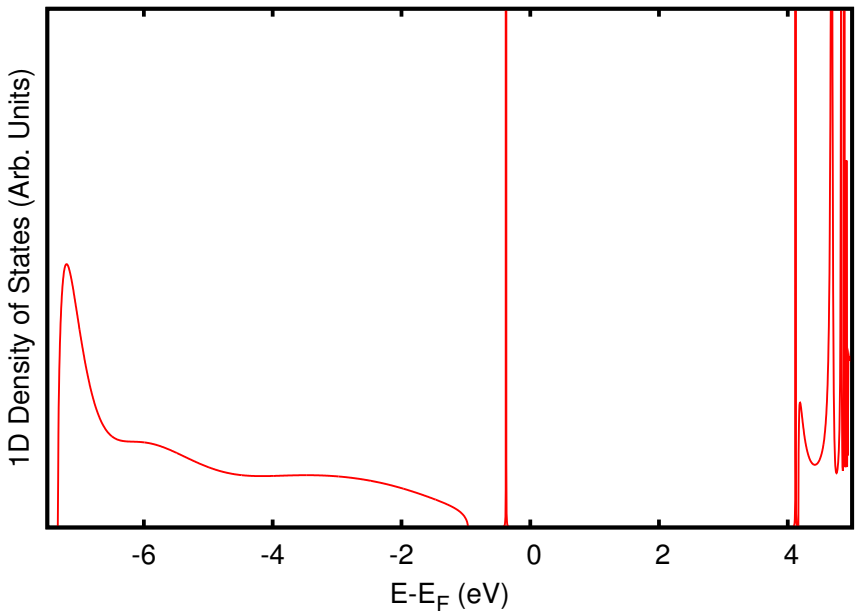


Figure 2.2: 1D-DOS of Cu(111) obtained by applying the embedding method to the Chulkov potential.

A fundamental difference between these two classes of surface states is their spatial localization. While the Shockley state is mainly located in the topmost atomic layer on the surface, the wave-function probability amplitude of the image states has a maximum in the vacuum far away from the surface.

Both the Shockley state and the image series, like other surface features that will be presented in the following, can act as intermediate states for the relaxation of electronic excitations at surfaces. The efficiency of such a process strongly depends on the lifetime of these states.

The general theory for lifetime accounts for three contributions: one due to electron-electron interaction, the second that includes electron-phonon interaction and the last one that is relative to the electron-impurity scattering. The electron-electron decay channel can occur via one electron scattering with bulk states (elastic scattering) and many body inelastic scattering.

The challenging peculiarity of the embedding method is that it permits to estimate the elastic term, thanks to the capability of describing the interaction between the continuum of bulk states and the surface specific features. Exploiting

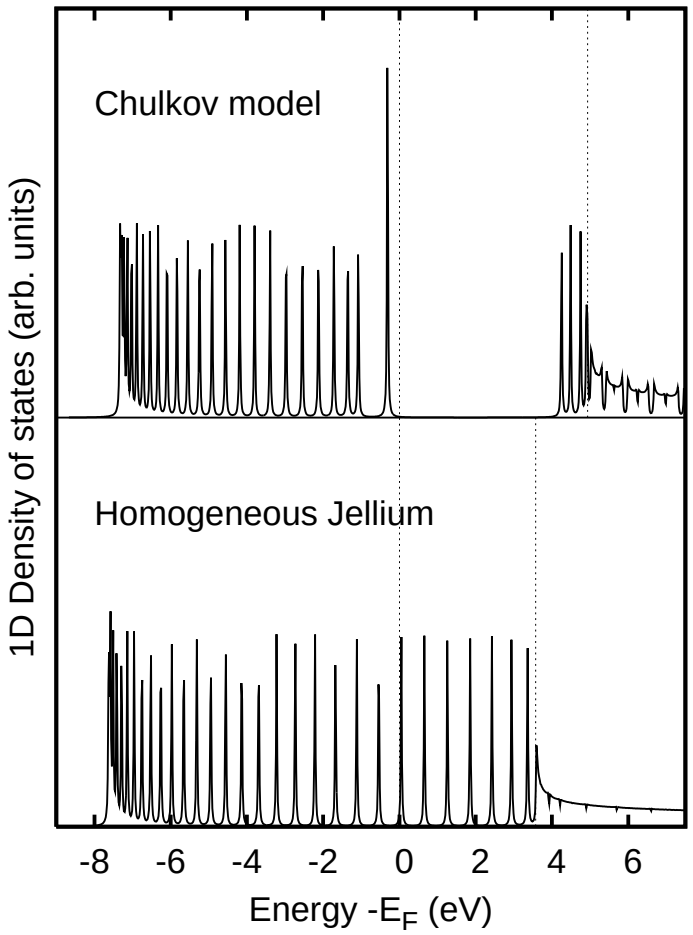


Figure 2.3: 1D-DOS obtained by the Chulkov potential of Cu(111) (upper panel) and by the jellium model with $r_S = 2.67$ a.u. (lower panel) using a supercell approach. The two images are aligned with respect to the Fermi level which has been chosen as reference. The dotted lines at higher energies are the vacuum level for each model.

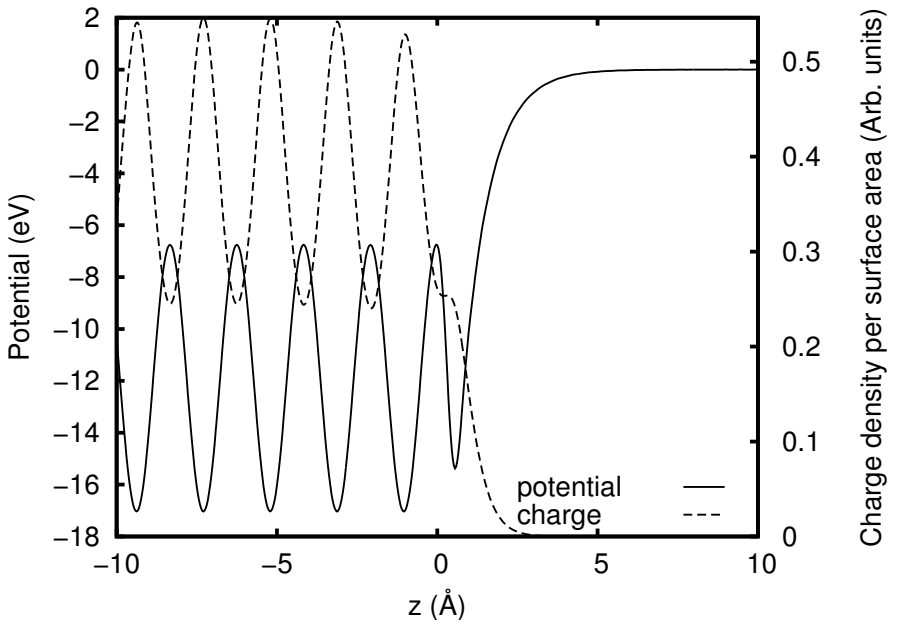


Figure 2.4: Effective Chulkov potential and relative charge density.

the relationship between the lifetime $\tau$ and the linewidth $\Gamma$: $\tau = \hbar/\Gamma$ one can derive the elastic contribution to lifetime of a particular surface state from its linewidth in the DOS.

The Shockley state and the first image state of Cu(111) are discrete states because they lie within the energy gap so there is no elastic contribution to their lifetime. Differently the $n \geq 2$ image states have a resonant character due to the hybridization with the bulk band and they display a finite linewidth.

This 1D-DOS looks very different from that obtained with a supercell approach, reported in Fig. 2.3 in the upper panel. From this picture it is evident that, despite of the large calculation region (25 layers) no spectral difference between the bulk states and the surface specific Shockley and image states can be accounted for.

From the comparison with the 1D-DOS of the jellium, which is reported in the lower panel of Fig. 2.3 as results of the calculation in a slab of the same thickness, emerges the benefit in the choice of the Chulkov potential to describe the surface. The jellium model indeed does not allow to obtain the energy gap and the discrete surface state therein and also the vacuum level is wrong.

Another physical quantity that can be derived from the Green function is the total charge density that is obtained as follows:

$$\rho(z) = \int_{-\infty}^{E_F} \sigma_{1D}(z, E)\, dE \tag{2.9}$$

In Fig. 2.4 the charge density is reported, superimposed to the effective Chulkov potential. A comparison with the position of the maxima in the potential shows that the charge density accumulates between two consecutive layers while outside the surface it exponentially decays in vacuum.

## 2.2 The Chulkov potential as a Kohn-Sham effective potential

The calculation we have presented in the previous section consists in determining the Green's function for a given potential through the embedding method. In order to exploit the same pseudopotential for more advanced calculations, such as for example the 3D calculation for a single atom on a surface, presented in next chapters, some important assumptions have to be done.

Let us remember that our formalism exploits a Density Functional Theory approach in which the Kohn-Sham Hamiltonian is solved. This requires the definition of a Kohn-Sham effective potential:

$$V_{eff} = V_H + V_{XC} + V_{ext} \tag{2.10}$$

The term $V_H$ is the Hartree potential while $V_{XC}$ is the exchange-correlation contribution. Once that the total charge density is computed, as explained in the previous section, these two term can be computed. The latter is obtained in Local Density Approximation (LDA) while the former is calculated in reciprocal space solving the Poisson equation with the charge density obtained as reported above.

The Hartree and the exchange and correlation potentials are reported in Fig. 2.5. The last term, $V_{ext}$, is the external potential which is due to the ionic contribution. Commonly in DFT first principle calculations the $V_{ext}$ is given as input data and both the effective potential and the Coulomb term are evaluated

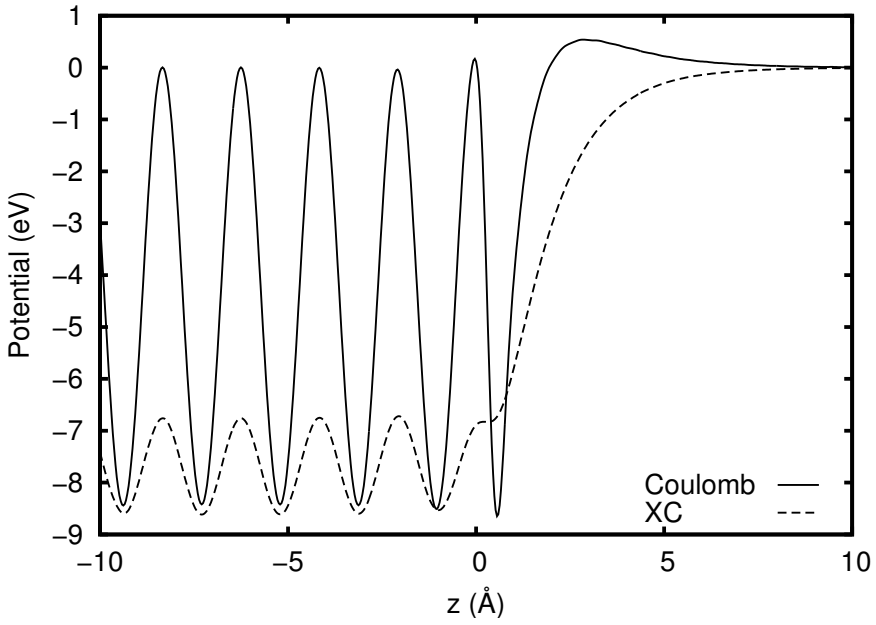


Figure 2.5: Exchange-Correlation and Hartree contribution to the effective Chulkov potential.

at each step of the self consistency. In our calculation, contrary to the usual, the effective potential is known.

Exploiting the one-to-one correspondence between the ground state charge density and the external potential demonstrated by the Hoenberg-Kohn theorems, one could be interested in evaluating the potential that gives the ground state charge density reported in Fig. 2.4.

The external potential has been computed as:

$$V_{ext} = V_{eff} - V_H - V_{XC}. \tag{2.11}$$

This term serves as input data in the *ab initio* calculation presented in the following chapters, for the construction of the external potential in the adatom on surface case.

## 2.3 Effects of the image potential tail

The Chulkov potential, reported in Eq. (2.1) is built in order to account for an image potential tail in the vacuum. This one can be related to the electrostatic attractive potential felt by an electron in front of a metal surface, due to its image charge inside the metal:

$$V(z) = -\frac{1}{4(z - z_{im})} \tag{2.12}$$

where $z_{im}$ is the image plane. Such a potential can not be reproduced in DFT dealing with a local approximation for the exchange and correlation. The failure of DFT in giving the correct asymptotic form of the surface barrier can be related to the exponential decay of the electron density outside the surface. Indeed the surface barrier is determined by an electrostatic contribution which has a short range character and by the exchange and correlation potential that gives the long range asymptotic behaviour. Considering for the exchange and correlation potential a local function of the charge density the decay of the long range term of the potential results to be exponential. As a consequence the image states can not be reproduced in self consistent DFT calculations and some strategy has to be built up in order to overcome this drawback. We will return on such a problem in Chapter 5.

In the case discussed in this chapter the effective potential is not determined self consistently but it is furnished *a priori* and built up in order to correctly reproduce the asymptotic behaviour. Nevertheless it can be useful to replace the correct asymptotic potential with an exponential function, in order to evidence what are the main effects on the electronic properties related to the inclusion of the image tail in the potential. The plots in Fig. 2.6 evidence the variation of the computed electronic properties due to the presence of the image tail. The inset in the right panel of Fig. 2.6 reports the surface barrier in the two cases, showing the slower decay of the potential which accounts for the image tail. In the left panel the 1D-DOS obtained neglecting the image potential tail is displayed. In this plot the vertical dashed lines correspond to the surface states of the Cu(111) surface. In addition to a wrong description of the DOS in the energy region close to the vacuum level (no image states are detected) also the Shockley state is shifted with respect to the experimental energy position. In particular, because the surface

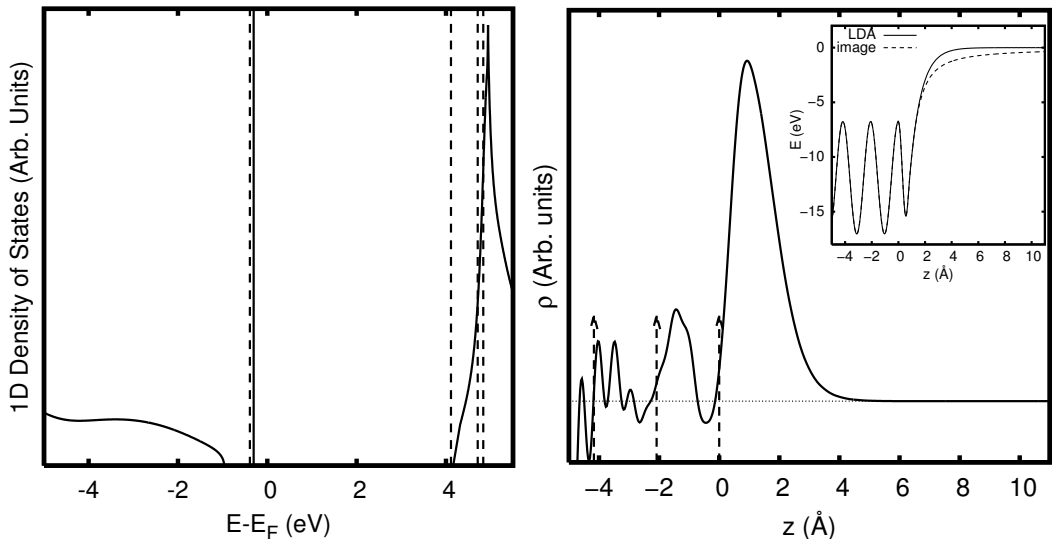


Figure 2.6: Left panel: 1D-DOS obtained using a LDA potential. Right panel: difference between the charge densities obtained in the two calculations. The inset shows the Chulkov effective potential with and without the image tail

barrier is higher in the LDA case, the Shockley state is higher in energy. The panel on the right reports the difference between the charge densities obtained in the two calculations. Although the absolute value of this quantity is really small, the main differences are found just outside the surface, i.e. in the spatial region where the Shockley surface state is localized.

# 2. THE ONE DIMENSIONAL CHULKOV POTENTIAL: A SIMPLE MODEL FOR METAL SURFACES

# Part I

# Single atom adsorption on metal surfaces

# Chapter 3

# An embedding approach for single atom adsorption

The one dimensional model adopted in the previous chapter allowed to show the capabilities of the embedding method in the description of the spectral properties. In this chapter the model will be extended to the case of a single adatom on a metal surface.

The adsorption of a single atom on a surface realizes in a large variety of contexts and it is at the basis of many physical processes: diffusion, early nucleation, ion-surface collision, dissociation of molecules, chemical reactions at the surface.

Besides in the adsorption process the elementary interaction between the surface and the external atom realizes. Depending on the strength of such interaction one can distinguish between physisorption, characterized by low adsorption energy, and chemisorption in which a chemical bonding between the surface and the adatom takes place. For a review of adsorption see Ref. (120; 140).

In this work we will concentrate on chemisorption, with the purpose to analyze the changes in the spectral properties due to the atom-substrate interaction. As a consequence of such interaction both the surface and adatoms states mix and new electronic levels arise, that are usually broadened and shifted with respect to that of the uncoupled systems. Although in general these states can be related to the original unperturbed ones, both of the atom and the surface, this assignment can turn out to be misleading. Often it is more appropriate to consider the new electronic properties as the result of the chemical bonding established between the

constituent elements. The nature of the chemical bonding between the adatom and the surface has been object of many works in the past (see for example Ref. (15; 61; 102; 118)).

This kind of analysis produces an insight on the *static* facet of adsorption. The term *static* is used here in opposition to the *dynamic* aspect proper of the motion of atoms on the surface. The latter problem is related to the determination of the potential energy surface (PES) whereas the former is relative for example to the study of the electronic structure, i.e. for example the charge density and the energy spectrum of the system.

The spectral properties of adsorbed atoms have been investigated in the past both by simple models, that capture the essential physics, and using more sophisticated approaches for an accurate characterization of the electronic states of the system (23). The Newns-Anderson model (6; 115), that works out the two limiting cases of weak and strong adsorption depending on the bandwidth of the metal substrate, and that evidences the importance of the coupling constant, is an example of simplified approach. In the same class can be included the Gurney model (66) that invoked the formation of an electrical double layer to explain the spectral properties of adsorbed alkali atoms. The Gurney picture together with the very rich literature about the adsorption of alkali atoms on metals, will be treated in the next chapter.

The second approach attempts to perform a large-scale *ab initio* calculation of the electronic structure. To this purpose many theoretical calculations have been performed exploiting the Density Functional formalism. They divide in those that use an extended substrate and those that model the system with a small cluster of atoms or a finite number of atomic layers periodically repeated. In the former case the substrate was commonly described as a jellium (69; 103), a suitable approximation for free electron like metals which is not appropriate for the $d$-bands of transition metals.

Different treatments have been developed in order to deal with the semi-infinite character of the solid. A large part of them exploits the Dyson equation formalism (63; 64). The adsorption of single atoms on jellium was also studied with the embedding approach (154) that reproduced the early results of Lang and Williams (103).

These calculations give an overview of the spectral properties of adsorbed systems such as the shift and the broadening of the electronic levels, the charge transfer, the surface dipole. Nevertheless, as already stated in the previous chapters, the jellium model does not allow to reproduce a realistic surface projected band structure which is related to the periodic modulation of the potential.

Other more elaborate *ab initio* calculations have been performed in the Density Functional Theory framework, heading toward a more realistic picture of the adatom-surface system. The major drawback is the lack of periodicity in every direction, due to the point defect represented by the adatom.

Within the cluster approach (126; 142) a finite number of atoms is used to describe the adsorbate and the underlying substrate. Although the computational resources available nowadays allow to consider a quite large cluster, this model clearly suffers from the consequences of the finite extension of the system, in particular for what concerns the convergence of the adsorption energy varying the number of atoms in the calculation (151), and the pure discrete spectrum which is obtained.

As an alternative, a commonly adopted supercell approach is used. In this case the solid is represented by some atomic layers and, instead of a single adatom, a regular array of adsorbates on the surface is considered. This finite extension of layers is repeated periodically in the direction perpendicular to the surface, leading to a fully three dimensional periodic system, for which the standard bulk techniques can be used.

Despite of the relatively small computational effort required from this approach, that made the supercell technique widely adopted, the quality of the results is damaged by the adsorbate-adsorbate interaction, as well as the impossibility of reproducing the continuum of bulk states.

The embedding method that we adopt in this work provides a partial solution to the problems reported above. The advantages of taking into account the semi-infinite character of the system have been already discussed in the previous chapters.

The embedding treatment of a single atom adsorption on a jellium-like metal surface is nowadays well grounded. The original result of this thesis is the treatment of a single adsorbate on a modulated one dimensional potential.

This model improves considerably the description of the spectral properties of the system, allowing a more realistic picture of the adatom induced resonances and their physical properties, such as for example their spatial extent and lifetime. In the following part of the chapter some basic details about the implementation of the embedding method for single atom adsorption will be given, while in Chapter 4 the results for some representative systems will be presented.

## 3.1 Embedding formalism for adsorption

A single atom adsorbed on a surface introduces a spherical perturbation on the system that consists of the semi-infinite solid in contact with the semi-infinite vacuum.

Due to the symmetry of the atomic potential, a spherical embedded region is convenient.

This embedded sphere is centered on the adatom and it extends as far as the induced perturbation is well screened. The typical radius is of the order of 3-6 Å depending on the chemical nature of the adsorbate and the substrate.

In order to apply the embedding method to single atoms on a modulated potential a self consistent calculation has been adopted. The Green's function of the clean surface $G_0$, obtained as explained in Chapter 2, is retained as the unperturbed solution and it is used to build the embedding potential through the matching Green's function technique (57; 74). For this purpose the unperturbed Green's function is re-expanded on an appropriate basis set. Being interested in the Green function on the spherical surface $S$, a convenient choice is represented by spherical harmonics.

The unperturbed Green function is expanded as:

$$G_0(\mathbf{r}_S, \mathbf{r}'_S) = \sum_{LL'} \Gamma_{LL'} Y_L(\Omega) Y^*_{L'}(\Omega'). \tag{3.1}$$

where $L$ is the composite angular momentum index $L = (l, m)$, and $\Omega$ is the solid angle.

The coefficients $\mathcal{G}^{-1}_{0LL'}$ of the surface expansion of the embedding potential,

$$G_0^{-1}(\mathbf{r}_S, \mathbf{r}'_S) = \sum_{LL'} \mathcal{G}^{-1}_{0LL'} Y_L(\Omega) Y^*_{L'}(\Omega') \tag{3.2}$$

can be derived from the matrix equation:

$$\mathcal{G}_0^{-1} = \Gamma^{-1}[1 + \Gamma' r_S^2/2] \tag{3.3}$$

where $\Gamma'$ are the matrix elements of the surface expansion of the derivative of the Green's function (154).

The self consistent procedure requires the solution of the matrix embedding equation. To this purpose the Kohn-Sham effective potential $V_{eff}$ has to be determined.

It is composed by three terms:

$$V_{eff}(\mathbf{r}) = V_H(\mathbf{r}) + V_{XC}(\mathbf{r}) + V_{ext}(\mathbf{r}), \tag{3.4}$$

where $V_H$ is the Hartree potential due to the electron-electron interaction, $V_{XC}$ is the exchange and correlation term and $V_{ext}$ is the external potential.

While $V_H$ and $V_{XC}$ are determined at each step of the self consistent procedure upon the calculation of the electronic charge density, the external potential is an input data. It is given by:

$$V_{ext} = V^0_{ext} + V_{atom} \tag{3.5}$$

where $V^0_{ext}$ is the potential generated by the tail of positive charge of the surface that extends in the embedding sphere. The term $V^0_{ext}$ is taken from the 1D calculation for the clean surface, as explained in Chapter 2. For the atomic potential $V_{atom} = Z/r$ is used.

The calculation of the effective potential within the embedded sphere requires that the correct matching conditions are verified on the sphere boundary. In particular the Coulomb potential is joined on the embedded sphere to the Coulomb potential of the clean surface.

For what concerns the calculation of the matrix element of the kinetic energy, and the effective potential refer to Ref. (154).

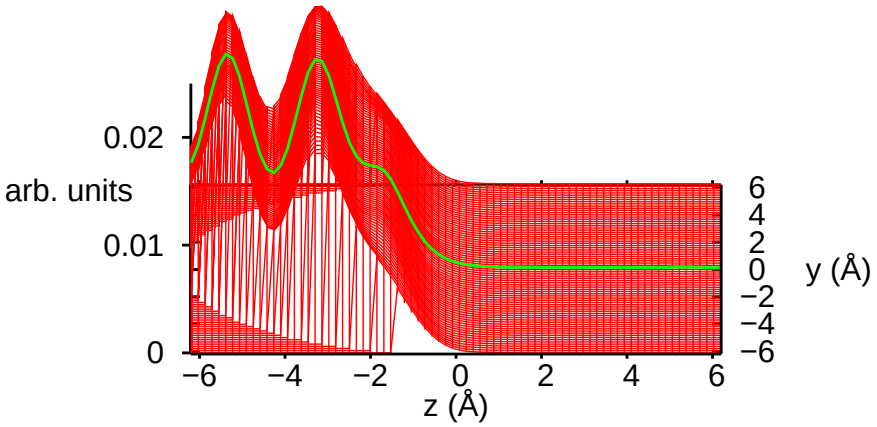


Figure 3.1: Three dimensional charge density for the clean surface of Cu(111)

## 3.2 The clean surface in the embedding sphere: from 1D to 3D

Before showing the results for adatoms on metal surfaces we analyze the case of a 3D calculation for a clean surface described by the 1D Chulkov potential. In practice the embedding formalism just presented is applied to the clean Cu(111) surface. The obtained results, in addition to give familiarity with the integration in the reciprocal space, will be useful in order to evaluate some induced properties, discussed in the following chapter, due to the adsorption of single adatoms on such a surface. In Fig. 3.1 is reported the charge density obtained through the embedding code for adsorption. It is very similar to that depicted in Fig. 2.4 that resembles a lateral sketch of such 3D plot.

The 3D embedding code has been developed in perspective of application to the treatment of adsorption. Consequently, because in presence of the adatom the translational symmetry is not preserved and $\mathbf{k}_{\parallel}$ is no more a good quantum number, the code performs an integration in $\mathbf{k}_{\parallel}$ in the calculation of the DOS. The same procedure is thus performed also in the case of the clean surface (no atoms adsorbed) for which in principle the translational invariance in the parallel direction holds.

The resulting DOS is reported in Fig. 3.2. Due to the integration in the

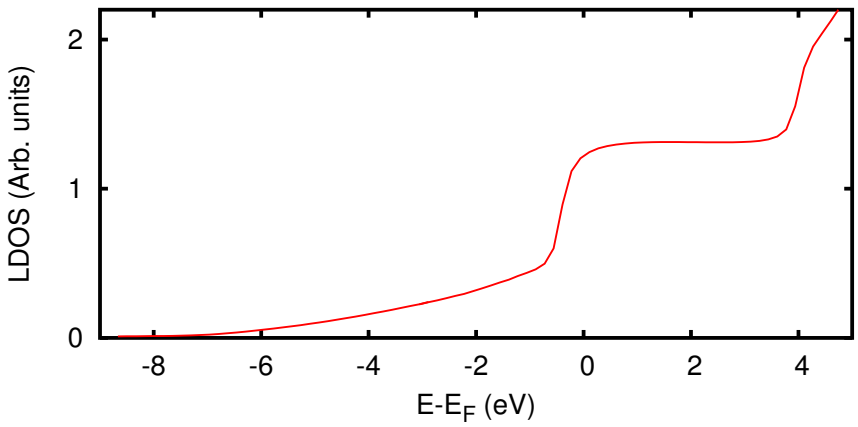


Figure 3.2: Density of states of the clean surface of Cu(111) obtained within a 3D calculation.

surface Brillouin zone (which is equivalent to an integration in energy, $\mathbf{k}_{\parallel}$ being $\propto E$) the DOS grows corresponding to the bulk bands, it is constant within the energy gap and display a step behaviour corresponding to delta-like states. In particular the step at -0.39 eV corresponds to the Shockley state of Cu(111) while that at about 4 eV is relative to the n=1 image state. Note that the unsharp step rise corresponding to delta-states is an effect of the imaginary part of the energy which is included in the calculation to avoid any problem in the evaluation of the embedding potential in the poles of the Green's function. This smoothing of the DOS is thus fictitious and could be avoided by reducing to zero the imaginary part of energy.

# 3. AN EMBEDDING APPROACH FOR SINGLE ATOM ADSORPTION

# Chapter 4

# Single atom adsorption: results

In this chapter some results relative to the adsorption of different atoms on metal surfaces will be shown. In particular in the first section a wide analysis of the spectral properties of alkali atoms on Cu(111). The choice of the substrate allows to point out the importance of the energy gap of the metal for a correct description of the electronic properties of the system. The second section will be devoted to the case of a two valence electron adatom, Ba, adsorbed on Cu(111).

## 4.1 Alkali-metal adsorption

The adsorption of alkali-metals on metal surfaces has been widely studied in past years as the simplest example of single atom adsorption, together with the case of an hydrogen adatom (115).

Since the early studies of low coverage Cs adlayers on W, Ni, Mo (93) it was clear that the main peculiarity of alkali adsorption consists in the lowering of the substrate work function. In the pioneering work of Langmuir (150) it was observed experimentally that, increasing the alkali coverage, the work function takes a minimum before reaching a saturation value. The same behaviour was observed on many metal substrates (67; 73; 127; 130; 153) and also on semiconductors (90; 121). Nevertheless the most appealing results concern the transition-metal substrates due to the wide perspective of their application in catalysis. In particular an intensive experimental and theoretical analysis was performed in past years on alkali metal atoms adsorbed on noble metals. Fig. 4.1 displays the

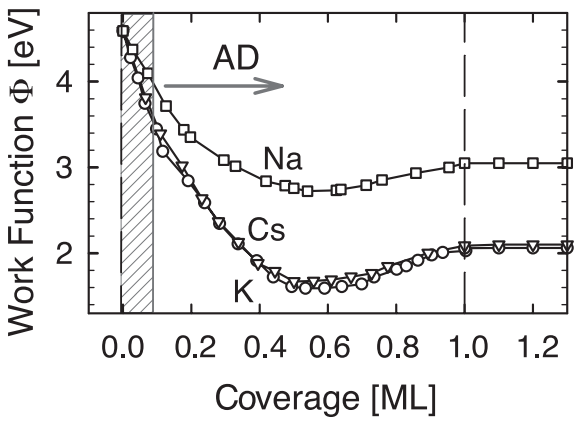


Figure 4.1: Experimental results about the variation of the work function with coverage. The picture is taken from Ref. (53)

variation of the work function of Cu(111) as a function of the coverage of Na, Cs, K adsorbed.

The initial lowering of the work function was explained by Langmuir in a classical picture, as the effect of the induced surface dipole due to the ionization of the alkali adatom upon adsorption. He suggested that the charge transfer from the adatom to the substrate, i.e., the adsorption of the alkali as a positive ion, is due to the lower ionization potential of the adatom than the work function of the metal. Subsequently Gurney (66) confirmed this picture through a quantum-mechanical treatment that accounts for a possible partial ionization of the adatom. He suggested that the degree of atomic ionization depends on the interaction with the substrate states. In particular the extent to which the positive core of the adsorbed atom is neutralized by the valence electrons of the system depends on the binding energy of the valence atomic levels with respect to the substrate Fermi level. Indeed, approaching to the surface, the atomic wavefunctions overlap with the metal states resulting in broad resonances. These resonances can be partially filled if they lie near the Fermi level of the substrate leading to a partial screening of the positive ion. The validity of the Gurney model has been confirmed by a series of theoretical studies (21; 103; 140) and this picture has been widely accepted as a basic concept for alkali adsorption.

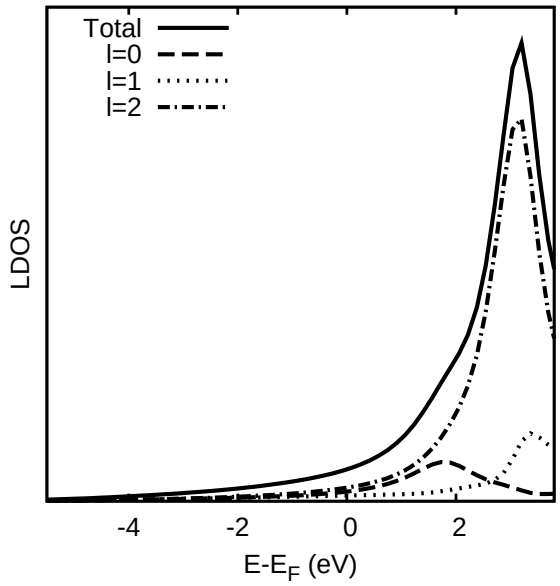


Figure 4.2: LDOS of Cs on jellium ($r_S = 2.67$) obtained through an embedding calculation. The adsorption distance is taken in this case equal to 2 Å from the jellium edge.

Increasing the coverage the adsorbate-adsorbate distance decreases and the electrostatic repulsion between the adatoms grows. In order to lower the total energy, a back donation of electrons from the metal toward the adatoms takes place and it determines the increasing of the work function after the minimum. For coverages near 1ML the work function tends to the value of bulk alkali.

The Gurney picture relative to the shift and broadening of the atomic levels of adsorbed species opened the way to a series of atomistic adsorption theories (15; 56; 62) based on the Anderson-Fano model (6; 48). In the seventies the analysis of the adsorption induced atomic resonances was favoured by the advent of the Density Functional Theory that produced the notable Lang and Williams results for alkali (and other atoms) on jellium surfaces (103). This model gives a very broad resonance in the unoccupied spectrum (see Fig. 4.2 which reports the LDOS of Cs on jellium obtained through an embedding calculation), that was often assigned to the $s$ atomic level, partially hybridized with the slightly higher $p_z$ orbital (80; 88; 119).

Concerning this assignment and in particular to the entity of the $s$-$p_z$ hybridization the works of Muscat and Newns are worthy of citation (110; 111). The authors exploited a matching wave-function technique in order to show how the energy position and the linewidth of the main resonance change as a function of the adsorption distance. They considered the factors that determine the resonance broadening and the causes of the hybridization between the atomic levels, confirming the results of Lang and Williams.

In recent decades the increasing accuracy of spectroscopic techniques allowed an intensive experimental investigation of the unoccupied spectral properties of low coverage adsorbates (7; 12; 49; 135; 149). A recent two photon photoemission experiment (166) has evidenced a general behaviour for all the alkali adatoms that display the atomic resonance always at the same energy position with respect to the Fermi level.

In addition, differently from what is predicted by adatom on jellium calculations, such main resonance has been found to be very long-lived, that means really narrow in energy, of the order of few meV (10; 11; 122). The scientific relevance of this really large lifetime is undoubted: this property makes this resonance an ideal transient state in excited state mediated surface reactions (54; 59).

Recently a new theoretical approach has been adopted in order to reproduce such properties of the system. The method has its foundation on the Langmuir picture that assumes a complete ionization of the alkali-metal adatom. According to this assumption the method considers the interaction between the only active electron and the compound formed by the alkali ion core and the metal surface. The last one is modeled through the Chulkov potential in order to account for the main features of the substrate band structure. The single valence electron is assumed to interact with the system through an image-charge interaction. It experiences the attractive Coulomb potential produced by its own image charge inside the surface and the repulsive interaction which is due to the negative charged image of the alkali-atom ionic core (18; 55). The model Hamiltonian obtained combining such terms has been exploited in different kind of electronic structure calculations such as the coupled angular model (CAM) (152) or the wave packet propagation (WPP) (18; 46). The last one has been applied to explain both the period independent binding energy of the $ns$ atomic resonance (166) and

its extremely long lifetime (19; 59). It consists in a non-stationary approach in which the time dependent Schrödinger equation is solved, in order to follow the evolution of the wave-packet of the single active electron in the potential built as above. The results obtained with WPP allowed to highlight the fundamental role of the substrate in the determination of the resonance lifetime (19; 20).

The embedding method adopted in this thesis furnishes an alternative approach for treating adsorption. Differently from the WPP method, a self consistent Hamiltonian is used and no more assumptions on the interacting potential involving the active electron are necessary. Consequently the charge state of the adatom is not fixed *a priori* but results from the self consistent procedure. In addition the embedding approach allows to treat the electron-electron interaction on the adatom so that also atoms with more than one valence electron can be treated. Thanks to the inclusion of the embedding potential in the Hamiltonian the hybridization of the atomic levels with the substrate states can be accounted for and an estimate of the elastic linewidth of the resonances is possible.

### 4.1.1 Computational details

Due to the charge transfer from the adatom to the surface, the adsorption of single alkali atoms introduces a long range tail in the effective potential. In order to guarantee the correct matching to the unperturbed solution outside the embedded region, it would be useful to choose a quite large sphere as a calculation region. Nevertheless, increasing the size of the sphere, a large number of basis functions is necessary to describe the oscillations of the wave-function, requiring a huge computational effort. A good balance between accuracy of the results and computational cost can be obtained using a sphere of $\sim 6$ Å and an angular expansion up to $l = 18$.

The adatoms are located at the origin of the coordinate system. In Tab. 4.1 their adsorption distances with respect to the surface ion core are reported. They have been obtained by a DFT calculation for a dilute $7 \times 7$ phase (166).

Little discrepancies between these values and that reported in other works (both theoretical and experimental) can produce a small shift of the surface induced features.

| Adatom | Li | Na | K | Rb | Cs |
|---|---|---|---|---|---|
| Distance | 2.22 | 2.55 | 3.00 | 3.11 | 3.33 |

Table 4.1: Equilibrium adsorption distances of alkali adatoms on Cu(111) expressed in Å.

The self consistent Green's function has been calculated onto a mesh of 32 energy points in the complex plane while for the LDOS calculation an equally spaced mesh on an a line in the complex plane has been used. An imaginary part of energy of the order of 1.4 eV has been chosen for such a mesh. As this value is large when compared with the linewidth of the resonances, a subsequent extrapolation of the LDOS on the real axis has been performed through a rational interpolation procedure (147). The LDOS shown in the following are calculated, where not otherwise declared, within a sphere of radius 2.64 Å, in order to show the contribution localized on the neighbouring of the adatom. Increasing the integration volume the contribution of the substrate states becomes more important.

The LDOS are split in their $l, m$-resolved components. Due to the cylindrical symmetry of the system $l$ is no more a good quantum number and a $m$-resolved analysis would be more appropriate. Nevertheless also the $l$-resolved analysis can be useful in order to assign the atomic resonances on the basis of their relationship with the atomic parent states, identified by the quantum numbers $n, l, m$.

The results discussed in the next sections have been obtained assuming that the effective potential inside the embedded sphere matches with an LDA effective potential outside, i.e., a potential that displays an exponential decay in vacuum. In practice the positive potential tail of the clean surface, that we use to construct the external potential in the 3D calculation, has been obtained, as explained in Chapter 2, considering $V_{eff}$ for the clean surface which decays toward the vacuum as an exponential function. This choice can give a good general description of the adatom-induced electronic properties and allows a first accurate analysis of them. Nevertheless a slower decay of the potential in the vacuum, typical of the image potential, can affect the spectral properties of the system, even if the entity of the changes is quite small. The effect of the image tail will be discussed in Sec. 4.1.5. The results shown there have been obtained using a $V_{eff}$ for the clean surface

with an image potential in vacuum and thus employing in the 3D calculation a $V_{ext}$ which accounts for such a behaviour.

### 4.1.2 LDOS of alkali on Cu(111): binding energy and lifetime of the main adatom induced resonances

Approaching the surface the alkali-metal atomic levels shift toward higher energies due to the net repulsive interaction with the surface (see Ref. (166)). In addition, due to the spatial proximity, their wave-functions start to hybridize with substrate states, resulting in resonances. The substrate band structure plays a fundamental role in this energy broadening. Indeed in order that an hybridization can take place, substrate states must be available at the same energy of the shifted atomic levels. Consequently if the band structure is characterized by an energy gap, the number of such states is considerably reduced.

In this sense the modulated potential used in this work, which reproduces the experimental gap, increases the quality of results with respect to the jellium case. In addition the appropriate description of the surface barrier, that corresponds to fixing correctly the vacuum level, allows to determine the binding energy of the resonances with more accuracy.

It is worthwhile to stress that, because $\mathbf{k}_{\|}$ is no more a good quantum number, the effect of the hybridization is spread on the whole surface Brillouin zone, i.e. it involves all the states characterized by different value of $\mathbf{k}_{\|}$ that are available at the fixed energy.

Let us now consider the $l, m$-resolved LDOS's reported in Fig. 4.3, 4.5 for the lighter alkali adatoms, namely Li and Na.

The main feature in the occupied spectrum is a peak at about -0.4 eV characterized by $m = 0$ character, i.e., $\sigma$ symmetry. This feature, which has both $l = 0$ and $l = 1$ contributions can be identified as the localized Shockley state of the clean surface. It was demonstrated by Simon (143) that a localized attractive perturbation caused by an impurity, such as for example an adatom, on a 2D electron gas (2DEG) always gives a bound state. Such a localization has been observed not only for alkali adatoms (60) but also for paramagnetic and magnetic adsorbates on noble metals (105).

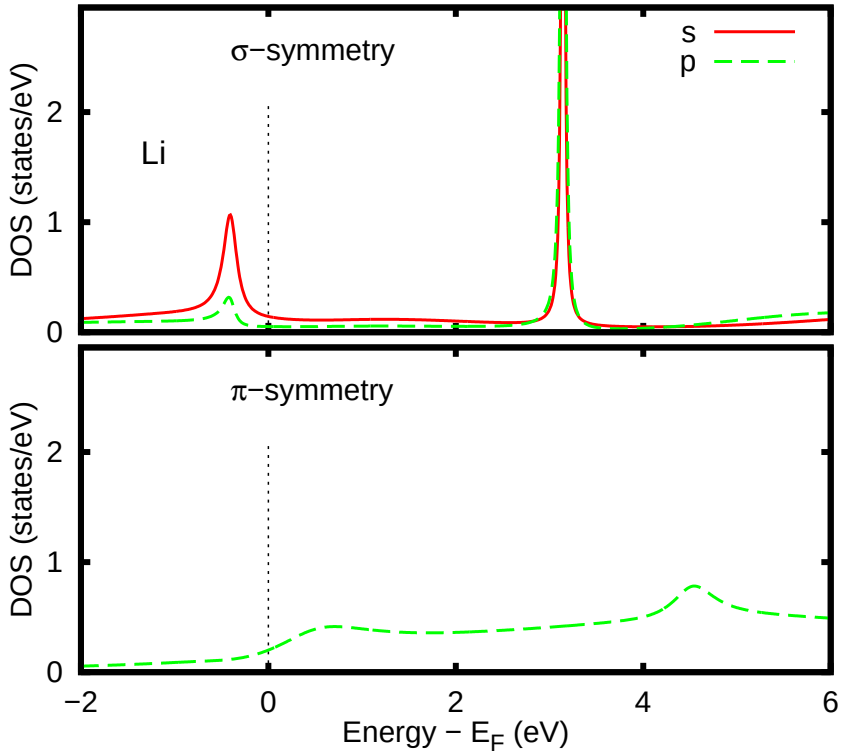


Figure 4.3: Local density of states of Li single adatom on Cu(111), resolved in $m$ and $l$ contributions.

The localized state appears as a peak in the LDOS, slightly below in energy with respect to the position of the step corresponding to the Shockley state observed in the clean surface (see Chapter 3). In Fig. 4.4 the $l = 0, m = 0$ component of the LDOS of the adsorbed system has been compared with the same component for the clean surface. Please note that the reference for the energy axis is the position of the Shockley state of the clean Cu(111) surface. We find that the localization amounts to 0.16 eV.

In the unoccupied part of the spectrum a narrow resonance at about 3 eV above the Fermi level is found. This state displays $m = 0$ character and can be identified as the $\sigma$ resonance of an alkali adatom on Cu(111). This is the main resonance observed for such a system which has been the object of both experimental and theoretical works (11; 17; 117; 149; 166). Since the early works

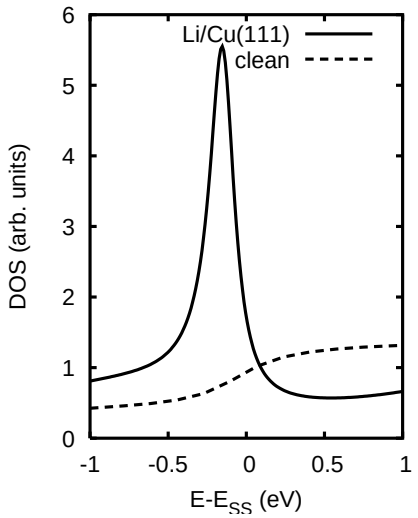


Figure 4.4: Adatom-induced localization of the Shockley state. The $l = 0, m = 0$ components are shown, for both the LDOS of Li/Cu(111) and the clean surface. The energy is given with respect to the binding energy of the Shockley state of the clean surface.

on jellium the characterization of such a resonance has been controversial. In particular many purposes were done in past years regarding its assignment to a parent atomic level. There are no doubt that it is related to the $ns$ valence state of the alkali-metal, as confirmed also by the $l = 0$ contribution in the LDOS. In addition a $l = 1$ contribution is found. Theoretical studies on jellium consider this resonance as a product of hybridization between $ns$ and $np$ atomic states (10; 111; 117; 119; 167), in particular between $ns$ and $np_z$. This statement requires some considerations. As suggested by Muscat-Newns (111) the hybridization between atomic levels can take place if their energy separation upon adsorption is larger than the linewidth that they acquire due to the interaction with the substrate states. On jellium this is always verified for these levels because the resonances width is of the order of 1 eV (119). Differently, in our calculation the resonances are much narrower than in jellium (see the figures) and the occurrence of the hybridization is not obvious.

The projection of the $l = 1$ component of the LDOS on the $l$ atomic orbitals of the isolated atom would clarify if the $l = 1$ observed contribution corresponds

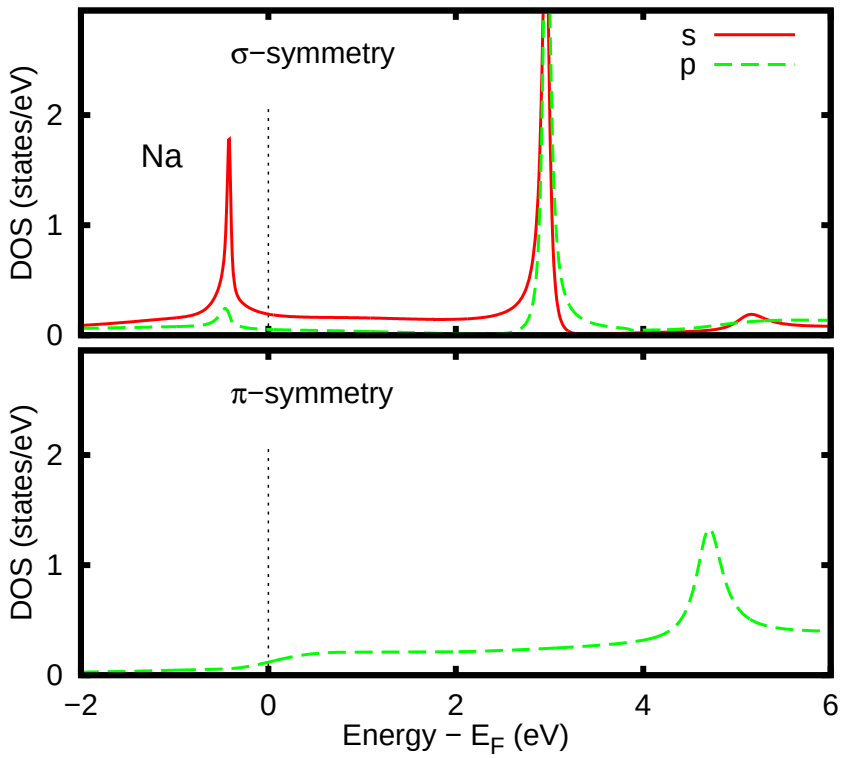


Figure 4.5: Local density of states of Na single adatom on Cu(111), resolved in $m$ and $l$ contributions.

to the $np$ atomic level. This analysis has not yet been performed thus we will limit to some general considerations.

Let us consider what happens in the Na case. The energy separation between the $3s$ and the $3p$ levels in the isolated atom is about 2.2 eV. Approaching to the surface these states shift upward to higher energy. The magnitude of the energy shift depends mainly on two factors: the spatial localization of the atomic wave-functions and their symmetry. In practice extended orbitals average the surface potential over a large region and consequently the shift varies more smoothly with the distance than spatially localized states. In addition if the wave-function of these states is oriented perpendicular to the surface the effect of the repulsive image potential will be stronger than for states oriented parallel to the surface. Thus $p_z$ states shift more than $p_x$ and $p_y$.

From our LDOS emerges that the energy separation between the $3s$ ($m = 0$, $l = 0$) and the $3p_x, 3p_y$ ($m = 1$, $l = 1$) levels stays equal to 2.2 eV also upon adsorption. Their linewidth is on the contrary considerably smaller, so that no hybridization can take place. The $3p_z$ ($m = 0$, $l = 1$) level in the LDOS has nearly the same binding energy of the $3s$ so that one could suppose that this state shifts less than the $p_x$ and $p_y$, differently from the expected behaviour. As these states almost coincide in energy their hybridization should be obvious but the unexpected small shift questions the assignment to the $np_z$ atomic level.

The nice picture of a gradual shift and evolution of the atomic states with the distance is however quite misleading. Indeed in the adsorbed system the meaning of $l$ is no more preserved. Due to the cylindrical field of the surface the $m$ degeneracy is lifted and different $l$ components can contribute to the same $m$ state. This is indeed what happens for the main resonance $\sigma$ in which both $l = 0$ and $l = 1$ contributions are found. We can conclude that the $\sigma$ resonance has also a $p_z$ character but it is not appropriate to state that it derives from the $np_z$ atomic level.

In addition to the $\sigma$ resonance another alkali induced feature is found at higher energy. The $m$-resolved analysis allows its unambiguous assignment to an adsorbate-localized state oriented parallel to the surface, i.e. with $\pi$ symmetry ($m = 1$).

As already mentioned above, the scientific relevance of the $\sigma$ main resonance became clear since the first experimental determination of its extremely long lifetime (11).

There are many decay mechanisms that contribute to this lifetime but the resonant charge transfer (RCT) from the adatom to the surface seems to be the most relevant one (59). It consists in the charge transfer (tunneling) of one electron from the adatom to the metal states available at the same energy. This energy conserving process constitutes the elastic contribution to lifetime and can be extracted from the linewidth of the resonances in the LDOS. This width, which is the effect of the interaction between the adatom levels and the continuum of the substrate states, can be estimated through the theoretical methods that are able to account for the semi-infinite character of the system.

Other methods that deal with a finite calculation region estimate the linewidth from the envelope function of the discrete peaks that compose the resonance. This procedure is conceptually misleading and gives values that differ from the experimental result, see for example the recent theoretical work for Li/Cu(111) in Ref. (116). We found a linewidth for the $\sigma$ resonance of the order of some tens of meV for lighter alkali and also smaller for the heavy Rb and Cs (the numerical values are reported in Tab. 4.2).

The difference with respect to the calculation on jellium suggests that the electronic properties of the substrate play a fundamental role. Differently from jellium the modulated potential accounts for the presence of the energy gap in the band structure of Cu(111). The effect of the gap on the RCT process is to prevent the transfer of electrons from the adatom toward the substrate, due to the absence of substrate states available to be occupied. Nevertheless the energy gap is not absolute but it varies with $\mathbf{k}_{\parallel}$ so that this blockade effect is only partial. The sketch in Fig. 4.6 can help in understanding this point. The picture reports the band structure of Cu(111) along a high symmetry path in the surface Brillouin zone and the energy position of the adatom induced resonances (that are $\mathbf{k}_{\parallel}$ independent because they are atomic features).

The $\sigma$ resonance has a binding energy that falls within an energy gap for a quite large range in $\mathbf{k}_{\parallel}$. Due to the small number of substrate states available at the $\sigma$ resonance binding energy, the hybridization with the substrate is small.

Differently, the atomic resonances that lie higher in energy, such as for example the $\pi$ resonance ($l = 1$, $m = 1$), have more states available to hybridize with. Indeed also states at $\Gamma$ can be found at that energy and this gives a linewidth one order of magnitude larger.

In addition to the energy position there are other two aspects that can influence the linewidth: the spatial extension of the states and their symmetry. Concerning the former, it is possible to observe that states with the same binding energy but different extension in space have different linewidth. This is because there is a sort of selectivity on the $\mathbf{k}_{\parallel}$ values that characterize the substrate states available for tunneling process. Indeed the more resonance wave function is extended in space, the more it can be described by Fourier coefficients characterized by small values of $\mathbf{k}_{\parallel}$. Consequently states that extends largely in space couple

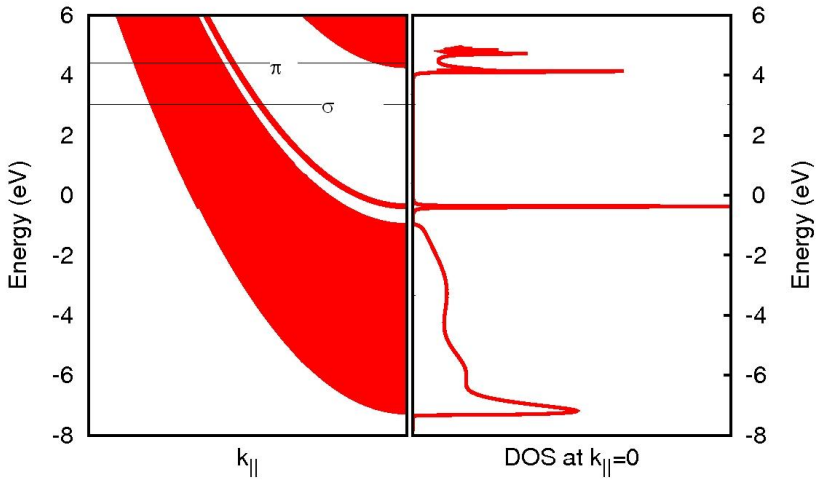


Figure 4.6: Band structure of Cu(111) and adatom induced resonances.

preferably with substrate states around $\overline{\Gamma}$. Also the symmetry of the resonance affects its linewidth because the tunneling process is favoured if the wave functions are oriented toward the surface. This aspect can be put in evidence considering the high energy resonances of the heaviest alkali adatoms. The LDOS's of K, Rb, Cs (Fig. 4.7, 4.8, 4.9) exhibit also states of $l = 2$ symmetry that are related to the first excited atomic $d$ state.

Regarding for example the LDOS of K, a $l = 2$, $m = 0$ contribution is visible at around 4.2 eV, identifiable as a $\sigma'$ resonance. At the same energy also the $l = 2$, $m = 1$ component is found, that combine with the $l = 1$,$m = 1$ to give the already mentioned $\pi$ resonance. Although the $\sigma'$ and $\pi$ resonances are at nearly the same energy and are both localized in space their linewidth appears considerably different due to their different orientation with respect to the surface. Indeed the $m = 0$ state is directed toward the surface so that the RCT process results more efficient than in the $m = 1$ case (parallel oriented).

The LDOS of the heavy alkali adatoms are characterized also by a $l = 2, m = 2$ resonance which can be identified as $\delta$. This resonance, which derives from the $d$ atomic level, is quite broad, confirming the higher degree of hybridization of the states with higher spatial localization.

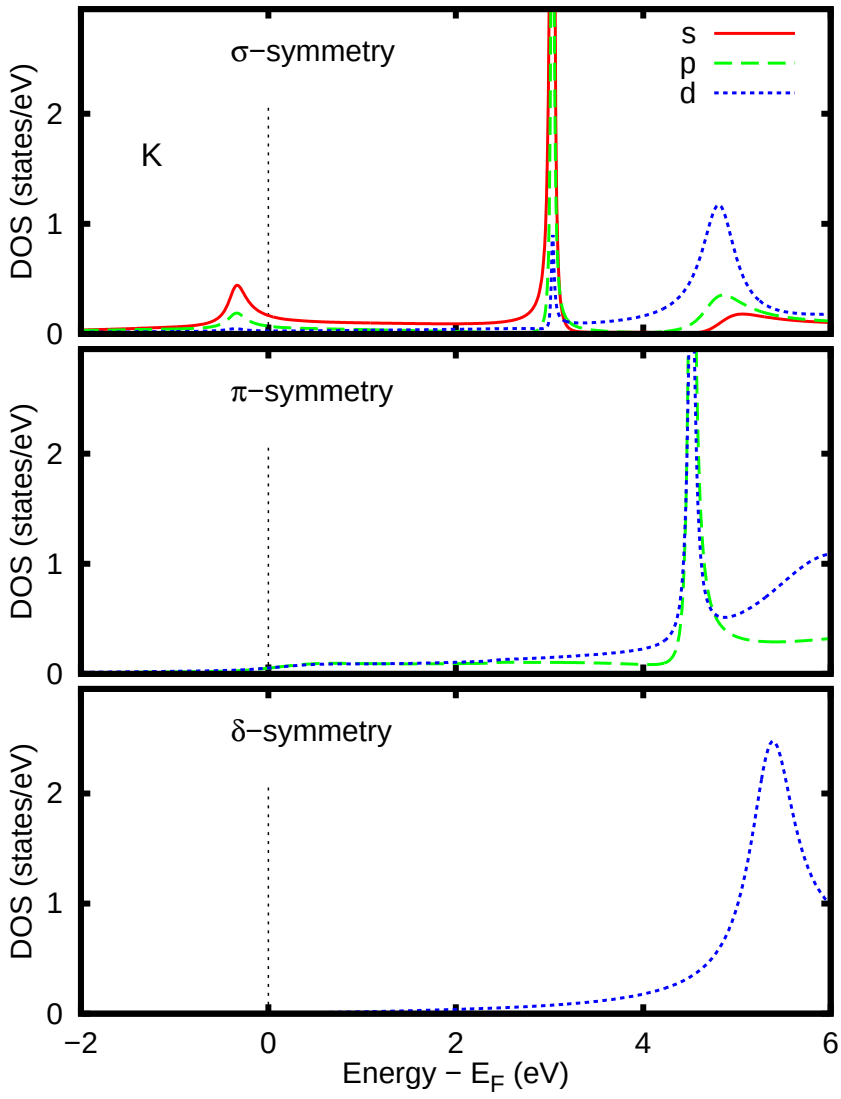


Figure 4.7: Local density of states of K single adatom on Cu(111), resolved in $m$ and $l$ contributions.

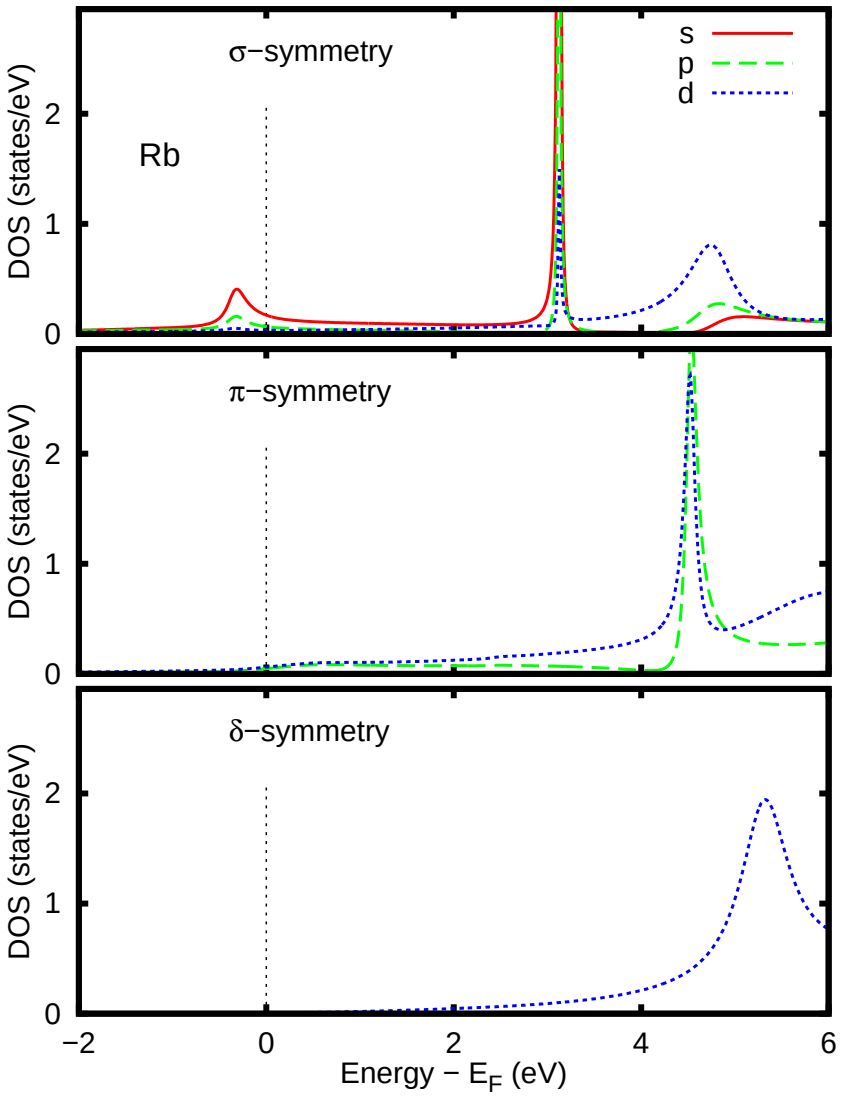


Figure 4.8: Local density of states of Rb single adatom on Cu(111), resolved in $m$ and $l$ contributions.

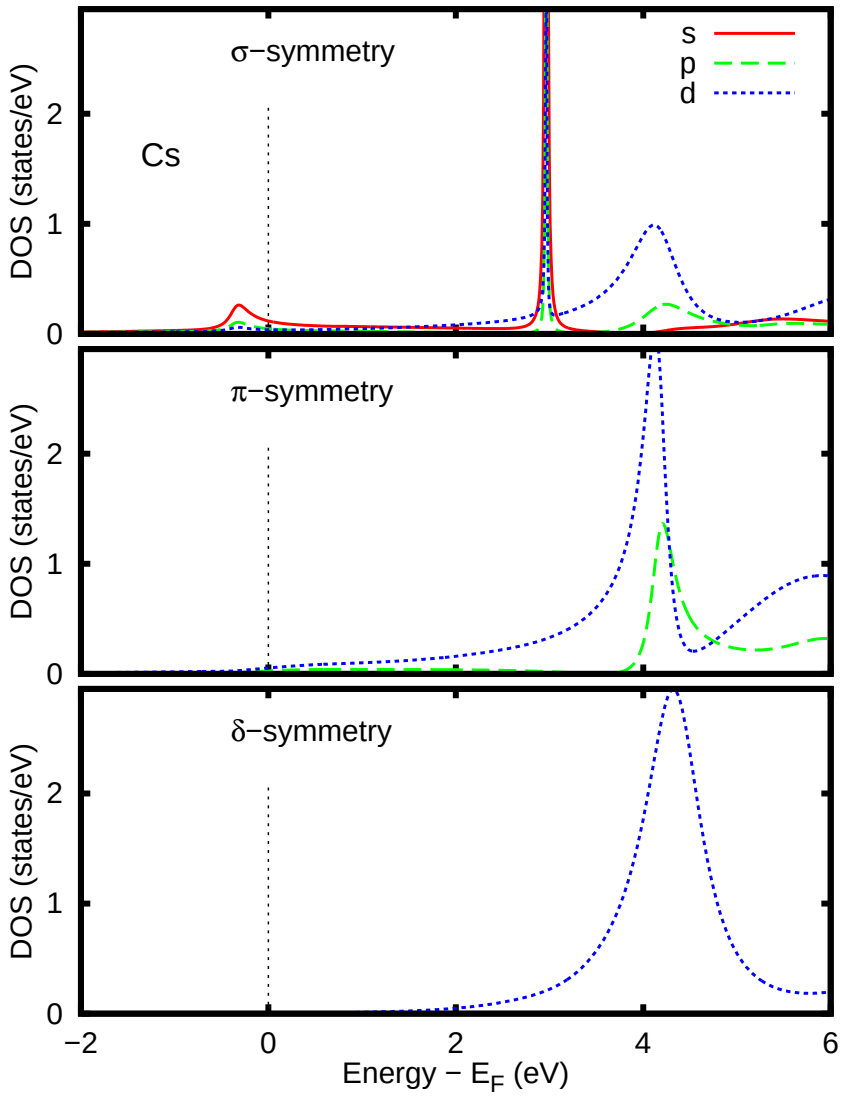


Figure 4.9: Local density of states of Cs single adatom on Cu(111), resolved in $m$ and $l$ contributions.

Table 4.2: Calculated energy and linewidth ($\Gamma_{el}$) of the $\sigma$, $\pi$, $\delta$ resonances.

| $\sigma$ | E (eV) | $\Gamma_{el}$ (meV) |
|---|---|---|
| Li | 3.14 | 36 |
| Na | 2.96 | 96 |
| K | 3.03 | 24 |
| Rb | 3.12 | 16 |
| Cs | 2.97 | 8 |
| $\pi$ | $E$ (eV) | $\Gamma_{el}$ (meV) |
| Li | 4.57 | 500 |
| Na | 4.71 | 336 |
| K | 4.54 | 100 |
| Rb | 4.50 | 124 |
| Cs | 4.13 | 346 |
| $\delta$ | $E$ (eV) | $\Gamma_{el}$ (meV) |
| K | 5.51 | 486 |
| Rb | 5.35 | 944 |
| Cs | 4.26 | 444 |

As a summary of the spectral properties of alkali on Cu(111) the binding energies and resonance linewidths are reported in Tab. 4.2.

The binding energy of the $\sigma$ resonance is found to be nearly period independent while its linewidth reduces passing from Li to Cs, probably because the adsorption distance is larger for the heaviest alkali atoms. This trend can not be observed for $\pi$ and $\delta$ resonances that are anyway broader.

### 4.1.3 Charge transfer and dipole moments

The charge transfer that occurs when alkali atoms are adsorbed on noble metals has been object of analysis in past years (15; 21; 81; 123; 158). In particular Ref. (21; 158) were devoted to the estimation of the amount of the electronic charge transferred and to the characterization of its spatial localization. The aim of this kind of analysis was to clarify the nature of the chemical bonding (81;

123). Nevertheless the scientific contributions relative to this topic are in general controversial and the debate about the ionic or covalent nature of the bonding did not found an unambiguous answer. The point is that the the physical properties that make the interaction ionic or covalent are not clearly and universally defined, so that sometimes this discussion becomes partly semantic. In this context the aim is not to give any evidence as support of one of these two pictures. We will limit to give an estimation of the charge transferred and of the dipole moments and we will do some considerations about the redistribution of the electronic charge of the system upon adsorption of alkali atoms. The purpose is indeed to show how the self consistent embedding approach gives an appropriate description of the charge transfer without requiring any initial assumption relative to the charge state of the constituent elements.

The first quantity analyzed is the variation of the valence charge within a sphere of radius $R$ centered on the adatom, due to the adsorption of the alkali atom. It is defined as follows:

$$\Delta Q(\mathbf{R}) = \int_{|\mathbf{r}|<\mathbf{R}} d^3\mathbf{r} \left[\rho(\mathbf{r}) - \rho_{clean}(\mathbf{r})\right]. \tag{4.1}$$

This quantity is reported in Fig. 4.10 for Na/Cu(111). In a very small sphere, i.e., in the atomic region, no difference is found with respect to the clean surface. Increasing the radius of the sphere the charge difference starts to grow, for $R$ between 1.5 Å and 3 Å and reaching the value of 0.79 electrons for $R = r_{emb}$.

We conclude that the valence electron is transferred to the substrate and 0.21 electrons lie outside the embedding sphere.

Although the difference charge can give a qualitative evidence of the charge transfer, it does not allow to argue anything about the spatial localization of the alkali valence electron. Nevertheless the rapid increase of the difference charge for $R$ between 1.5 Å and 3 Å suggests that the electronic charge accumulates in the spatial region between the adatom and the surface.

Let us consider in more detail the spatial distribution of the electronic charge. In the left panel of Fig. 4.11 is reported the electronic charge density for Na/Cu(111) evaluated in the embedding sphere. From the picture one can note an high density region both in front of the adatom on the surface side and just within the

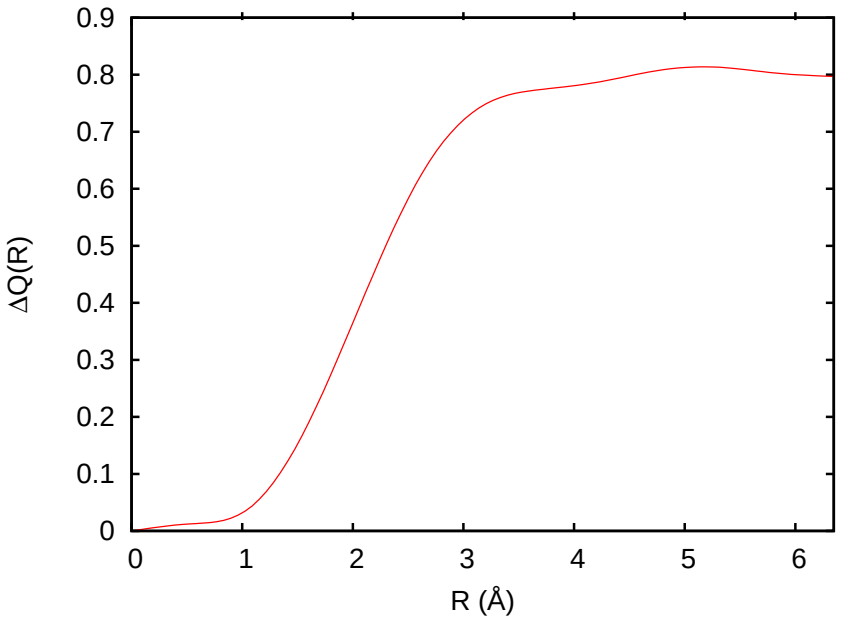


Figure 4.10: $\Delta Q(\mathbf{R})$ for Na on Cu(111).

substrate. The Fig. 4.11 displays also the contour plots of the *induced charge* and the *difference density* in the central and right panel respectively. These two quantities are defined as follows (140): the induced charge is obtained subtracting the charge density of the clean surface to that of the adsorbed system

$$\rho_{ind}(\mathbf{r}) = \rho(\mathbf{r}) - \rho_{clean}(\mathbf{r}), \tag{4.2}$$

while the difference density is deprived also of the charge density of the isolated atom

$$\rho_{diff}(\mathbf{r}) = \rho(\mathbf{r}) - \rho_{clean}(\mathbf{r}) - \rho_{atom}(\mathbf{r}). \tag{4.3}$$

Both $\rho_{ind}(\mathbf{r})$ and $\rho_{diff}(\mathbf{r})$ have been considered neglecting the contribution from the core states.

The induced charge evidences a depletion of electrons just inside the surface (blue dashed contour lines) and the presence of a local maximum in the electronic charge in front of the adatom at 1.11 Å from the surface. This maximum joins to a quite spherical distribution of electronic charge around the adatom. This positive-valued induced charge (red continuous lines) in the region between the

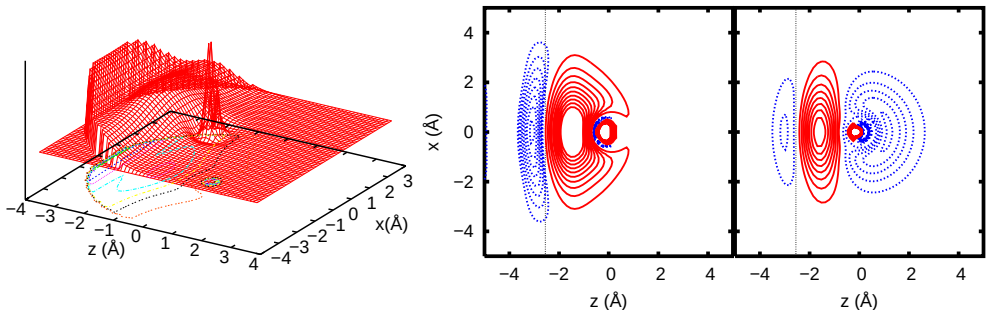


Figure 4.11: Charge density of Na/Cu(111). Left panel: total charge density. Central panel: induced charge density. Right panel: difference density. Blue (dashed) and red (solid) lines correspond to negative and positive values, respectively.

adatom and the surface has contributions from the valence electrons of both the substrate and the alkali adsorbate.

Subtracting the charge density of the isolated atom the ionization of the adsorbate becomes more evident. The difference density is negative inside the surface and also in the atomic region, demonstrating that the alkali-metal has lost part of its valence electron and it is partially ionized. The response of the system to the adsorption of a positive charged atom induces an electronic density localization just outside the surface. This screening charge is constituted by the valence electrons of the metal that spill out from the surface and localize themselves on the image plane, which is located at 1.11 Å from the surface ionic coordinate (32). The negative screening charge and the positive ion are the responsible of the surface dipole generated upon adsorption of the alkali-metal.

The surface dipole can be estimated through the integral:

$$\mu = \int d^3\mathbf{r}\rho(\mathbf{r})z. \tag{4.4}$$

The results obtained for the different alkali atoms are reported in Tab. 4.3. The surface dipole moment grows with the atomic number $Z$. This behaviour can be explained considering the definition of the dipole moment for two point charges: $\mu = qz$. The heavy alkali adatoms have a larger adsorption distance thus it is expected that they produce a larger dipole moment, assuming the same charge polarization for all the alkali. In reality the different dipole moment is partially

| Adatom | Li | Na | K | Rb | Cs |
|---|---|---|---|---|---|
| Dipole | 1.16 | 1.39 | 1.95 | 1.96 | 2.16 |

Table 4.3: Dipole moments (in a.u.) of alkali adatoms on Cu(111) adsorbed at the equilibrium distance.

due to the different charge reorganization induced by alkali with different $Z$, as it will be discussed in the next section.

### 4.1.4 Dependence of the electronic properties on the adsorption distance

The electronic properties analyzed in the previous sections are the effect of the mutual interaction between the adsorbate and the substrate. Such interaction becomes stronger during the approaching of the atom to the surface. In particular the electronic charge organizes itself in a dynamic way when the adatom-surface distance is progressively reduced. Dealing with a static configuration of the system we can not analyze this dynamical behaviour. Anyway, performing a series of calculations for different adsorption distances it is like considering a sequence of frames in such approaching to the surface. In Fig. 4.12 and Fig. 4.13 the induced charge density and the difference density of K/Cu(111) are depicted for different adsorption distances.

From these figures it is evident that the more adsorption distance is reduced the more we find a spherically shaped reorganization of the induced electronic charge both inside and outside the surface. Nevertheless the screening electronic charge has always its centre of gravity on the image plane, as can be evinced from the induced charge densities. On the contrary in the difference densities the centre of gravity of the positive part (red continuous lines) progressively moves toward the vacuum, according to the adatom adsorption distance. This is because in this quantity also the polarization of the adatom upon adsorption is included.

The analysis at different distances allows to study also the variation of the surface dipole moment approaching to the surface. The results obtained for Na and K are displayed in Fig. 4.15. The surface dipole exhibits a linear dependence

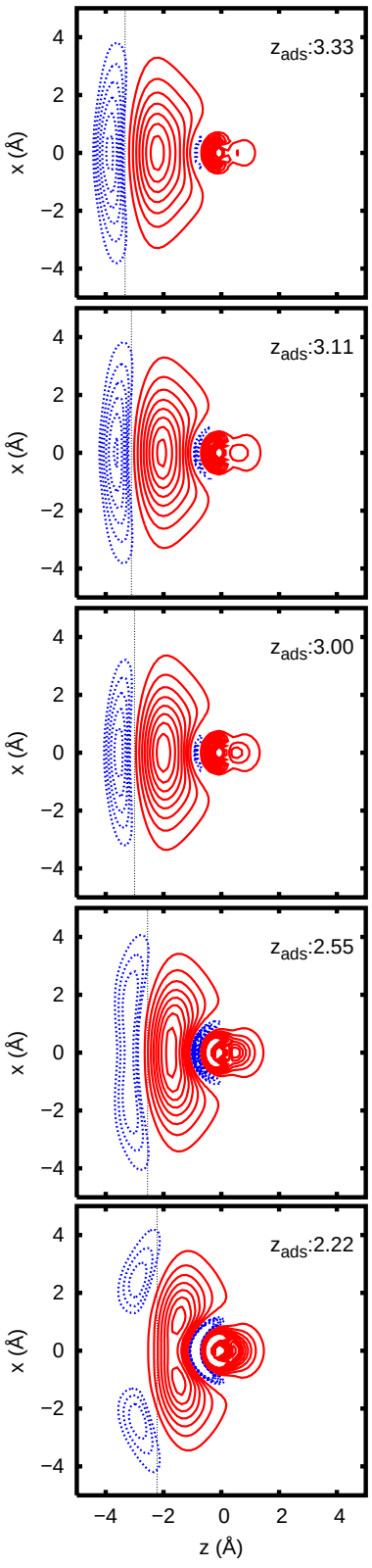


Figure 4.12: Induced charge density for K/Cu(111) at different adsorption distances. The dashed vertical line indicates the position of the surface.

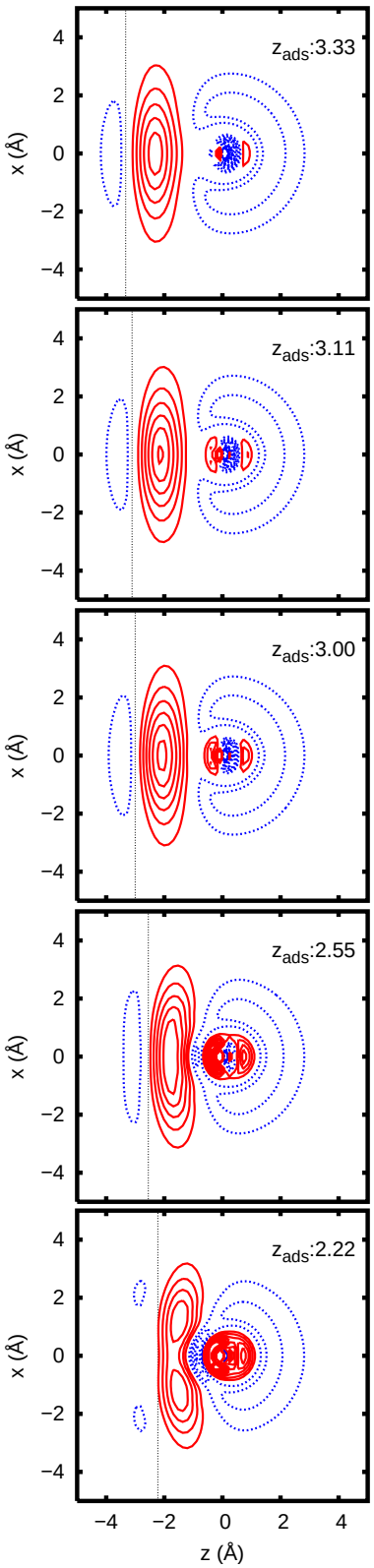


Figure 4.13: Difference density for K/Cu(111) at different adsorption distances.

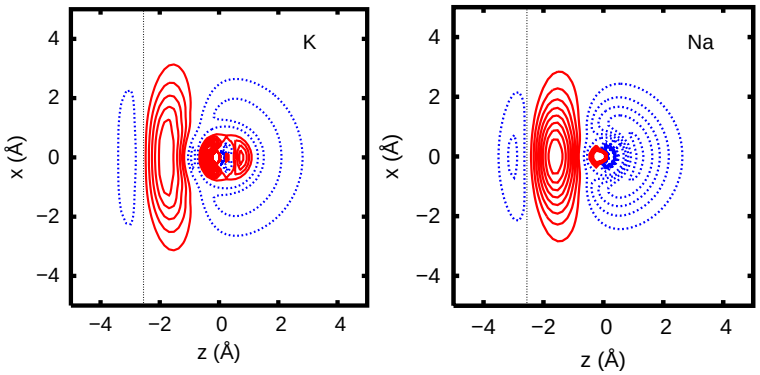


Figure 4.14: Difference density for K/Cu(111) and Na/Cu(111) at the same adsorption distance, namely 2.55 Å. Blue (dashed) and red (solid) lines correspond to negative and positive values, respectively.

on the adsorption distance, as expected for an ionic bond (140). In addition the dipole moment induced by adsorption of Na is lower than that due to K, for every adatom-surface separation. In order to explain such a behaviour let us consider the difference charge density of both K and Na at the equilibrium adsorption distance of Na (2.55 Å). They are reported in Fig. 4.14.

From the comparison it is evident that the lighter alkali atom induces a more conspicuous reorganization of the electronic charge, as evidenced by the major number of contour lines both inside and outside the surface (please note that the contours level have been truncated at 0.005 a.u. and the spacing between two lines is 0.0005 a.u.). In addition the distance between the maximum of the screening charge and the adatom is smaller in Na case than in K. As this distance is the quantity that effectively affects the dipole moment, more than the adsorption distance, a lower value of $\mu$ in the Na case is consistent with the behaviour observed in Fig. 4.15.

The charge density plots reported above have shown that depending on the adsorption distance and on the atomic number of the adatom, the electronic charge of the system reorganizes itself in order to produce an efficient screening of the induced perturbation.

One can imagine that the net effect of the charge redistribution due to the adsorption is the transfer of a net amount of electronic charge from the adatom

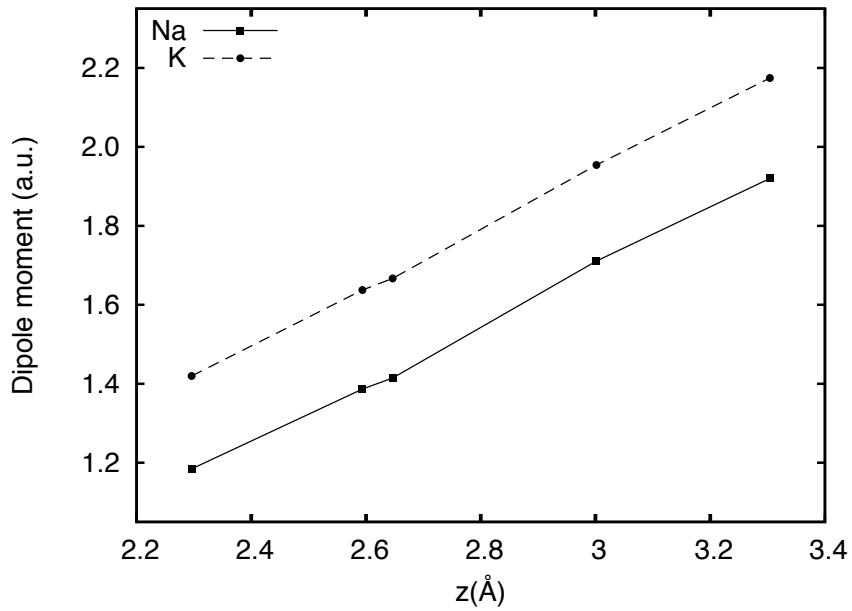


Figure 4.15: Dipole moment of Na and K on Cu(111) as a function of the adsorption distance.

to the substrate which is different from the expected value of one electron. This is indeed the final effect of two opposite contribution: the difference in the ionization potential and the screening response of the metal. The amount of electrons *effectively* transferred is commonly a fractional quantity that can be viewed as the effective charge responsible of the surface dipole. The effective charge is defined from the relationship:

$$\mu = q^* z \tag{4.5}$$

where $z$ is the adsorption distance, and can be thus estimated through:

$$q^* = d\mu(z)/dz \tag{4.6}$$

The effective charge can be deduced from the Fig. 4.15: the slope of $\mu(z)$ results equal to 0.35 both for Na and K. The net value of 0.35 electrons is very similar to the value of 0.4 found for Na on Al(111) (21).

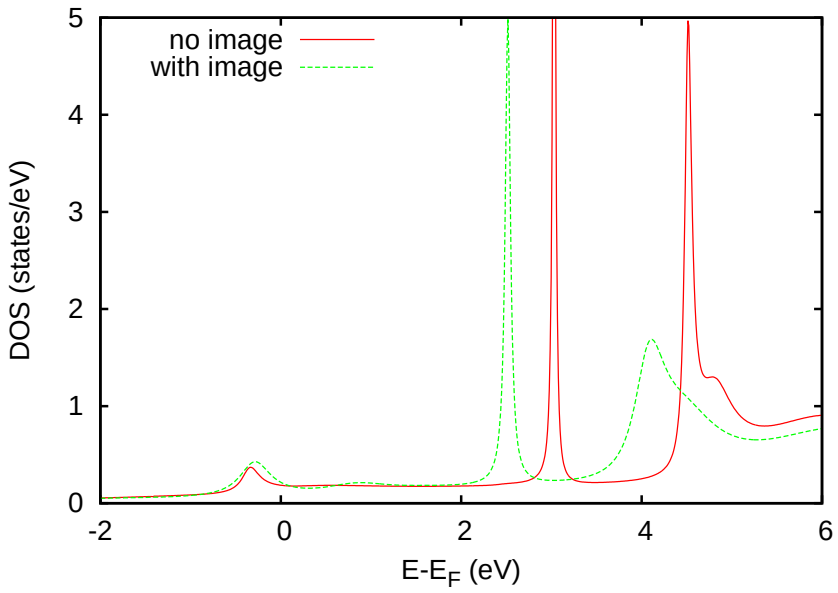


Figure 4.16: Comparison of the total local density of states of K/Cu(111) with (dashed line)and without (solid line) the image tail in the potential.

### 4.1.5 Inclusion of the image potential tail

The results discussed up to this point have been obtained supposing an exponential behaviour of the potential in vacuum, thus neglecting the long range image term which is the typical potential experienced by one electron in front of a metal surface.

The inclusion of the image tail gives an effective potential which is lower than the LDA one in front of the surface. As a consequence the electrons see a different barrier in the vacuum and this can induce some changes in the electronic properties of the system. We have analyzed in Chapter 2 the changes in the LDOS of the clean surface due to the inclusion of the image tail in the potential.

In analogy with what is observed for the Shockley state of the clean surface, adatom-induced resonances are expected to shift toward lower energies. In order to analyze the effect of the inclusion of the image tail we report in Fig. 4.17 the LDOS of K/Cu(111) obtained requiring a long range decay for the potential outside the embedded region. The LDOS has to be compared with that reported

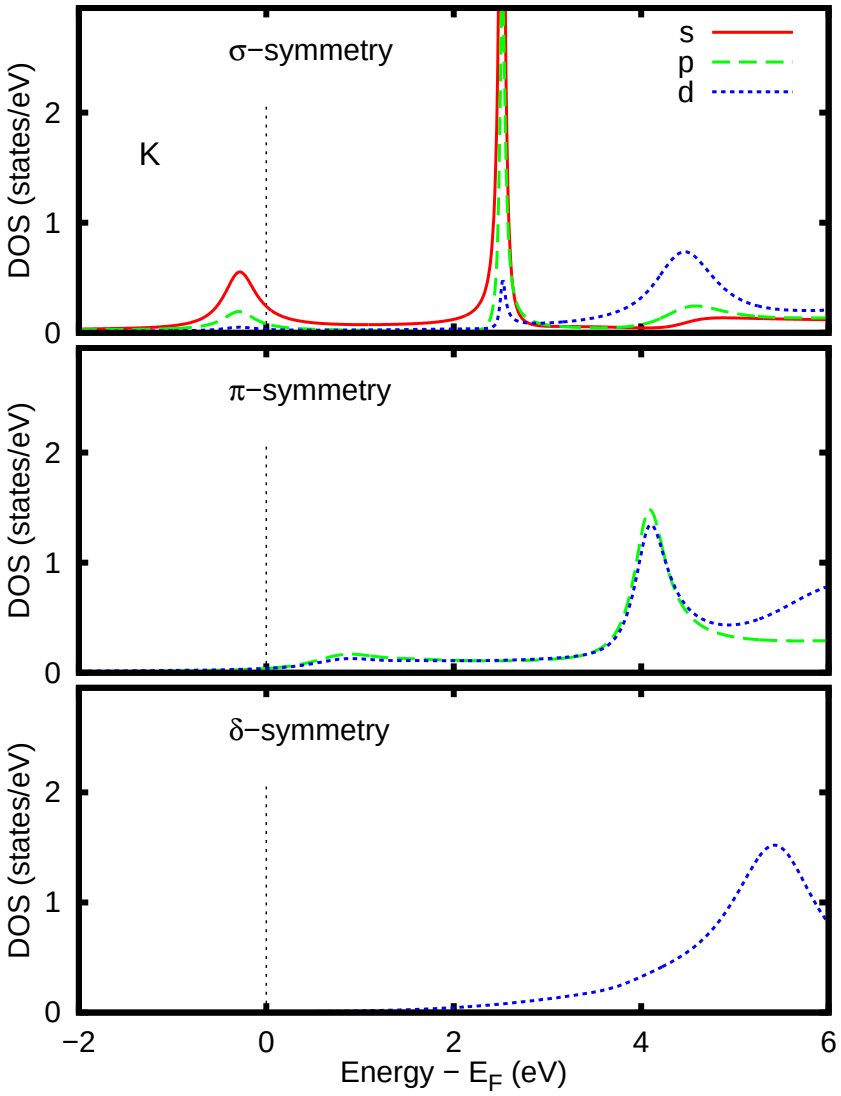


Figure 4.17: Local density of states of K single adatom on Cu(111), resolved in $m$ and $l$ contributions, with the image potential tail included in the calculation.

in Fig. 4.7. For the comparison we can refer to Fig. 4.16 that displays the total LDOS of K/Cu(111) for the two cases. Both the $\sigma$ and $\pi$ resonances are shifted of 0.5 eV and 0.6 eV respectively. However the $\delta$ resonance maintain nearly the same energy position. This is because near to the vacuum level the variation of the surface potential barrier due to the inclusion of the image tail is less than at lower energies. Another point is the variation of the linewidth. The resonance are in general larger. For what concerns the $\sigma$ resonance this can be explained by the larger number of substrate states at the new binding energy of the resonance. In the case of $\pi$ resonance the linewidth is enhanced also by the hybridization with the $n = 1$ image state which lies at 4.12 eV in the clean surface. The same holds for the $\delta$ resonance which hybridizes with image states at higher energy.

## 4.2 Single Ba atom on Cu(111)

One of the advantages in using the embedding method to treat adsorption is that it allows to consider any atomic species as adsorbate. On the other hand, other state of the art methods, such as WPP or CAM require the presence of only one active electron in the system and thus are not suitable for application to adatoms with many valence electrons. In this section the results obtained in the embedding formalism for a Ba single adatom on Cu(111) will be presented. The scientific literature for this rare-earth metal on surfaces is not as rich as for alkali adatoms. Some works were devoted to the change of the work function induced by this adsorbate (138; 165). Recently a joint experimental and theoretical study of the electronic properties of Ba on Cu(111) varying the coverage has been performed through a comparative analysis of the results obtained both by one and two photon photoemission experiments and by embedding calculation (4). The results presented in this section have been obtained in an embedding sphere of radius $\sim 6$ Å and with a setting of parameters analogous to that adopted for alkali atoms. The adsorption distance, equal to 2.61 Å has been taken from DFT calculation for a dilute $(7 \times 7)$ phase (4). In Fig. 4.18 it is reported the LDOS for Ba on Cu(111). In this case the $l$-resolution has been chosen as the main criterion for separating the contributions to the LDOS, while the $m$-resolution is given inside each panel. This choice is motivated by the relevance of the $6s$

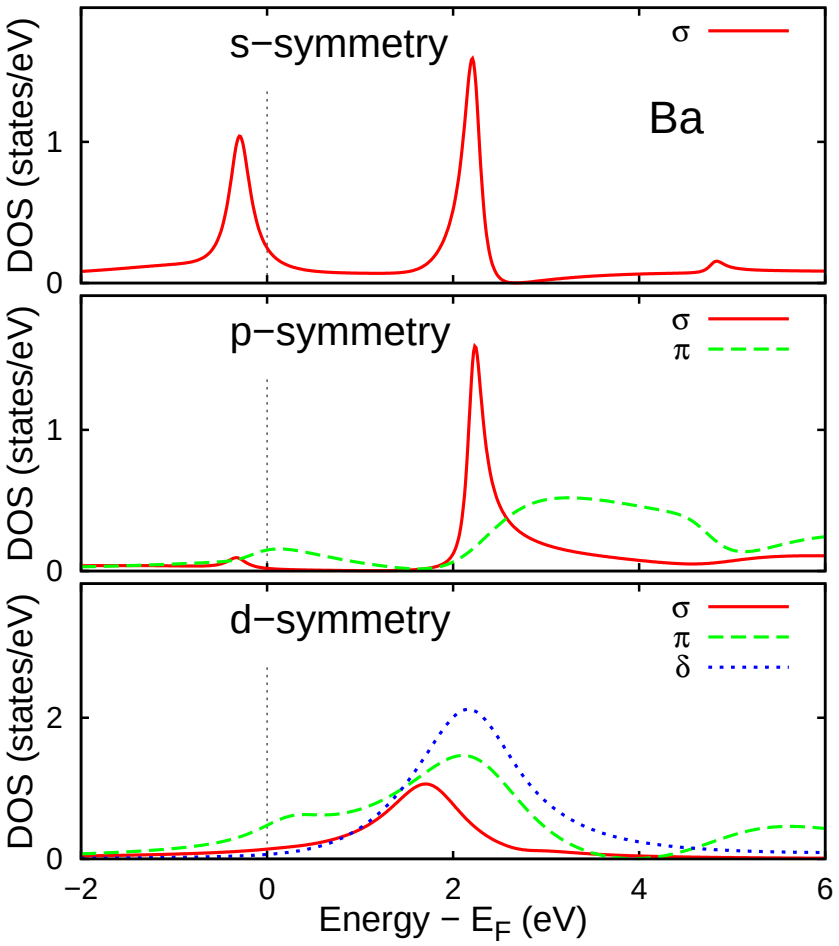


Figure 4.18: Local density of states of Ba single adatom on Cu(111), resolved in $l$ and $m$ contributions.

state of Ba in determining the induced spectral properties. In addition such a representation is preferred in perspective of comparison with experimental results that show mainly the $s$ components due to the larger transition moment of states with $l = 0$ symmetry.

The atomic resonances of Ba on Cu(111) display an higher binding energy with respect to the alkali atoms, because the Ba core produces a stronger attractive potential. The $l = 0$ component to the LDOS exhibits two peaks that can be related to the $6s$ state of Ba which splits in two contributions. This behaviour is typical of a covalent bonding in which two states (bonding and antibonding) are

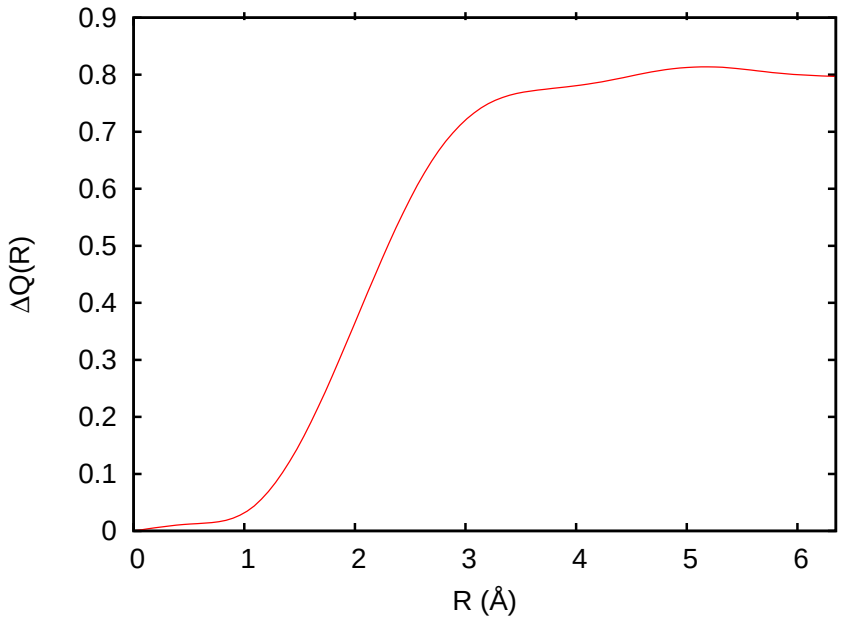


Figure 4.19: $\Delta Q(\mathbf{R})$ for Ba and Cs on Cu(111).

formed.

In the case of Ba/Cu(111) the bonding state lies in correspondence of the Shockley state of the substrate. Although this fortuitous coincidence can generate some doubt on this assignment, there is much evidence of the exactness of such interpretation. First of all the two $l = 0$ peaks have nearly the same height, differently from the alkali atom case, in which the localized Shockley state was considerably smaller than the main atomic resonance. One can suppose that, in analogy with the alkali LDOS, the $l = 0$ contribution to the Shockley state is of the same order of magnitude of the $l = 1$ one (see central panel in Fig. 4.18), while the remaining density of states at that energy has to be related to states of different nature.

Also the analysis of the charge transfer confirms the presence of an occupied bonding level. In Fig. 4.19 is reported the difference charge $\Delta Q(\mathbf{R})$ of Ba/Cu(111) in comparison with that of Cs.

The picture shows that in a spherical volume that contains only the adatom ($R \sim 2$ Å) more electronic charge is found for Ba than in the alkali atom case. In this volume 0.1 and 0.8 electrons are found for Cs and Ba respectively, supporting

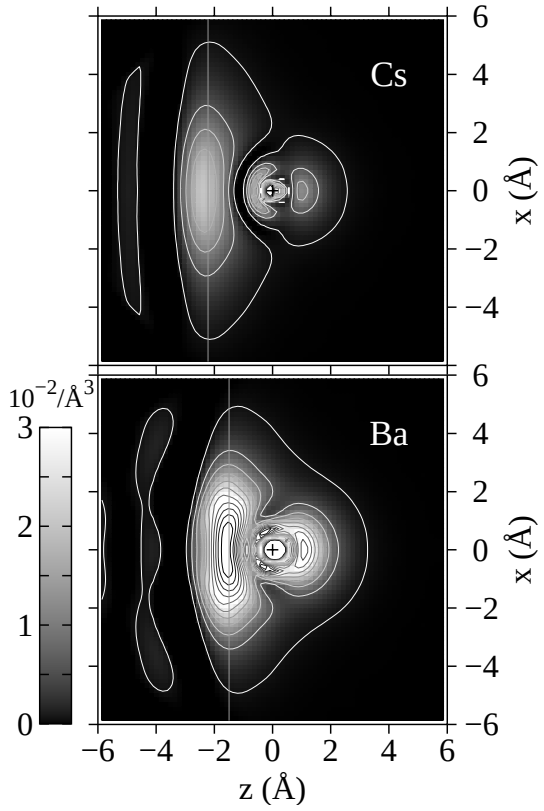


Figure 4.20: Spatial charge distribution of Cs and Ba on Cu(111).

the hypothesis of an additional occupied level in Ba, not found in Cs. The spatial distribution of the electronic charge, reported in Fig. 4.20 in comparison with the Cs one, supports such interpretation. In addition to the screening charge that accumulates at the image plane, as in the alkali adsorption, the Ba case presents an additional charge distribution centred on the atom, that can be related to the $s$ valence electron in the bonding level.

Furthermore the bonding-antibonding picture is supported also by the experimental results. The 1PPE spectra at $\overline{\Gamma}$ is reported in Fig. 4.21 as a function of the Ba coverage. The picture shows that the initial Ba deposition causes a broadening of the occupied feature and a reduction of its intensity. At higher coverages the lineshape is asymmetric presenting a tail that extends toward the Fermi level. This suggests the coexistence of two spectral features: one related to the Shockley state and the other to the bonding resonance. The same inter-

pretation is confirmed also by the angle resolved 1PPE spectra in Fig. 4.22 that shows, along an high symmetry path, in addition to the dispersive Shockley state, a hint of a non-dispersing feature that can be related to the adatom-localized $\sigma$ resonance.

For what concerns the other contributions to the LDOS, the $p_z$ component ($m = 0$) coincides in energy with the unoccupied $l = 0, m = 0$ peak, contributing to the main $\sigma$ resonance, as already found for alkali adatoms. The $p_x, p_y$ resonance ($\pi$) appears at higher energy, 0.5 eV above the main $\sigma$ resonance, according to the experimental findings. In addition a large $l = 2$ contribution is found at about 2 eV above the Fermi level, that contains all the $m$ components and has to be related to the $d$ atomic level.

All the Ba resonances are in general quite broad if compared with the heavy alkali adatoms ones. This is mainly due to the smaller adsorption distance of Ba with respect to Cs, Rb, K. This enhances the overlap with the continuous band of Cu(111). The linewidth of the $\sigma$ resonance of Ba is comparable to that of Na on Cu(111), which has slightly shorter adsorption distance than Ba.

In addition the main unoccupied $\sigma$ resonance has a different energy position in the energy gap. Due to its higher binding energy, the number of substrate states available for hybridization is larger than for alkali adatom case. For the $\pi$ resonance this effect joins with the $\mathbf{k}_\parallel$ selectivity discussed above, giving a greater broadening of the atomic level. Indeed the substrate states at this energy, that are available for the overlap, are characterized by large $\mathbf{k}_\parallel$ values, resulting in an enhanced hybridization with the localized $\pi$ states (characterized by high $\mathbf{k}_\parallel$ Fourier components).

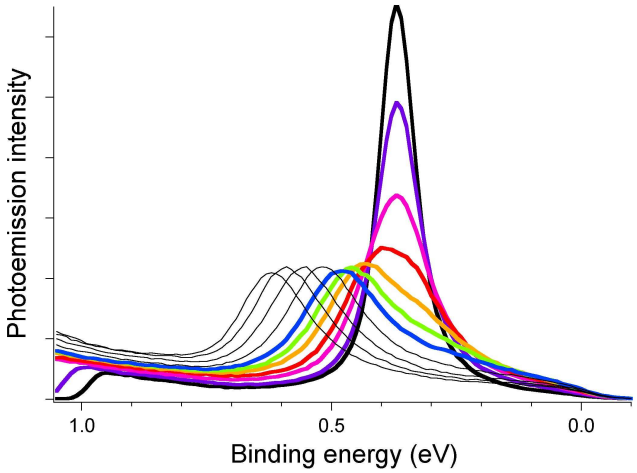


Figure 4.21: 1PPE spectra for Ba/Cu(111) at increasing Ba coverage. The more intense peak corresponds to the Shockley state of the clean surface. These data are taken from Ref. (4).

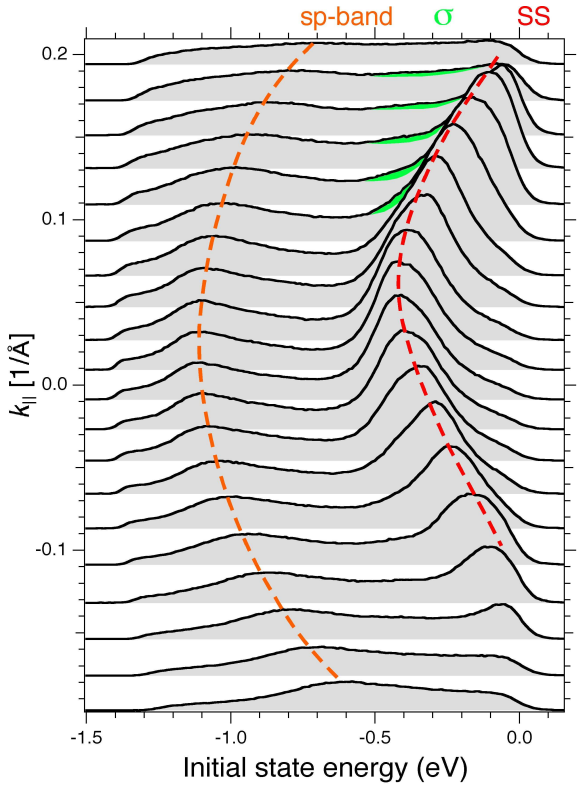


Figure 4.22: Angle resolved 1PPE spectra for Ba/Cu(111) from Ref. (4).

# Part II

# Embedding method applied to realistic systems: thin films on metal surfaces

In the second part of this thesis the results obtained for the electronic properties of thin films on metal surfaces are analyzed. The aim is to discuss some peculiar aspects of these low dimensional systems, also connected to the experimental analysis.

First of all a brief overview on the computational aspects relative to the embedding implementation for realistic surfaces will be given in Chapter 5.

The last three chapters are devoted to the application of such a method. The three systems analyzed here can be considered as representative of different physical properties due to the different chemical nature of their constituent elements, both of the surface and of the overlayer.

The alkali film on noble metal substrate is a milestone of the scientific literature, due to its technological and fundamental interest. Despite the really simple electronic structure of alkali, this system displays interesting properties for the surface localized electronic states. In particular the theoretical analysis relative to alkali on Cu(111) will be performed from a fundamental point of view, discussing the different broadening of surface specific features as a consequence of a surface reconstruction.

Copper can be also a good substrate for the growth of adlayers of heavy elements such as Bismuth. In this case our theoretical analysis is a support to the experimental one and it is devoted to understand the interplay of electronic and structural properties.

The third system, oxygen film on an iron surface, allows to consider the electronic imbalance due to the magnetic character of the surface. In such a case the theoretical analysis joins to an experimental investigation performed through scanning tunneling microscopy (STM) and spectroscopy (STS), showing other physical properties accessible through the applied theoretical method.

# Chapter 5

# Embedding for realistic surfaces

The study of realistic surfaces through the embedding method is really more complex than the model presented in the first part of this thesis. The real geometrical configuration of the atoms, both in the surface plane and in the normal direction (surface relaxation) has to be considered. As a consequence the calculation of the embedding potential becomes more demanding. Indeed the embedded region adopted for the calculation is chosen in such a way that it contains some crystal layers (the number depends on the screening properties of the substrate) and a portion of vacuum outside the surface. On the crystal side the embedding potential should be defined on a curly surface $S_C$ that tracks the undulating profile of the spherical volumes that define the last atomic layer included in the calculation. This leads to a quite difficult evaluation of the matrix elements. A further difficulty in using a realistic surface potential instead of a pseudopotential concerns the description of the rapid oscillations of the wave-functions near to the atomic nuclei. The solutions adopted to overcome these points will be the object of this chapter together with a general overview of the implementation of the embedding method for realistic systems.

## 5.1 Embedding potential for realistic surfaces

The drawback in the calculation of the embedding potential can be overcome using the method proposed by Crampin *et al.* (37) that consists in displacing the embedding potential on an equivalent plane surface $S$, which is separated from

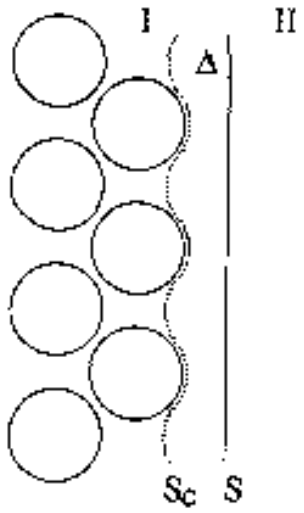


Figure 5.1: Geometry adopted for the evaluation of the embedding potential on the crystal side.

$S_C$ by a non-physical buffer space $\Delta$ (see Fig. 5.1). In this method the wave-function $\phi$ is defined in the volume $I + \Delta$ and matches on $S$ to the free electron wave-function $\chi$. Both $\phi$ and $\chi$ satisfy on the surface $S$ the boundary condition in Eq. (1.9), where $G$ is the free particle Green's function with zero normal derivative on $S$. Because the potential in $\Delta$ is constant, the two functions evolve in the same way and thus they exhibit the same amplitude and logarithmic derivative also on $S_C$. In this way, if the the logarithmic derivative of $\chi$ on $S_C$ matches to that of the bulk solution, the boundary conditions on $S$ are automatically fixed, giving a wave-function $\phi$ which is the solution to the Schrödinger equation in $I$ with the right normal derivative on $S_C$. In practice the embedding potential on $S$ furnishes the same solution that one would obtain considering the embedding potential on $S_C$. For the construction of the embedding potential on $S$ different methods have been proposed (37; 83; 162). In the embedding code used in this thesis the Ishida implementation has been adopted. The details of the calculation can be found in Ref. (162).

## 5.2 The FLAPW basis set

In the proximity of the atomic nuclei the wave-functions are strongly varying and nearly spherical, while in the spatial region between the nuclei they are smoother. It is thus convenient to use a basis set that reproduces such a behaviour. The Full Linearized Augmented Plane Waves (FLAPW) basis set is suitable for this aim. This provides a different basis expansion in two different region of space: the spherical volumes centred on the atomic nuclei (*muffin tins*) and the interstitial region between them.

$$\psi(\mathbf{r}) = \begin{cases} \sum_{\mathbf{G}} c_{\mathbf{G}}(\mathbf{k}) e^{\mathrm{i}(\mathbf{k}+\mathbf{G})\cdot\mathbf{r}} & \mathbf{r} \in \mathrm{I} \\ \sum_{lm} \left[ A_{lm}(\mathbf{k}+\mathbf{G}) u_l(\mathbf{r}) + B_{lm}(\mathbf{k}+\mathbf{G}) \dot{u}_l(\mathbf{r}) \right] Y_{lm}(\Omega) & \mathbf{r} \in \mathrm{MT} \end{cases} \tag{5.1}$$

Within the muffin tins (MT) atomic like basis functions are defined. The $u_l(E, r)$ are the solutions of the radial Schrödinger equation:

$$\left( -\frac{d^2}{d\mathbf{r}^2} + \frac{l(l+1)}{\mathbf{r}^2} + V(\mathbf{r}) - E_l \right) \mathbf{r} u_l(\mathbf{r}) = 0 \tag{5.2}$$

where $V(\mathbf{r})$ is the spherical component of the potential within the MT, including also the core state. The use of a *full potential* allows to describe both valence and core states and to access to interesting quantities such as for example the core level shift.

The $u_l(E, \mathbf{r})$ are constructed on a radial grid and for a given set of values of E (*pivot energies*). During the self consistent procedure the variational freedom of the pivot energies allows a better description of the eigenvalues of the system. Also the derivatives $\dot{u}_l(\mathbf{r})$ are introduced with this purpose. Indeed, if the band energy differs slightly from the pivot, a simple Taylor expansion allows to describe the radial function at the correct band energy, with an error which is quadratic in the energy difference $(E - \epsilon)$.

$$u_l(\epsilon, \mathbf{r}) = u_l(E_l, \mathbf{r}) + (\epsilon - E_l)\dot{u}_l(\mathbf{r}) + O((\epsilon - E)^2). \tag{5.3}$$

In the region outside the MT the usual plane-waves are used. The two coefficients $A_{lm}$ and $B_{lm}$ that appear in the linear combination of the $u_l(E, \mathbf{r})$, and their

derivatives $\dot{u}_l(\mathbf{r})$ are determined requiring the continuity of both the amplitude and the radial derivative of the basis set on the MT boundaries. The FLAPW basis set is used also for the expansion of the charge density and the potential, that are evaluated in reciprocal space. These quantities require a larger cutoff on the basis functions, respectively two and four times that used for the wavefunction.

In order to reduce the computational effort the basis set is built in such a way that it exploits the crystal symmetries.

For the technical details about the construction of such symmetrized functions see Ref. (144).

## 5.3 Computational details

The preliminary step for the self consistent calculation at the surface is the determination of the unperturbed Green's function of the bulk, which is necessary for the calculation of the embedding potential. This calculation furnishes the effective potential in the bulk unit cell.

The second step consists in the construction of the embedding potential, exploiting the method described in Section 5.1. As by-product of the calculation, also the complex band structure is obtained (162).

Finally the *ab initio* calculation for the surface is performed within a finite embedded region.

Differently from supercell calculations, only few layers of bulk are enough to guarantee a good solution that matches correctly to the unperturbed one, thanks to the inclusion of the embedding potential in the Hamiltonian.

One of the fundamental step in the calculation is the input part. Some of the input data define the system (atomic coordinates, chemical nature of the atomic species, symmetry operators) and the general parameters of the calculation (cutoff for the basis set, radial grid, extension of the embedding region, MT radii, exchange-correlation functional). Other ones are instead fixed for a specific aim (energy path and mesh, $\mathbf{k}_{\parallel}$ points, Broyden parameters for the self consistency). After the reading of the input data an initial (guess) charge density is built up by superimposing the charge density of the unperturbed isolated atoms.

At this point the self-consistent cycle is entered: the effective potential $V_{eff}$ appearing in the Kohn-Sham set of equations is determined by computing separately the Hartree+nuclear part and the exchange-correlation part. At present in the code it is possible to evaluate the latter one using different approximations: in particular the Local-Density (LDA) and the General Gradient one (GGA) have been implemented in the code. Available parametrization are: the Perdew-Zunger (133), the Moruzzi-Janak-Williams (89), the Gunnarson-Lundquist (65) and the Von Barth-Hedin (157) for the LDA while it is possible to use the Perdew-Wang (134) and the Perdew- Burke-Ernzerhof (132) parametrization within GGA. At this level, the computation is split according to the number of $\mathbf{k}_{\parallel}$ points sampling the SBZ. In the following steps the embedding potential is read and the Hamiltonian matrix elements which do not depend on the energy are calculated; as the embedding potential matrix elements are energy dependent, a third loop is now entered in which the Green's function is determined at each energy point, inverting the $[H - EO]$ matrix, as shown in Eq. (1.20). An energy and $\mathbf{k}_{\parallel}$ dependent Green's function is now available; the imaginary part of its trace representing the output local density of states. The information concerning different $\mathbf{k}_{\parallel}$ points is now collected and the integration over the SBZ is performed; the output charge is then compared to the input one and, if they differ by more than a given threshold, the iterative cycle continues up to when convergence is reached. In order to have a smoother and faster convergence the output charge is mixed with the input one using the so-called Broyden algorithm (24).

### 5.3.1 Inclusion of the image potential

Within the embedding region the effective potential is evaluated in the Density Functional framework. Due to the local character of the functionals used for the exchange and correlation term, the long range behaviour of the potential in vacuum is not reproducible. In front of the metal surface the electrons experience a long range image potential:

$$V^{image}(z) = -\frac{1}{4(z - z_{im})} \tag{5.4}$$

where $z_{im}$ is the position image plane. This potential gives the asymptotic behaviour in vacuum and bounds the hydrogenic series of image states. In order to allow an appropriate description of such states, one should include a non local correction to the potential but the calculation would become quite demanding. Alternatively it is possible to use the procedure proposed by Nekovee and Inglesfield (113; 114). Assuming that the potential in vacuum has the image asymptotic behaviour reported in Eq. (5.4), they gradually mix the self consistent effective potential with the image tail:

$$V(z) = [1 - I_x(a,b)]V^{GGA}(z) + I_x(a,b)V^{image}(z). \tag{5.5}$$

This procedure gives in the near surface region a potential that accounts for the effect of the correct asymptotic behaviour in vacuum, although it differs from that reported in Eq. (5.4). Indeed the effective potential coincides with the perfect image potential only asymptotically in vacuum. The mixing procedure is realized through an incomplete beta function $I_x$ (3) that extends from the image plane up to the limit of the embedded region in the vacuum. This function that grows gradually from zero to one guaranties a continuous mixing of the two potentials. In Eq. (5.5) $I_x$ is given as a function of the reduced coordinate $x$ that is defined as:

$$x = -\frac{z - z_{im}}{z_{im} - z_s} \tag{5.6}$$

where $z_s$ is the starting point for the mixing and $z_{im}$ is the image plane. The parameters $a$ and $b$ define the slope of $I_x$ in passing from zero to 1. In particular the ratio $a/b$ is related to the centre of gravity of the function, while acting on the absolute value of $a$ and $b$ it's possible to change its curvature. Some test-calculations have evidenced that the calculated binding energy of the image states weakly depends on the choice of $a$ and $b$ in a wide range of values.

The last point which is worthy to be discussed regards the position of the image plane. In order to determine the image plane it is possible to exploit the non periodicity of the embedding method which makes the application of an external electric field normal to the surface plane an easy task to perform (85). It is then possible to calculate the centroid of the field induced charge distribution

which corresponds to the position of the static image plane as originally stated by Lang and Kohn (99). Indeed:

$$E_z z = \Delta\Psi \tag{5.7}$$

where $E_z = 4\pi\sigma$, $\sigma$ representing the induced charge. It is possible to rewrite Eq. (5.7) in terms of $\sigma$ and of the position of the image plane $z_{im}$:

$$\Delta\Psi = -4\pi\sigma(z_s - z_{im}) + A\sigma^2 \tag{5.8}$$

where $\Delta\Psi$ is the variation of the work function upon the application of the electric field.

# Chapter 6

# $p(2 \times 2)$-K/Cu(111)

Alkali metals on metal surfaces have been studied extensively for a long time. The main scientific interest was devoted to the structural configuration upon adsorption (41), to the nature of the chemical bonding (81; 123), and to the rich electronic properties of the system (16). In particular the electronic structure of one monolayer of an alkali metal on a metal substrate has been widely studied in recent years both from an experimental and theoretical point of view (7; 22; 28; 146). From the single adatom adsorption up to the completion of a monolayer, the electronic properties of the system are subject to a continuous modification that involves both the states of the pristine clean surface and the overlayer induced ones (49). Despite the simple electronic configuration of alkali adatoms, these low dimensional systems give the opportunity to observe and characterize electronic states of various nature. In particular the confinement of the electronic wave functions in the overlayer can be remarkable. The substrate band structure together with that of the adlayer can lead to the formation of a sort of a quantum well in which 2D state appears (26; 70; 106). This quantum well state (QWS) and other overlayer specific features will be the object of the present chapter.

In particular the role of the substrate band structure in the lifetime of the surface specific features will be discussed. This topic, already treated in Chapter 4 for a single adatom on Cu(111), returns here for a more intricate situation. The growth of one monolayer of alkali metal on such a surface is indeed associated with a surface reconstruction that determines a band folding into a smaller surface

Brillouin zone. The effect of such a folding is that the overlayer states that lie in the energy gap of the clean surface acquire an intrinsic elastic linewidth. The embedding method allows to estimate this elastic contribution. Furthermore the bulk bands of the pristine surface and the folded ones overlap in different way within the surface Brillouin zone. As a consequence also the linewidth has a not trivial dependence on $\mathbf{k}_{\parallel}$. In the following the *ab-initio* electronic properties of $p(2 \times 2)$-K/Cu(111) will be discussed. Recently the electronic properties of Na/Cu(111) (25) and Cs/Cu(111) (28) have been investigated by the embedding method. The recent experimental results (141) relative to $p(2 \times 2)$-K/Cu(111) motivated the extension of the theoretical analysis, performed through the same approach, also to this system.

## 6.1 Surface geometry

Many studies were devoted in past years to the surface configuration of adsorbed alkali atoms on noble metal substrates, in particular on Cu(111). Due to the low corrugation of Cu(111) the alkali adatoms are free to rearrange themselves on the surface.

Concerning the atomic configuration of K on Cu(111) LEED measurements (47) revealed an initial incommensurate reconstruction, that was identified as an hexagonal phase with the same orientation as the substrate. Increasing the coverage a long-ranged-ordered phase can be observed evolving into a clear commensurate $p(2 \times 2)$ phase. After further adsorption of potassium the phase becomes incommensurate again. The experimental analysis thus confirms the formation of a continuous hexagonal overlayer on the surface that constitutes a two-dimensional solid orientationally ordered on the copper substrate and without intermixing phenomena. This assertion is confirmed also by the linear relationship between the inverse square of the atomic spacing and the coverage, reported in Fig. 6.1. In particular the linearity is observed up to 0.3 ML. In order to follow the evolution of the surface configuration in the different phases as a function of K adsorbed and to unequivocally identify the completion of the first monolayer, a clarification about the definition of 1 ML coverage is necessary. It is indeed a common choice in alkali overlayer systems to define 1 ML such that it is normalized to

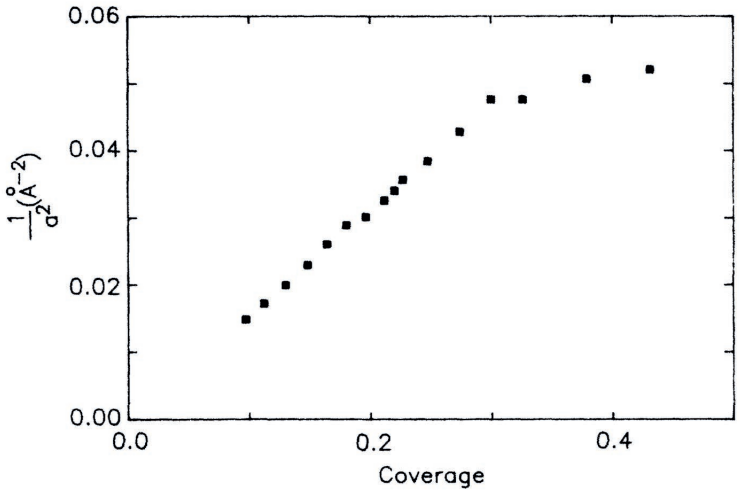


Figure 6.1: Relationship between inverse square of the potassium nearest-neighbour spacing $a$ and the K coverage on Cu(111) surface. From Ref. (47)

the nominal coverage (defined as the ratio between the number of adatoms and the number of substrate atoms per unit area) which gives a clear experimental evidence. For example Fischer *et al.* (49) fix the completion of the first monolayer at the nominal coverage at which the saturation of the work function is reached. In other works this assignment is made in correspondence of the maximum in the photoemission intensity of the state at the Fermi level. These two phenomena coincide within a 10% variation of coverage. As confirmed also by the data in Fig. 6.1 the completion of the first monolayer occurs at 0.3 of nominal coverage. Further adsorption of potassium leads to an out of plane reconstruction, that corresponds to a deviation from linearity. The $p(2 \times 2)$ phase (nominal coverage of 0.25) can be thus properly identified as the full monolayer within an error of about 10% with respect to 0.3 derived from Fig. 6.1. Nevertheless in the recent work of Schiller (141) the $p(2 \times 2)$ ordered phase has been assigned to a 0.75 ML, a coverage considerably smaller than 1 ML. This discrepancy is due to the erroneous definition of 1 ML in correspondence of a 0.4 nominal coverage in Fig. 6.1 where a saturation regime is already stabilized. In the following we will consider the perfect $p(2 \times 2)$ as the full monolayer and our theoretical results will be compared with those of Schiller at the same coverage. The $p(2 \times 2)$ phase

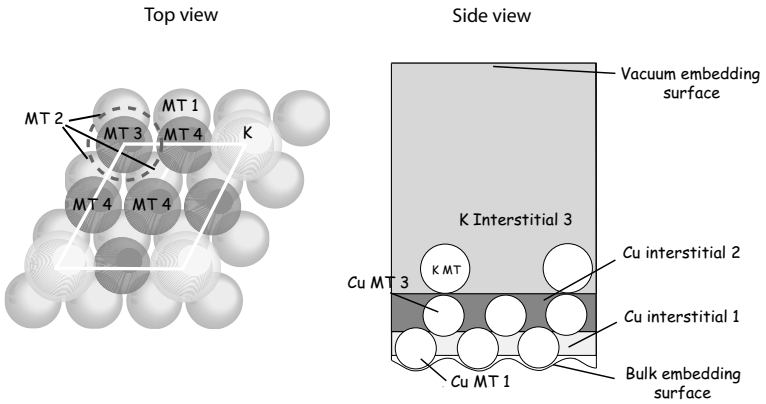


Figure 6.2: Sketch of the $p(2 \times 2)$-K/Cu(111) unit cell considered in the calculation.

has been characterized both by SEXAFS measurements (5) and theoretical calculations (42; 124; 125) in the past. All these investigations agree in attributing to the potassium adatoms an atop adsorption position, although a higher coordination site could be expected in such a system. Nevertheless experiments and theories (more than one theoretical method has been used) are not in agreement on the equilibrium adsorption distance. The experimental determination is 3.05 $\pm$ 0.02 Å, while the theoretical ones are in general shorter. Cluster calculations in DFT-LDA and Restricted Hartree Fock approach give respectively 2.90 Å and 3.00 Å (125). This last value was confirmed also by a Metropolis Monte Carlo simulation (124). A DFT slab calculation confirmed once again that the atop position is preferred, with an adsorption distance equal to 2.73 or 2.83 Å in LDA or GGA respectively (42).

## 6.2 Computational details

In the calculation we use the experimental adsorption distance (3.05 Å) that we retain as the more reliable one. The lattice parameter of Cu (3.61 Å) is used and the calculation is performed assuming no surface relaxation. In the plane of the surface the adatom-adatom distance is equal to a double lattice parameter of the Cu(111) surface unit cell. The embedded region chosen for the calculation extends for 15.34 Å. It includes two layers of the substrate (eight Cu atoms) and

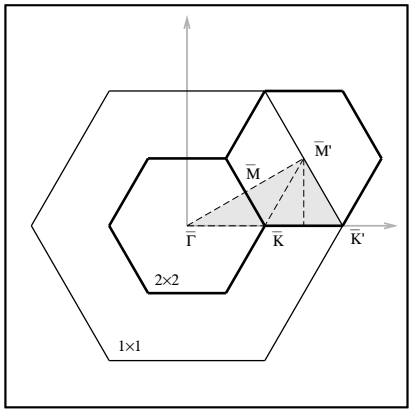


Figure 6.3: Surface Brillouin zone of $p(2 \times 2)$-K/Cu(111)

the overlayer (one K atom), while the remaining space is vacuum. In Fig. 6.2 a top view of the surface and the embedded region are reported.

For the calculation parameters, we have used 10.24 Ry as the cutoff for the plane wave expansion and $l_{max} = 9$ for the basis in the muffin tins. The muffin tin radii are respectively 1.06 Å for copper and 1.28 Å for K.

The surface Brillouin zone (SBZ) is sampled with a $(9 \times 9)$ regular mesh, that consist in 22 independent $\mathbf{k}_{\|}$ points. It is important to note that due to the surface reconstruction a mapping of the surface Brillouin zone of the pristine clean surface onto that of the overlayer occurs. The resulting SBZ is a quarter of that of Cu(111) and is obtained by the folding of the clean surface one, as depicted in Fig 6.3. Note that primed letters correspond to high symmetry point of the $(1 \times 1)$ SBZ of Cu(111).

The image state calculation is performed taking $z_{im} = 1.95$ Å from the K surface atom, as explained in Chapter 5. The densities of states that follow display a fictitious width due to the small imaginary part of the energy used in the LDOS calculation; where no differently declared this is equal to 2.27 meV.

## 6.3 Overview of the theoretical electronic properties

The first result concerns the work function reduction with respect to the clean Cu(111) surface. The reason for this reduction in the low coverage regime has been already discussed in Chapter 4. At 1 ML coverage the work function has reached the saturation value. This regime corresponds to the so called 2D condensation in which a metallic layer is formed. Indeed, increasing the number of adsorbates on the clean surface, the cohesion interaction between the K adatoms surpasses the interaction with the substrate due to the considerable overlap of the K valence states that form a surface band. The theoretical work function associated to such a metalization of the monolayer is equal to 2.07 eV, considerably smaller than the Cu(111) one, which is equal to 4.89 eV. Our results are in agreement with the experimental ones (2.27 eV and 4.93 eV respectively) despite a little discrepancy of 0.2 eV for the K-covered surface. This difference could be ascribed to the fact that the measured system could not correspond exactly to an homogeneous monolayer. Indeed the presence of impurities and defect can influence the work function.

A preliminary characterization of the electronic properties of the system can be deduced from the density of states in the SBZ. This one is reported in Fig. 6.4 for different spatial volumes.

Note that the DOS in the interstitial regions is considerably smaller than in the muffin tins due to the close packed nature of Cu(111). First of all it is possible to observe that the DOS of copper in the second layer (central panel) is narrower than the bulk DOS (first panel). This effect is attributed to the presence of the surface. In addition the DOS in the MT 3, which is just below the K atom slightly differs from that of its nearest neighbour. In particular a depletion of states is observed at around $-2$ eV while higher DOS is found around $-4$ eV. The third panel reports the DOS in the overlayer region and in the vacuum space. In this case the DOS is nearly equal in the two volumes. This allows us to conclude that the $s$ valence states of K are localized in the overlayer and in the near-surface region.

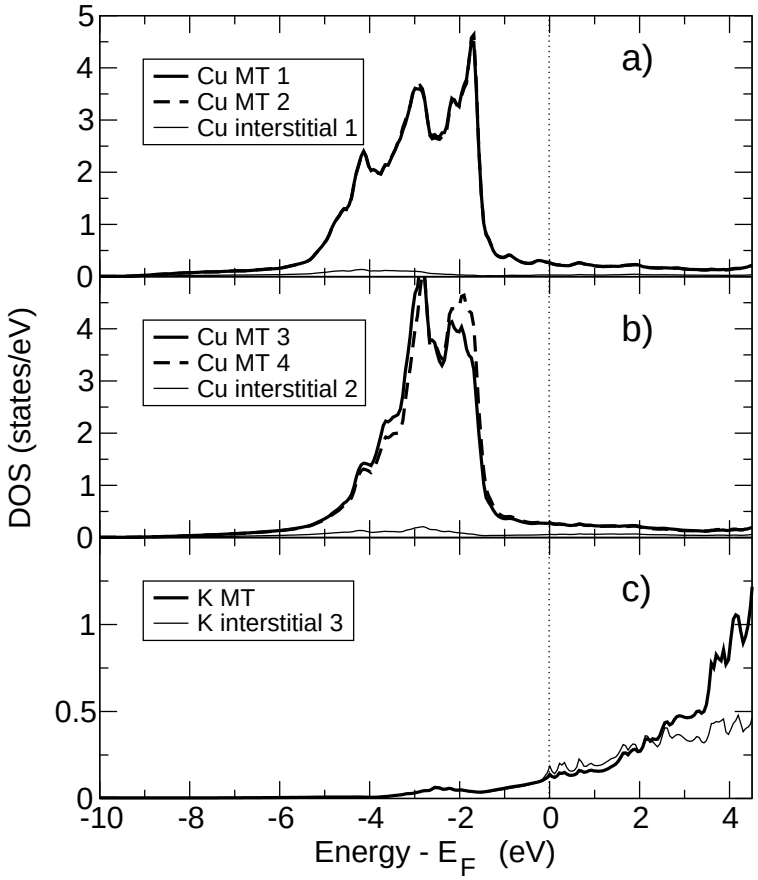


Figure 6.4: Density of states of $p(2 \times 2)$-K/Cu(111) in the surface Brillouin zone evaluated in different volumes.

The DOS in the SBZ is an averaged quantity, so that the single states can not be clearly identified. In order to characterize the surface specific electronic features a $\mathbf{k}_{\parallel}$ analysis is preferred.

### 6.3.1 $\mathbf{k}_{\parallel}$ resolved DOS

In Fig. 6.5 the DOS in the $\overline{\Gamma}$ point is reported, in the same volumes as above, with the exception of the copper interstitials that we verified to contribute poorly.

The upper panel displays the DOS in the Cu muffin tins. This is characterized by the high density of states corresponding to the $d$ band of the substrate that extends, in the $\overline{\Gamma}'\equiv\overline{\Gamma}$ point up to $-1$ eV. The clean surface exhibits at $\overline{\Gamma}'$ a surface projected energy gap in the energy range $-1$ eV, 3.75 eV. Note that theoretical energies of the upper and lower edge of the gap slightly differ from the experimental ones due to the well known DFT erroneous estimate of the bulk band edges. In the $\overline{\Gamma}$ point of the SBZ of $p(2 \times 2)$-K/Cu(111) an additional contribution to the DOS comes from the $\overline{\mathrm{M}}'$ point of the clean surface, due to the band folding. This density of states partially plugs up the gap, up to 1.5 eV. Close to the upper edge of this band the $n = 1$ image state is visible while the other image states accumulate at the vacuum level. The density of states from the vacuum level up to the upper edge of the $(1 \times 1)$ energy gap at 3.75 eV is due to the states of vacuum and merges in the upper $s$ band of copper.

In order to illustrate the electronic states induced by the K film, the analysis of the DOS localized in the overlayer and in the surface region (K interstitial) is the most appropriate. For this purpose the DOS at $\overline{\Gamma}$ shows the main surface electronic features of the system. Nevertheless the analysis along high symmetry paths in the $(2 \times 2)$ SBZ allows a more complete characterization. In Fig. 6.6 the DOS along the $\overline{\Gamma\mathrm{MK}\Gamma}$ path, evaluated in the K muffin tin is reported.

Let us analyze in detail the overlayer induced features at $\overline{\Gamma}$. The occupied spectrum is characterized by a broad feature near to the lower edge of the Cu(111) energy gap and by a narrow peak just below the Fermi level.

The broad surface resonance (SR) at about $-1.2$ eV is the evolution of the Shockley surface state of Cu(111) which, in the clean surface, is located in the surface projected energy gap. Photoemission experiments (49; 92; 141) have shown

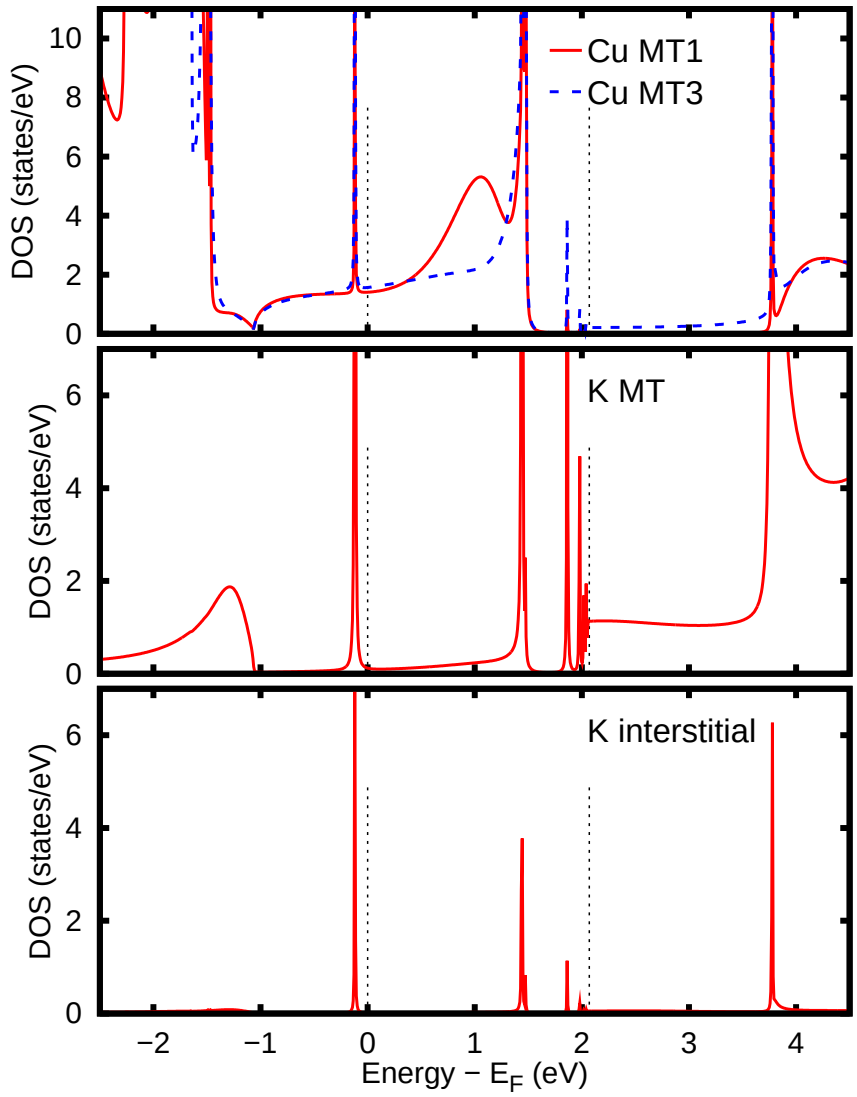


Figure 6.5: Density of states of $p(2 \times 2)$-K/Cu(111) at the $\overline{\Gamma}$ point, in different volumes (see Fig. 6.2). The vertical dashed lines indicate the Fermi level and the vacuum level.

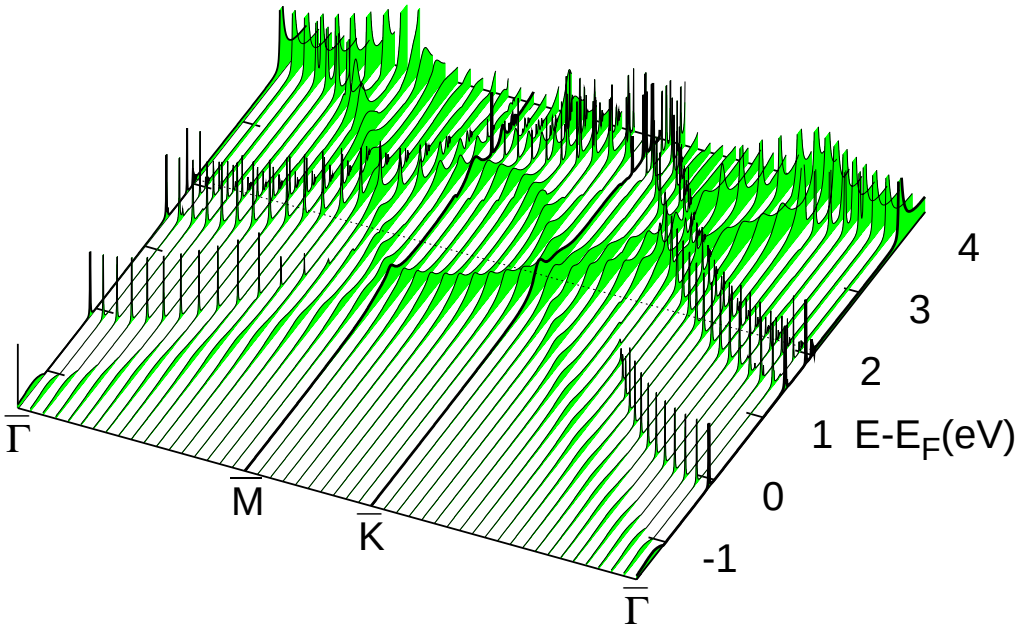


Figure 6.6: Surface band structure of $p(2 \times 2)$-K/Cu(111) along high symmetry paths in the surface Brillouin zone, evaluated in the K *muffin tin*.

that increasing the coverage of alkali adatoms the Shockley state shifts lower in energy until it disappears from the photoemission spectra when it crosses the edge of the *sp* band. Approaching to the bulk band, also the physical properties of such a state progressively change. Recent experiments have shown for example the variation of its effective mass for different alkali coverages (141). The energy shift has to be ascribed to the more attractive potential upon adsorption of K. When the Shockley state enters in the continuous band it hybridizes with the substrate states giving rise to a resonance which was observed also for Na and Cs films on Cu(111) (22; 28). Note that slab calculations give discrete overlayer states due to the finite extent of the slab, while the embedding method gives a broad resonance and it permits the estimate of its elastic linewidth. The elastic width of the surface resonance (and other states) will be analyzed in Section 6.3.2. The binding energy of the surface resonance at $\overline{\Gamma}$ can be compared with the experimental one reported by Schiller (141). The *ab initio* value of $-1.28$ eV slightly differs from the experimental one of $-1.05$ eV. The reason of this discrepancy is probably due to the error in the DFT estimate of the band edge. The

surface resonance is indeed pinned by the edge of the bulk band of Cu(111). In DFT this lower edge of the gap is slightly lower than the expected experimental position and this influences also the position of the surface resonance.

Due to its resonant character the SR can propagate also toward the bulk, as can be deduced from the density of states on the Cu atoms. Nevertheless the higher contribution in the K *muffin tin* demonstrates the overlayer character of such a feature. The localization on the overlayer could suggest a different assignment of this states, that can be related to the free-electron like energy band found by Wimmer in the free-standing K monolayer at slightly lower energies (160). This hypothesis is confirmed by the spatial distribution of the charge density, which is reported in the left upper panel of Fig. 6.8. This quantity has been obtained integrating the Green's function in the actual energy range of the surface resonance. In this plot the darker (lighter) regions correspond to larger (smaller) charge density. The charge density relative to the analyzed energy range show a contribution of $p$ symmetry on the Cu atoms, while a lower intensity of spherical charge distribution is observed on the K atom, in agreement with the assignment of this electronic feature to the $s$ band of the unsupported K overlayer.We conclude that the SR has a dual nature because it can be related both to the Shockley state and to the overlayer band. The substrate or overlayer character emerge in different way in different point of the SBZ. The Fig. 6.7 reports the surface resonance intensity in $\overline{\Gamma}$, $\overline{\mathrm{M}}$ and $\overline{\mathrm{K}}$ both in the K and subsurface Cu muffin tin. Note that the DOS in the K MT has been normalized to $r_{Cu}/r_K$ to be comparable with that in the Cu volume. From these plots it is evident that the SR intensity, evaluated in the K MT, grows in the $\overline{\mathrm{M}}$ and $\overline{\mathrm{K}}$ points. This behaviour, already observed for Cs and Na overlayers, reflects an higher localization of this state at the edges of the surface Brillouin zone. This aspect suggests that the K electronic structure interacts strongly with the states at $\overline{\Gamma}$. Indeed, due to the stronger overlap, the wave-function at $\overline{\Gamma}$ is spread both on the surface Cu layers and on the K overlayer. The surface planar average of the charge density at $\overline{\Gamma}$ and $\overline{\mathrm{M}}$, which is reported in the lower left panel of Fig. 6.8, confirms this behaviour. The dispersion of the surface resonance shows a parabolic dependence on $\mathbf{k}_{\parallel}$ along high symmetry paths. Fitting the energy

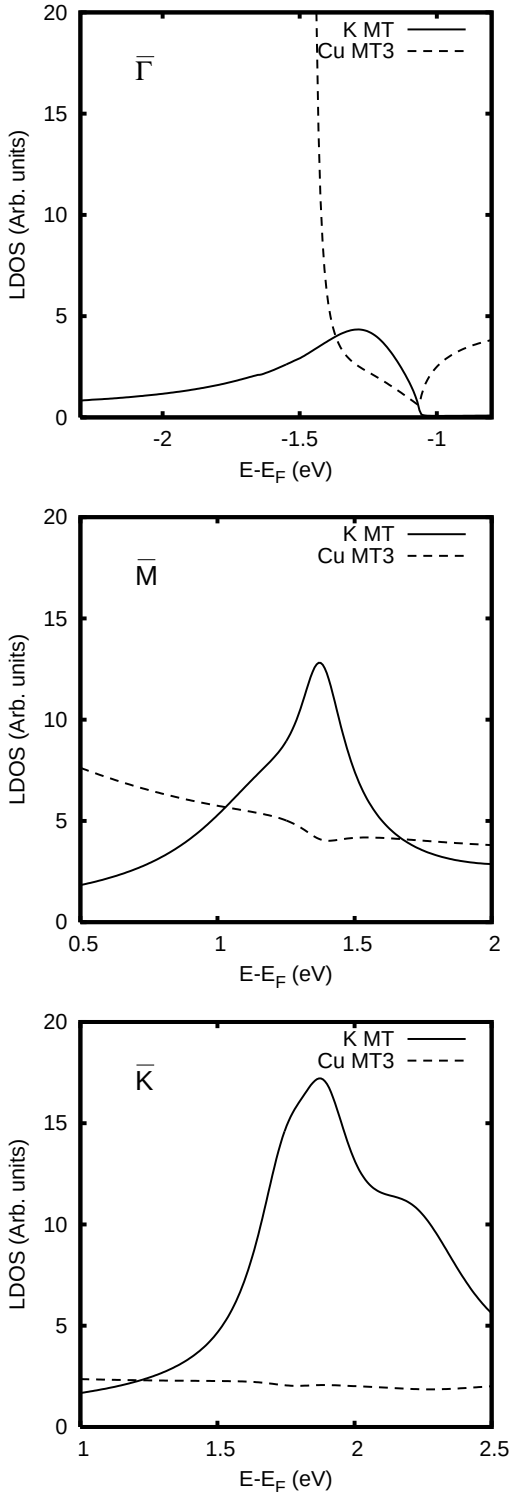


Figure 6.7: Density of states of $p(2 \times 2)$-K/Cu(111) in the energy range of the surface resonance, evaluated in different point of the SBZ and in different volumes, namely the K and Cu muffin tins.

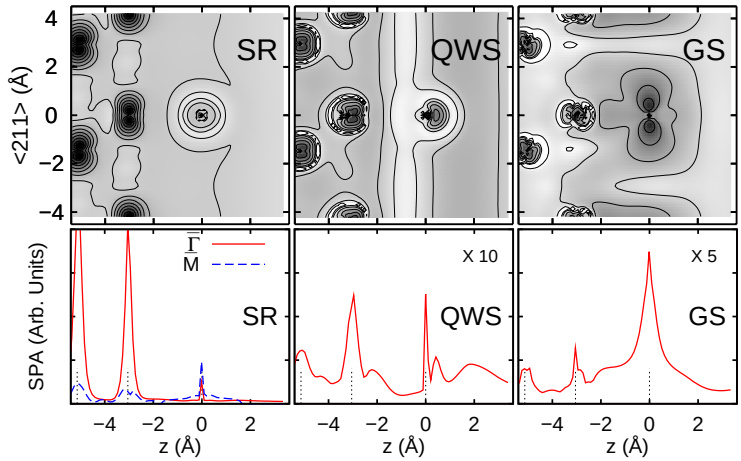


Figure 6.8: Spatial distribution (upper panel) and planar average (lower panel) of the charge density of SR, QWS, GS of $p(2 \times 2)$-K/Cu(111).

position of the maximum the effective mass of 0.53 $m_e$ has been estimated, in quite good agreement with the value of 0.55 $m_e$ reported by Schiller (141).

The other occupied feature observed in the overlayer-vacuum region is the Quantum Well State (QWS) at −0.118 eV from the Fermi level. This state originates from the 2D confinement between two potential barriers: the gap of forbidden states on the substrate side and the vacuum on the other side. The presence of such a state in the alkali-covered surfaces has been investigated both theoretically and experimentally (25; 31; 44) and it is a well known feature of thin and ultra-thin metal films on metal substrates (109). The quantum well state appears in the photoemission spectra from coverages at about half a monolayer and it is connected with the formation of an ordered overlayer structure observed by LEED. It originates from the 4*s* atomic level of K, that lies at higher energies in the limit of zero coverage (see Chapter 4) and shifts down with an increasing amount of alkali metal adsorbed. The theoretical binding energy of the QWS in the $p(2 \times 2)$-K/Cu(111) is slightly greater than that found for the $(3/2 \times 3/2)$ Na/Cu(111), equal to −0.173 eV while for the $p(2 \times 2)$ Cs/Cu(111) this state is unoccupied (+0.05 eV).

For all the alkali-metal overlayers the QWS thus lies within the energy gap of the clean Cu(111) surface. Nevertheless due to the band folding induced by

the surface reconstruction its wave-function overlaps with that of the folded bulk states, resulting in an intrinsic linewidth. The lifetime of the QWS of alkali overlayers on Cu(111) has been object of theoretical studies that evaluated both the elastic and the inelastic contributions (34). The embedding approach allows the estimation of the elastic contribution that is found equal to 2.8 meV in the $\overline{\Gamma}$ point. Recently we have shown that the elastic contribution constitutes only the 5% of the lifetime, which is dominated by the many body inelastic electron-electron scattering (16 meV) and receives a small contribution from the electron-phonon channel (2 meV). Our estimation of the elastic contribution is of the same order of magnitude of that found for Cs overlayer QWS.

The surface charge density distribution relative to QWS is reported in Fig. 6.8 in the upper middle panel. A charge depletion in the region between the K atom and the surface is observed, while it spills out in the vacuum evidencing an outward spatial distribution. The surface planar average confirms this behaviour (lower middle panel of Fig. 6.8) showing a high density outside the surface. This reflects in a high density of states in the K interstitial volume, as can be evinced from Fig. 6.5.

Looking at the dispersion in $\mathbf{k}_{\|}$ the intensity of the QWS is found to decrease moving from $\overline{\Gamma}$ while its linewidth progressively grows, as it will be discussed in next section.

Since the QWS is due to a 2D charge distribution confined at the surface it displays a nearly free electron dispersion in the surface plane. Consequently its effective mass can be determined from a free-particle dispersion law in $\mathbf{k}_{\|}$. The effective mass resulting from the fitting procedure up to $k_F$ is equal to 0.7 $m_e$, in good agreement with the experimental value of 0.8 $m_e$ (141). Passing from Na to K and Cs the QWS progressively moves up in energy and consequently the effective mass becomes closer to the free particle value $m^* = 1\ m_e$. This is because approaching the centre of the energy gap the decay length of the QWS is smaller, so that it is strongly confined in the overlayer acquiring an increasing 2D character.

Concerning the unoccupied part of the DOS it is characterized mainly by the series of image states (IS) that accumulates at the vacuum level and by the gap state (GS) at higher energies. The image states are lower in energy with respect

to the clean surface, because they are pinned to the new vacuum level of the surface. Note that the quite low imaginary part of energy chosen to calculate the DOS allows to resolve the states up to $n = 5$ and in principle the whole series could be obtained by reducing the imaginary part of the energy. However in the literature there is little evidence of the states with $n \geq 3$ due to the limited experimental resolution, so that in the following we will refer only to the first three states of the series. The theoretical binding energies are in good agreement with the experimental ones (50). In the $\overline{\Gamma}$ point the image states lie within an energy gap, also upon the band folding so that they display zero linewidth. The situation changes moving in $\mathbf{k}_{\parallel}$ because they cross the substrate bands and also other overlayer features resulting in an intricate broadening process. Due to their spatial localization far outside the surface, where the planar corrugation of the potential is really small, the image states have an effective mass close to unity.

The last observed electronic feature is a peak at 3.8 eV in the $\overline{\Gamma}$ point. This state was already identified in the overlayer of Cs on Cu(111) as Gap State (GS) (28). In that case it was found to lie within an energy gap at $\overline{\Gamma}$ (at 2.7 eV), resulting in a quite sharp peak. This allowed to conclude that it is not hybridized with the states of vacuum. In the $p(2 \times 2)$-K/Cu(111) the GS is higher in energy, just below the upper edge of the bulk energy gap. Regarding the band structure of the unsupported monolayer reported by Wimmer, this state can be assigned to the $p - d$ band of the overlayer electronic structure. Such a band lies at lower energies for Cs, in agreement with the previously observed difference in the binding energy of the GS. The surface charge density (right panel Fig. 6.8) confirms such interpretation; it shows indeed a $p$-like orbital on the K atom. The charge density accumulates on the K atom, as confirmed also by the surface planar average. These properties of the GS reproduce what already found in the case of Cs, confirming that the two features have the same physical nature. Moving from the $\overline{\Gamma}$ point the GS separates in two branches. One of them disperses downward and joins the surface resonance both in the $\overline{\mathrm{M}}$ and $\overline{\mathrm{K}}$ points so that it can be viewed as a folded band. The other branch disperses upwards for one third of the path in $\mathbf{k}_{\parallel}$ then its dispersion suddenly changes and it shifts down in energy. This change is not properly a strange behaviour typical of this state but it is due to the crossing with an higher energy band.

Table 6.1: Key features of the surface states of $p(2 \times 2)$-K/Cu(111) (in brackets the experimental values (50; 141)). Binding energy and elastic linewidth are relative to the $\overline{\Gamma}$ point. The image states are given with respect to the vacuum level.

| State | Energy (eV) | $k_{\mathrm{F}}$ (Å$^{-1}$) | m$^*$ ($m_e$) | $\Gamma_{el}$ (meV) |
|---|---|---|---|---|
| SR | $-1.28$ (1.03) | 0.43 (0.36) | 0.53 (0.55) | 250 |
| QWS | $-0.118$ ($-0.100$) | 0.148 (0.15) | 0.707 (0.81) | 2.8 |
| GS | 3.8 | | | $\sim$0 |
| $n = 1$ | $-0.626$ ($-0.64 \pm 0.03$) | | 0.92 | 0 |
| $n = 2$ | $-0.208$ ($-0.19$) | | 0.95 | 0 |
| $n = 3$ | $-0.090$ ($-0.05$)] | | 0.95 | 0 |

It is interesting to note that when the second branch of the GS encounters the $n = 1$ image state along the $\overline{\Gamma\mathrm{K}}$ path, it displays an anti-crossing behaviour due to symmetry reasons.

In Tab. 6.1 a summary of the relevant properties of the analyzed features are reported, in comparison with the experimental results available.

### 6.3.2 Elastic linewidth along a high symmetry path in the surface Brillouin zone

It has been already shown that the accurate description of the continuum of the bulk states allows the determination of the elastic linewidth of the electronic surface features. In the $p(2 \times 2)$-K/Cu(111) the folding of the copper bands and their mutual superposition in the Brillouin zone, induce complex changes of the elastic linewidth along high symmetry paths in the SBZ. Indeed the overlayer features can hybridize differently with the substrate states at the centre or at the edge of the SBZ. In addition their linewidth depends on the symmetry of the states involved in the hybridization. In the upper panel of Fig. 6.9 is reported the dispersion of the overlayer resonances along $\overline{\Gamma\mathrm{K}}$, superimposed on the surface projected bulk band structure resulting from the folding in the $p(2 \times 2)$ SBZ. The dots correspond to the maxima of the observed overlayer states. Note that there are three paths of the $(1 \times 1)$ SBZ that are folded in the $\overline{\Gamma\mathrm{K}}$ of the $p(2 \times 2)$ (see

Fig. 6.3):

$$\overline{\Gamma K} = \overline{\Gamma}'\overline{K}'/2 + \overline{M}'\overline{K}' + \overline{M}'\overline{K}'/2 \tag{6.1}$$

where $\overline{K}'/2$ is the intermediate point of the $\overline{\Gamma}'\overline{K}'$ path in the $(1 \times 1)$ SBZ that coincides with the $\overline{K}$ point. In the bottom panels the elastic linewidth of the overlayer features is reported as a function of $\mathbf{k}_{\|}$. This has been obtained fitting these states with a Lorentzian function plus an additive constant that accounts for the background of the substrate states. The variation of the linewidth as a function of $\mathbf{k}_{\|}$ is not trivial and can be explained quite successfully by the different interaction of the overlayer states with the bulk bands they encounter along the path. Let us analyze the situation with more detail. Starting from the occupied states, the SR displays an initial linewidth of 0.21 eV at $\overline{\Gamma}$ which remains nearly constant since the state crosses the bands proper of the $\overline{M}'\overline{K}'/2$ path at $\mathbf{k}_{\|}$ equal to 0.1 $\text{Å}^{-1}$. This behaviour suggests that it interacts strongly with the states near the $\overline{M}'$ point, more than with the states at $\overline{\Gamma}'$. The linewidth thus starts to grow, then it reaches a maximum and after decreases. Differently the QWS displays a really small intrinsic linewidth at the $\overline{\Gamma}$ point due to a little hybridization with the states near the $\overline{M}'$ point. The linewidth of this state starts to increase when it enters in the bulk band relative to the $\overline{\Gamma}'$ $\overline{K}'/2$ path. This behaviour demonstrates that the QWS hybridizes poorly with the folded bands while it is quenched by the bulk states in the $\overline{\Gamma}'\overline{K}'/2$ path. The series of image states has zero linewidth at $\overline{\Gamma}$ lying within the resulting energy gap. The major changes in their linewidth are induced by the crossing with the branches of the gap state while the hybridization with the bulk continuum is little. This is an effect of the spatial localization of these states far outside the surface. As a consequence the overlap with bulk states is lower, while the wave-function of the GS which is localized in the overlayer has a larger probability of hybridization. Finally both the branches of the GS start at $\overline{\Gamma}$ with zero linewidth, then they broaden due to the crossing with the bulk band that they encounter in the dispersion.

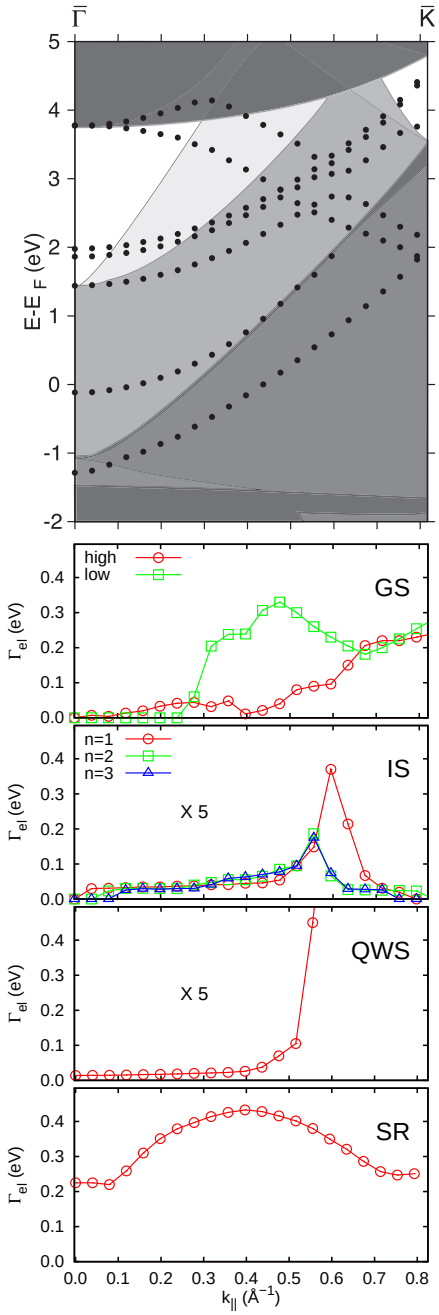


Figure 6.9: Upper panel: Dispersion of the K induced states and folded bands of Cu(111). Lower panels: Linewidth of the overlayer states as a function of $\mathbf{k}_{\|}$.

# Chapter 7

# $c(2 \times 2)$-Bi/Cu(100)

Phase transitions in reduced dimensional materials are sometimes a direct consequence of electronic instability against lattice distortion due to dimensionality reduction. The interplay between electronic properties and surface morphology is then a key issue in the characterization of quasi-2D systems which display high electron-phonon coupling, as for example ultra-thin crystal films of *sp*-block metals on fcc(001) surfaces (8).

Bismuth is an example of an *sp*-block metal with strong electron-phonon coupling and large spin-orbit splitting in the surface bands (68). In addition an enhancement of the density of states at the Fermi level passing from bulk to the surface (71) has been evidenced for this system.

It was observed experimentally that the adsorption of a single Bi layer on Cu(100) gives rise to a large variety of structural phases varying the coverage (40; 107; 108; 163). The analogies with the case of In/Cu(100) (112) suggest a possible explanation of these phase transitions on the basis of the coupling of the conduction electrons with the phonon modes of the system leading to the formation of a charge density wave (CDW). This hypothesis is not yet confirmed and requires an accurate understanding of the electronic properties of the thin film adsorbed. In particular the density of states at the Fermi level plays a fundamental role in such a process, being the *nesting* of the Fermi surface a necessary condition for such kind of Peierls transition (131).

An accurate analysis of the spectral properties of the different phases observed has been performed recently through an Angle Resolved Photoemission Spec-

troscopy (ARPES) experiment (58). It shows the evolution of the Bi-induced states upon the formation of strain dislocations in the Bi surface plane, that separate $c(2 \times 2)$ domains.

In this chapter the *ab initio* theoretical results relative to the ordered $c(2 \times 2)$ reconstruction are presented. This structural phase occurs at 0.5 ML and characterizes the local morphology of the bi-domain superstructures at higher coverages. Thus a deep insight into the electronic properties of such a phase can help in understanding the influence of the periodic array of dislocations on the electronic structure, as observed experimentally. In addition it could give some evidence of the interplay of electronic and structural properties in the sequence of phase transitions observed for this system.

## 7.1 Surface reconstructions and theoretical modeling

A single layer of bismuth deposited on the Cu(100) surface forms long range ordered structural phases at various Bi density. The LEED experiments show that the initial deposition of Bi on Cu(001) surface corresponds to the formation of a Bi-Cu alloy (108) concomitant with a charge transfer that induces a work function reduction. At around 0.5 ML of coverage an ordered $c(2 \times 2)$ phase is observed with the Bi atoms in hollow positions (58). This structural phase coincides with the complete de-alloying of the overlayer. Increasing the Bi coverage line dislocations appear that determine the transition to a $(9\sqrt{2} \times \sqrt{2})$R45° reconstruction accompanied by an abrupt change in the work function that reduces further. For a coverage equal to 0.6 ML a strain induced bi-dimensional array of dislocations is formed giving rise to a $p(10 \times 10)$ reconstruction (107).

The high symmetry $c(2 \times 2)$ phase thus characterizes the local morphology since 0.5 ML of coverage up to the completion of the full monolayer. The *ab initio* embedding calculation has been performed considering a surface cell which is $(\sqrt{2} \times \sqrt{2})$R45° that of the clean Cu(100) surface. The cell contains one Bi atom in hollow position. The Bi-Cu vertical distance has been set equal to 2.07 Å according to Refs. (107; 108). In addition a surface relaxation of the outermost

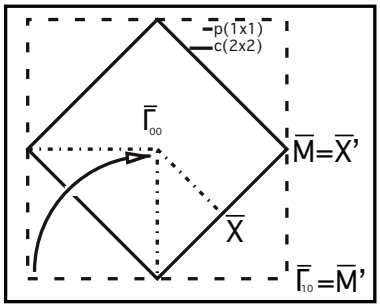


Figure 7.1: Surface Brillouin zone of $c(2\times2)$-Bi/Cu(100) (solid line) and Cu(100) (dashed line).

Cu layer as been included, in terms of a 2.3 % expansion of the interlayer spacing, as determined by experiment. The embedded region includes two Cu substrate layers on the bulk side and extends for about 9 Å in vacuum. The calculation has been performed using 18.1 Rydberg as the cutoff for the basis set and a spherical expansion up to $l_{max} = 8$ in the muffin tins. The DOS are calculated introducing a small imaginary part of the energy, equal to 5 meV. The surface Brillouin zone is sampled with a $(10 \times 10)$ mesh in reciprocal space that reduces to 21 independent $\mathbf{k}_{||}$ points. The surface Brillouin zone is reported in Fig. 7.1 in comparison with that of Cu(100). As a consequence of the surface reconstruction the pristine Brillouin zone is folded in the smaller one. Note that primed letters refer to the high symmetry points in the $(1 \times 1)$ SBZ.

A PBE-GGA approximation for the exchange and correlations potential has been used.

Please note that currently the embedding code does not contains the spin-orbit interaction, so this is neglected in the results presented in the following.

## 7.2 Bi-induced features in the $k_{||}$ resolved DOS

The starting point in the analysis of the electronic properties of the system can be the $\mathbf{k}_{||}$ resolved DOS in different spatial volumes. In Fig. 7.2 the DOS of $c(2\times2)$-Bi/Cu(100) in the $\overline{\Gamma}$ point is reported in the upper panel for two different volumes:

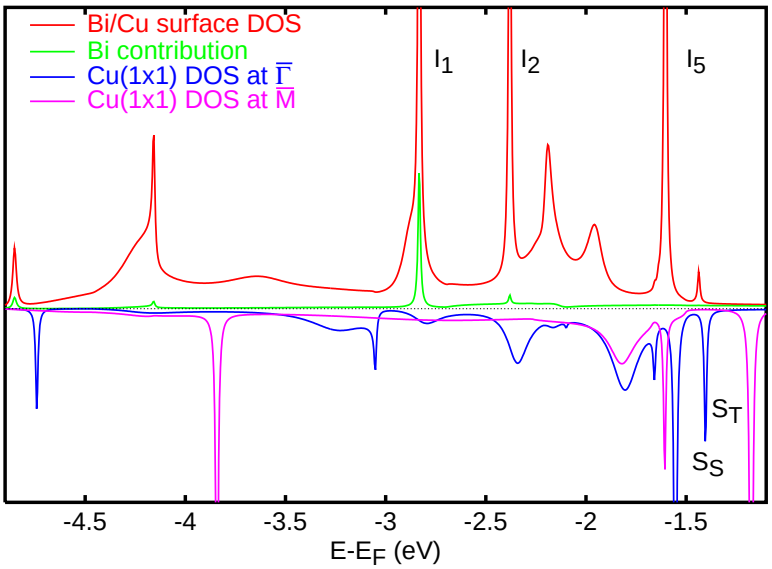


Figure 7.2: Density of states of $c(2 \times 2)$-Bi/Cu(100) at the $\overline{\Gamma}$ point (upper panel), evaluated in two different volumes, in comparison with the surface DOS of Cu(100) in the equivalent points of the $(1 \times 1)$ SBZ (reversed in the lower panel).

the surface region (Bi plus sub-surface Cu MT) and the Bi layer alone in order to identify the states localized in the overlayer. The DOS is also compared with that obtained for the clean Cu(100) surface in the equivalent points of the SBZ. This DOS is reported reversed in the lower panel of Fig. 7.2. Note that, due to the folding, both the $\overline{\Gamma}$' and $\overline{\mathrm{M}}$' points of the $(1 \times 1)$ Brillouin zone contribute to the $\overline{\Gamma}$ point of the $c(2 \times 2)$.

The first notable effect of the Bi deposition is the disappearance of the Tamm state ($S_T$) of Cu(100), localized within a surface projected energy gap in the $\overline{\mathrm{M}}$' point of the $(1 \times 1)$ SBZ. Differently the Shockley state ($S_S$), which is in the $\overline{\Gamma}$' point of Cu(100), is slightly shifted and reduced in amplitude. The $d$ band of copper, in the energy range between $-1.5$ and $-3.5$ eV, exhibits a reorganization in the spectral weight of the electronic states. In addition a general shift of the copper surface states toward lower energies can be noted. This behaviour can be observed for example for the discrete state at $-4.73$ eV in the $\overline{\Gamma}$' point that shifts toward the lower edge of the small gap in which it lies. The size of the shift

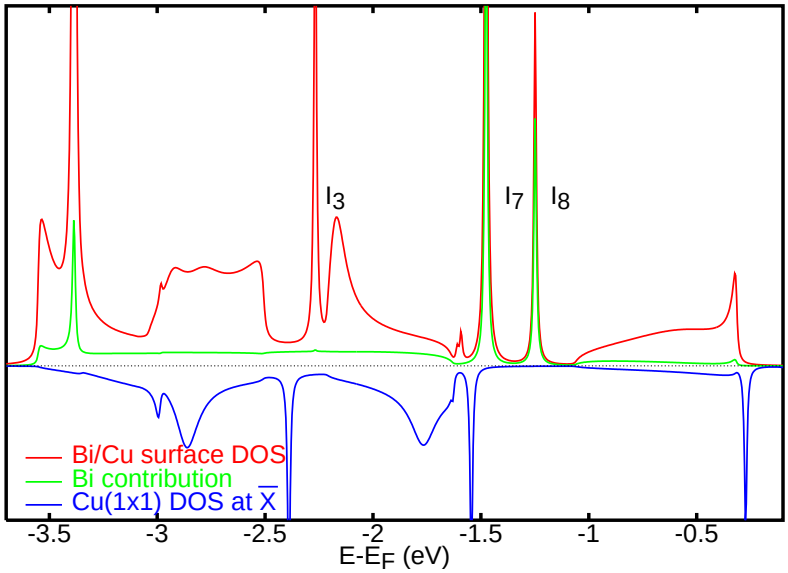


Figure 7.3: Density of states of $c(2\times2)$-Bi/Cu(100) at the $\overline{\text{M}}$ point (upper panel), evaluated in two different volumes, in comparison with the DOS of Cu(100) in the equivalent point of the $(1 \times 1)$ SBZ (reversed in the lower panel).

is even larger for the surface resonance at $-3.85$ in $\overline{\text{M}}$', whose energy is reduced of about 0.5 eV. Upon adsorption of Bi new sharp features appear in the DOS that have been identified by $I_i$. Among them only the $I_1$ is localized in the Bi layer. The other $I_i$ features can not be immediately identified as overlayer states and could be due to a modification of the spectral properties of the underlying Cu(100) substrate resulting in an energy shift of the surface states and in the variation of the spectral weight of the electronic states. The DOS in the $\overline{\text{M}}$ point, reported in Fig. 7.3 in comparison with the correspondent point of the $(1 \times 1)$ surface, exhibits more significant features localized on Bi. These ones, labeled by $I_8$ and $I_7$ lie in a surface energy gap of Cu(100) resulting in very narrow peaks. The $I_7$ peak is more precisely due to a doublet of states that are degenerate at $\overline{\Gamma}$.

Also in this case there is a reorganization of the $d$ band of copper and an energy shift of its surface states, namely the discrete state at $-1.5$ eV and the surface resonance at $-2.4$ eV. In particular the last one shifts toward higher energies leading to a very narrow peak labeled by $I_3$.

The spectral features just analyzed are in very good agreement with that

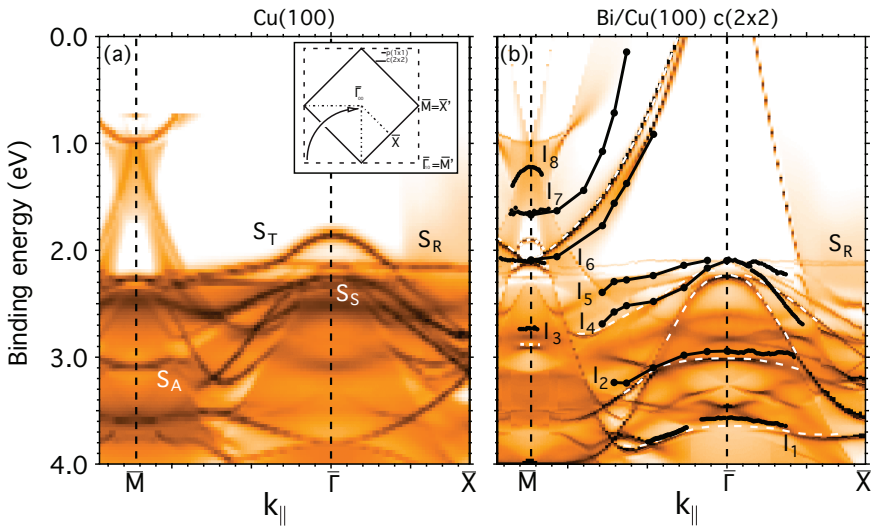


Figure 7.4: Surface band structure of $c(2 \times 2)$-Bi/Cu(100) in comparison with the Cu(100) one (left panel) and with the experimental data (dotted-lines). The theoretical band structure has been shifted of 0.73 eV to allow a better comparison with experiments. Theoretical surface states are evidenced by white dashed lines.

evidenced by ARPES measurements. Almost all the theoretically predicted states have been observed for the $c(2 \times 2)$ phase. The ARPES investigation, performed as a function of coverage, shows that the Bi-induced states are influenced by the formation of the surface strain dislocations. In particular the binding energy of $I_1, I_2, I_4$ reduces increasing the coverage of Bi. This energy shift seems to be due to the effect of the domain wall potential confinement on the electronic states. Differently $I_6, I_7, I_8$ are completely quenched passing from the $c(2 \times 2)$ to the $(9\sqrt{2} \times \sqrt{2})$R45° phase. The $I_3$ state is unshifted in all the experimental coverage-dependent measurements confirming that it is proper of the copper band structure.

The comparison between theoretical and experimental results has been performed in Ref. (58) by applying an overall shift to the computed electronic band structure. This shift can be justified through the inaccuracy in the Kohn-Sham estimation of the binding energy, which is commonly known, and often resolved by shifting the theoretical data in order to compare them with the experimental ones. A more correct operating procedure should account for a different shift for

different electronic states, because the many body effects are not the same for all the spectral features.

There is also agreement between theory and experiment for the surface band dispersion in $\mathbf{k}_{\parallel}$. In Fig. 7.4 the theoretical surface band structure along high symmetry paths in the SBZ is depicted both for Cu(100) and $c(2\times2)$-Bi/Cu(100). Theoretical data have been shifted by 0.73 eV, as explained above. This energy shift is the same as reported for the clean Cu(100) surface in Ref. (9). The experimental $I_i$ states are superimposed as black lines while the computed surface states are evidenced by white dashed lines.

Around the $\overline{\Gamma}$ point the agreement is quite good. The $I_5$ and $I_6$ states are characterized by a downward dispersion moving around the centre of the SBZ. The same holds also for $I_2$ and $I_1$ but with a smaller curvature. While in the $\overline{\Gamma}$ point the superposition between theoretical and experimental results is almost perfect with the energy shift, in $\overline{\mathrm{M}}$ the applied energy translation is responsible for a theoretical-experimental discrepancy in the $I_8$ binding energies that would coincide in absence of the fictitious shift. Note that the $I_7$ peak is split in two states moving away from $\overline{\Gamma}$. The degeneracy of these two states at $\overline{\Gamma}$ occurs only in the theoretical results, while the experimental ones show two different states, as an effect of the spin orbit splitting.

Among the theoretical features that have not counterparts in experimental measurements, the free-electron like state along $\overline{\Gamma\mathrm{X}}$ is worthy to note. This state, not observed in ARPES measurements could be responsible for the formation of a CDW in the system, as will be discussed in next section.

Finally comparing this dispersion with that of Cu(100) the changes already evidenced previously can be observed, namely the disappearance of the Tamm state and the general shift of the surface states.

## 7.3 Fermi surface and Charge Density Wave

The last literature regarding chemical modified surfaces revealed that the physical properties of these systems are strictly related to their low dimensionality (112; 148). In particular it was shown that the phase transitions observed for these adsorbed systems could originate by the instability of the low dimensional

electron system induced by the electron-phonon coupling (139). This instability is essentially due to the divergence in the response of an electron gas to an external perturbation with modulation $q = 2k_F$.

The linear response theory provides evidence of such instability as a singularity in the Lindhard response function, showing that it is more pronounced in low dimensional systems (137).

In practice the phonons interact with the electron excitations that connect states at the Fermi level (one occupied and one unoccupied) separated by a wave vector equal to $2k_F$. As a consequence, the divergence in the Lindhard response function can be related to the topology of the Fermi surface, i.e. to the number of states on the Fermi surface that can be spanned by parallel vectors with modulus $2k_F$. The greater is the number of such nesting vectors connecting parallel branches of the Fermi surface, the greater is the divergent behaviour. For instance, the Fermi surface of materials with one dimensional character consists in two parallel planes with distance $2k_F$. This situation is referred as *perfect nesting* since the number of nesting vectors is maximized.

Due to the concerted operation of the electron-phonon coupling and the Fermi surface nesting, the system undergoes a periodic charge redistribution with wavevector $q$. At the same time the phonon mode at $2k_F$ is frozen in, i.e. the static displacement of the ion cores takes place from the equilibrium position. Such periodic lattice distortion is commonly referred as Peierls transition (131) associated to a Charge Density Wave (CDW). The formation of a CDW results in an energy gain due to the opening of an energy gap at the Fermi level.

Although in more than one dimension the number of *nesting* vectors is reduced, due to the different topology of the Fermi surface, also in realistic systems the Peierls instability can be the driving mechanism for the surface reconstruction.

The occurrence of a CDW was invoked to explain for example the surface reconstructions observed for H on W (164), in $NbSe_2$ (159) and in many *sp*-block metals on Cu(100) (see Tab. 1 in Ref. (8) and references therein).

In particular In/Cu(100) exhibits many similarities to the Bi/Cu(100) case, being characterized by an analogous transition from a $c(2 \times 2)$ phase to the $(9\sqrt{2} \times \sqrt{2})$R45° one. Nakagawa (112) demonstrated that the phase transition

can be explained invoking a *generalized nesting* condition for the Fermi surface: $Nq = 2k_F$, where N is an integer. In that case parallel branches of the Fermi surfaces were connected by a vector of modulus $2k_F$ equal to three times the shortest modulation vectors $q$ that determines the surface reconstruction.

In order to verify if the phase transitions observed for Bi/Cu(100) can be related to the formation of a CDW, the Fermi surface proper of the $c(2 \times 2)$ phase has been computed and the nesting condition has been checked. The Fermi surface has been obtained considering the LDOS at the Fermi level along a series of parallel paths that span the $\overline{\Gamma\mathrm{MX}}$ irreducible zone of the SBZ. Along these paths the $k_F$ has been identified and reported in a 2D $(k_x, k_y)$ plot. Through symmetry operations the Fermi surface on the whole Brillouin zone has been reconstructed and it is reported in Fig. 7.6 in an extended zone scheme. The surface Brillouin zone of $c(2 \times 2)$-Bi/Cu(100) corresponds to the blue (solid) line in the picture.

Let us analyze the origin of the branches observed in the Fermi surface. The branches along the $\overline{\Gamma\mathrm{M}}$ direction originate from the theoretical $I_6$ and $I_7$ parabolic states while that along $\overline{\Gamma\mathrm{X}}$ is related to the free-electron band observed in that direction. This feature, named $I_9$ in the following, has been characterized only from a theoretical point of view while there is no evidence of such a state in the experimental results. It is related to a surface state, induced by Bi adsorption, that lies close to the substrate bulk band (see Fig. 7.5 that shows the DOS at the $k_F$ relative to this state).

The shape of the Fermi surface and the physical nature of the states that contribute to this one suggest that the observed branches originate from the folding in the $c(2\times2)$ SBZ of a nearly free-electron like resonance (Red (solid) line circumference in the picture). This resonance would generate in an extended zone scheme a circular shape Fermi surface which is typical of a perfect bi-dimensional system (see Fig. 7.6). This could explain also the absence of the $I_9$ state in the experimental measurements. The photoemission spectra are indeed recorded in an extended zone approach and they have to be folded in order to be compared with the theoretical ones. Nevertheless the folded experimental surface band structure could not coincide with the theoretical dispersion, due to the effect of the photoemission matrix elements. Indeed they could generate an enhancement

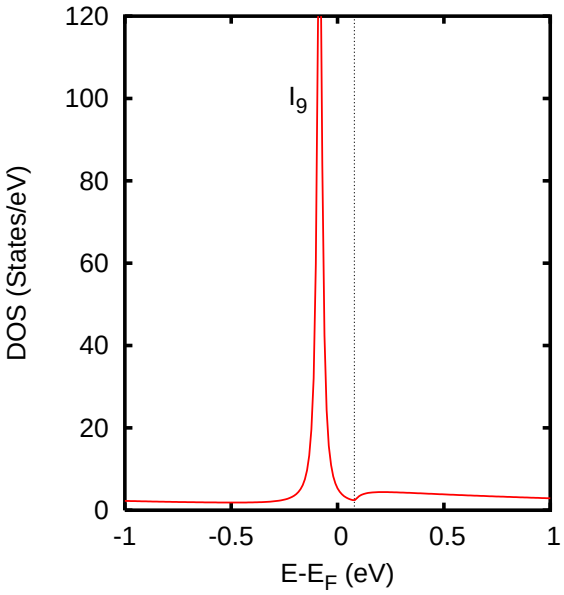


Figure 7.5: The $I_9$ state in the DOS of $c(2 \times 2)$-Bi/Cu(100) at the $k_F$ relative to this surface feature. Vertical dashed line evidences the bulk band edge.

of the spectral weight of the states in the $c(2 \times 2)$ SBZ and a depression of these ones in the adjacent SBZ. This could be exactly what happens for $I_9$ that, in an extended zone scheme, lies in the second SBZ.

We will now focus on the criterion for the occurrence of a CDW, i.e. the nesting of the Fermi surface. In order to verify if there are nesting vectors that would justify a CDW, let us consider the period of the modulation induced by the surface reconstruction. In the $c(9\sqrt{2} \times \sqrt{2})$R45° the two orthogonal modulation vectors are: $q_1 = 2\pi/(9\sqrt{a})$ and $q_2 = 2\pi/\sqrt{a}$ ($a$ is the lattice parameter of Cu(111)) that are oriented along the [110] and the [$\bar{1}$10] direction respectively. In other words the modulation vectors are the sides of the SBZ of the reconstruction. Searching for a nesting vector that can be related to such modulation, it has been verified that a generalized nesting condition is almost verified: $3q_1 \approx 2k_F$ along the $\overline{\Gamma X}$ direction, by a vector that connects the parallel branches generated by the $I_9$ state. In Fig. 7.7, left panel, such a nesting vector is reported (green arrow) together with the $c(9\sqrt{2} \times \sqrt{2})$R45° SBZ (green solid line). The not perfect nesting could be ascribed to the absence in the theoretical calculation of the spin

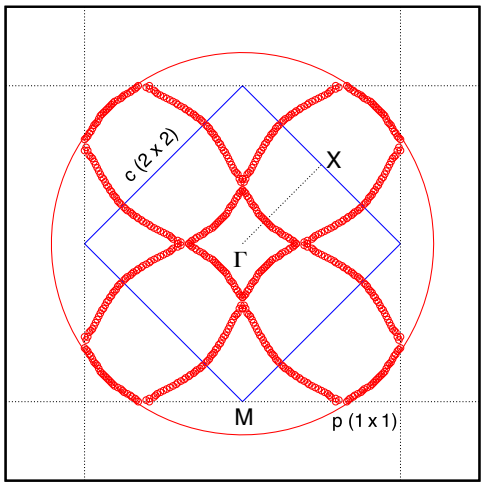


Figure 7.6: Fermi surface (empty circles) of $c(2 \times 2)$-Bi/Cu(100) in an extended zone scheme. The blue (solid) line corresponds to the $c(2 \times 2)$ SBZ. Dashed lines indicate the $(1 \times 1)$ SBZ. The red (solid) circumference is the free electron like resonance that generates the observed Fermi surface.

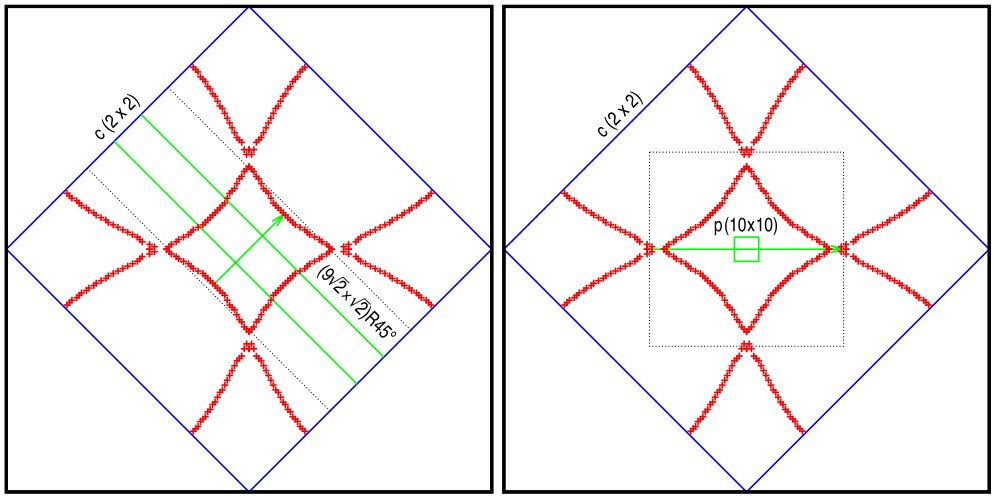


Figure 7.7: *Nesting condition* for the Fermi surface, relative to the $c(9\sqrt{2} \times \sqrt{2})$R45° (left) and $p(10 \times 10)$ (right) reconstructions. The green lines and arrows indicate respectively the SBZ of the reconstructions and the *nesting* vector.

orbit term. Including such a correction the surface states are expected to split in doublet and one of the two resulting states might satisfy perfectly the generalized nesting condition.

For what concerns the $p(10 \times 10)$ reconstruction the modulation vectors are $q_1 = q_2 = 2\pi/(10a)$ along the [100] and [010] direction. In this case a generalized nesting condition $8q_{1,2} = 2k_F$ is exactly satisfied, involving the branches generated by the $I_7$ state (see green arrow in Fig. 7.7, right panel).

Concluding this analysis we can suppose that, in analogy with the In/Cu(100), the driven mechanism for the surface reconstructions observed for Bi/Cu(100) could be a CDW transition.

# Chapter 8

# $p(1 \times 1)$-O/Fe(100)

The aim of this chapter is to show how the *ab initio* electronic properties calculated in the embedding approach can be used as a support to the experimental measurements. In particular a simulation of STM and STS images will be shown, recently employed in a joint experimental-theoretical study. The system chosen for such kind of analysis is a thin oxygen film (1 ML) on Fe(100) which is characterized by the formation of an ordered $p(1 \times 1)$ phase (104). The adsorption of oxygen on iron surfaces has been the object of a large number of both theoretical and experimental works. The scientific relevance of such a system is motivated by the interest in understanding the physical basis of processes like corrosion, passivation, oxidation that characterize the iron surfaces and that have important consequences in technological applications (145). The magnetic character of the substrate leads to notable magnetic effects when ultra-thin films of oxygen are grown on the iron surface. For example it was demonstrated that in such systems the surface magnetization is enhanced, while the oxygen atoms acquire a small induced magnetic moment (30; 33). In addition the adsorption of oxygen gives an example of ferromagnetic coupling between the adsorbates and the surface. These properties, together with the low dimensionality of the system, are suitable for application in the field of nano-technology and in the industry of magnetic recording (156). Ultra-thin oxygen films on Fe (100) have been extensively studied through a large number of experimental techniques. Among them STM and STS techniques proved extremely useful in order to perform a nanometer-scale investigation of both the surface atomic structure and the spatial distribution of

the electronic states at the Fermi level. In addition the recent introduction of the spin resolution in these techniques opens the way to a magnetic characterization of the surface. An accurate analysis of the experimental results can exploits the *ab initio* simulation of the tunneling current.

Although an appropriate description of the tunneling current takes into account the electronic structure of both the sample and the tip, the Tersoff-Hamman approach allows to connect this quantity directly to the DOS of the sample at the Fermi level, considering a constant density of states for the tip. Before showing the STS and STM simulations a brief analysis of the electronic properties of the system will be performed, this being a fundamental preliminary step for the complete understanding of the simulations.

## 8.1 *Ab initio* electronic structure calculation

The *ab initio* calculation has been performed including in the embedded region four atomic layers of Fe, the oxygen overlayer and 11 Å of vacuum. It has been verified that in such a magnetic system four substrate layers in the embedded region are necessary to guarantee the correct matching with the unperturbed bulk, in term of potential and local magnetic moment. The surface relaxation has been taken as reported by Ref. (30). For the parameters of the calculation, the cutoff for the FLAPW basis set has been chosen equal to 11.6 Ry, while the maximum angular momentum for the expansion in the *muffin tins* was fixed equal to 9. The muffin tins radii are equal to 1.2 Å and 0.85 Å for O and Fe, respectively. The surface Brillouin zone has been sampled with a $(18 \times 18)$ regular mesh which reduces to 55 independent $\mathbf{k}_{\|}$ points. Note that with respect to the K/Cu(111) overlayer, the Brillouin zone is larger, so that more $\mathbf{k}_{\|}$ points in the mesh are necessary. The DOS have been calculated introducing an imaginary part of energy in the calculation, equal to 5 meV.

Finally the PBE-GGA approximation has been used for the exchange-correlation term. It is indeed well known that LDA is not appropriate for magnetic systems.

In order to analyze briefly the electronic properties of the system, the surface band structure evaluated in different volumes has been reported in Fig. 8.1. The graphical representation adopted here reproduces the DOS at every $\mathbf{k}_{\|}$ point

using a colorimetric scale. In particular, bright yellow region corresponds to higher values of the DOS while dark red-blue colours mean a small number of states. Note that in this representation the energy gaps (zero states) should be black. Nevertheless the black colour is fixed at the lower limit of the scale used for the DOS values. Consequently black areas may not correspond to energy gaps but also to very low-density areas. In the plots of Fig. 8.1 a logarithmic scale for the DOS has been used, that shows both small and large values of the density of states. In order to appreciate the difference between surface states and bulk states the surface band structure has been evaluated in different volumes: in the upper panel the LDOS in the inner "bulk" Fe muffin tins is reported while the second and third panel are relative to the sub-surface Fe and O muffin tins, respectively. Finally the last panel shows the band structure in the volume outside the surface. Note that in this region the DOS is smaller than within the surface, so that a re-scaling of the data is necessary in order to appreciate the colour differences at different energies and $\mathbf{k}_{\|}$. Let us now analyze the main properties of the surface band structure referring to the $\overline{\Gamma}$ point. First of all, due to the magnetic character of the system, the majority component (left panel) differs by the minority one (right panel). The former is characterized by the $d$ band of iron between $-3$ eV and $-1$ eV. In the minority component the $d$ band extends between $-0.5$ eV and 2 eV and is partially unoccupied. This imbalance between the two components produces a magnetic moment equal to 2.23 $\mu_B$ in the bulk and also higher at the surface where the energy separation between the two spin components results larger. In addition to the $d$ band the continuum of $s$ states can be identified. This corresponds to regions marked by the red colour, i.e. characterized by lower values of the DOS, the $s$ states being delocalized. In addition to the bulk states there are also surface features in the surface band structure. These ones becomes more evident considering the outermost muffin tins, due to their spatial localization in the surface region. Considering the sub-surface Fe atom and the O muffin tin the spectral weight of some features progressively grows while other ones become less intense. These bright states correspond to surface states that can be a property of the iron surface or induced by the adsorption of oxygen. In particular at $\overline{\Gamma}$ majority-spin surface states can be identified at $-3$, $-1.6$ and $-0.8$ eV. The minority-spin surface features are found at higher energies, namely

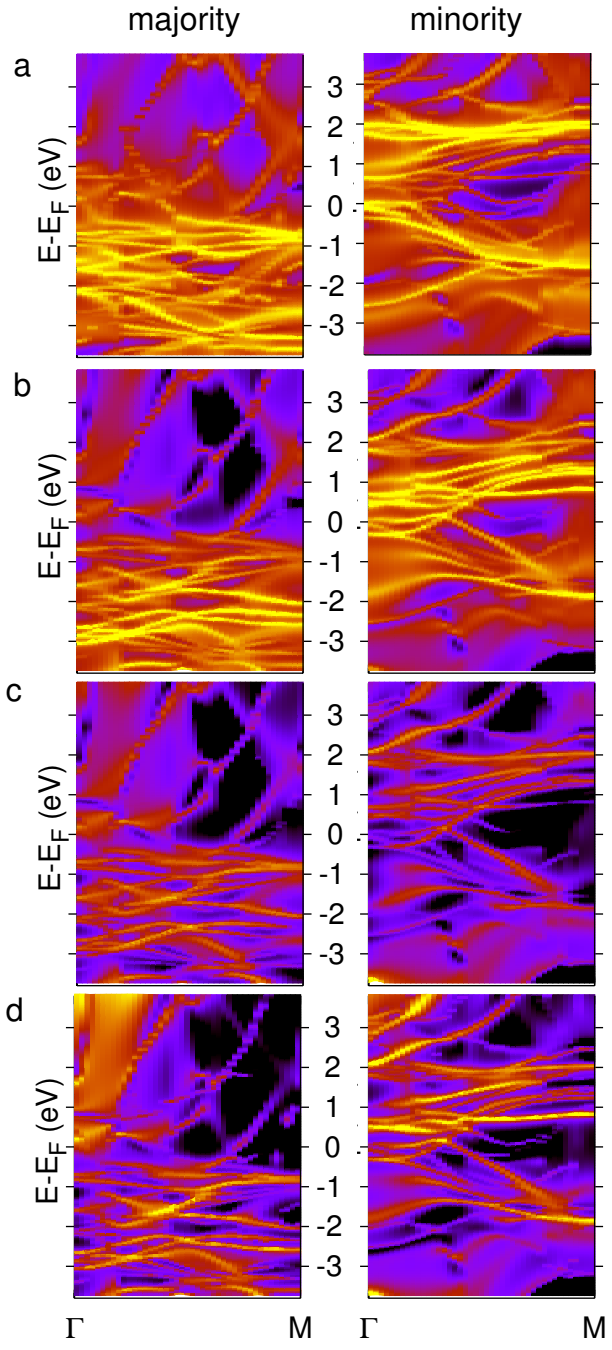


Figure 8.1: Surface band structure of $p(1 \times 1)$-O/Fe(100) evaluated in different volumes. a) inner Fe atom; b) sub-surface Fe atom; c) O atom; d) vacuum region outside the surface.

at $-0.35$ eV, in a 1 eV range above the Fermi level and at 1.7 and 2.1 eV. The surface band structure in the vacuum shows that these surface features extend spatially also outside the surface where they progressively decay. The advantage of such colorimetric representation of the LDOS is that in addition to show the relative intensity of the electronic states it allows to appreciate also their linewidth which is a peculiarity of the embedding method. In fact, differently from supercell calculations that gives a surface band structure composed by a series of discrete states, the *ab initio* calculation presented here allows to distinguish the sharp features (yellow narrow line) from the resonances (for example the broad line at $-2$ eV in the minority component) and from the continuous of bulk states (violet background).

## 8.2 STS and STM simulation

Scanning Tunneling Microscopy (STM) and Spectroscopy (STS) are two powerful experimental techniques based on the concept of quantum tunneling. They measure the tunneling current that flows between the sampled surface and a conducting tip, upon the application of a bias voltage. The tunneling current can be written as (155):

$$I(V) = A \int_0^{eV} T(E, V, z)\rho_S(E)\rho_T(E - eV)dE \tag{8.1}$$

where $\rho_S$ and $\rho_T$ are the sample and tip LDOS, $V$ is the applied bias, $T$ is the barrier transmission coefficient and A is a proportionality dimensional coefficient.

The STS approach consists in a spectroscopic application of scanning tunneling microscopy. It measures the $I - V$ spectrum or the differential conductivity $dI(V)/dV$ with the purpose to extract the density of states of the system. This is contained in a non obvious way in STS data, and a proper understanding of the overall features of the system (sample+tip) is mandatory in order to obtain quantitative information. Several approaches have been proposed in the literature to tackle this problem. A common feature of these methods is that they are mostly based on a one-dimensional (1D) Wentzel-Kramers-Brillouin (WKB) description

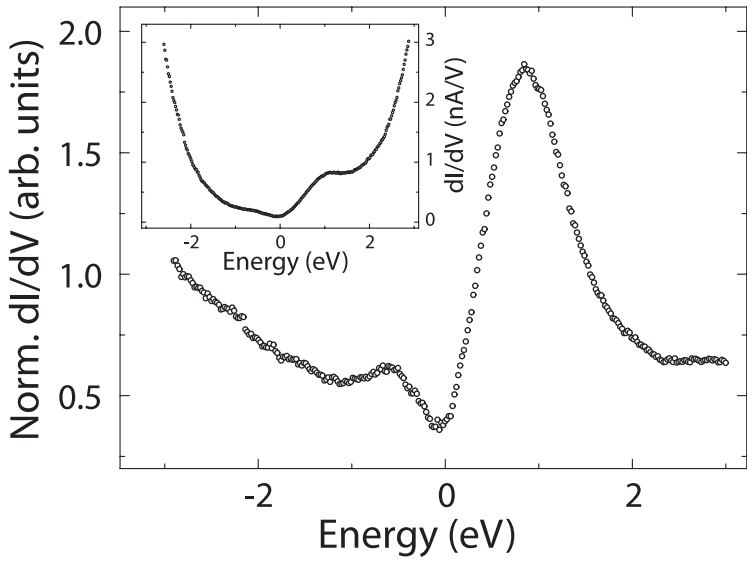


Figure 8.2: Experimental STS image of $p(1 \times 1)$-O/Fe(100). For details about the set-point of the measure see Ref. (43)

of the tunneling current. Within such a formalism the following approximated expression holds (129):

$$\rho_T(0)\rho_S(eV) \propto \frac{dI/dV}{T_S} \tag{8.2}$$

where $T_S$ is a symmetric combination of the barrier transmission coefficient. Thus, assuming a nearly constant DOS for the tip in the measured region, the LDOS of the sample can be extracted normalizing the differential conductivity to the transmission coefficient. This method has been applied recently to the STS data of $p(1 \times 1)$-O/Fe and the result, taken from Ref. (43), is shown in Fig. 8.2. The STS image shows two features at $-0.5$ eV and $+0.9$ eV respectively. The physical nature of such peaks is not immediately clear. In particular, dealing with a magnetic system, it would be interesting to assign them to the minority or majority component. Although the recent development of spin polarized scanning tunneling microscopy allows such analysis, a theoretical investigation can be predictive in this sense.

In order to simulate the STS spectra we have considered the DOS of the system in the surface Brillouin zone, evaluated in the two topmost surface layers. This is reported in the upper panel of Fig. 8.3. The total DOS exhibits a peak

at +0.8 eV and a double feature at about −2 eV. Regarding the spin resolved component the former is related to the minority spin states, while the latter is due to the majority component. Although the agreement with the STS data is quite good above the Fermi level, the DOS does not give any trace of the structure at −0.5. This is probably due to the fact that this contribution is lost in the integration in the whole Brillouin zone. Indeed it is commonly recognized in literature that the STS probing method seems to be more sensitive for the states around the $\overline{\Gamma}$ point due to their slower decay in vacuum. As a consequence a better simulation of the STS data should give larger weight to the states near the centre of the SBZ. Trying to apply this concept, the integration of the DOS has been limited to 1/5 of the SBZ and the result is shown in the lower panel of Fig. 8.3. Adopting such a procedure a new feature just below the Fermi level appears which can be associated to the two peaks observed experimentally. Also in this case it is a minority spin contribution. Indeed both the two peaks observed can be associated with the to the minority component surface states near to the Fermi level, as can be seen by Fig. 8.1. The dispersion of such states is nearly flat at $\overline{\Gamma}$ while it grows near the SBZ edge, in particular for the occupied states. Thus, by integrating in the SBZ their contribution is spread over a large energy range and it is quenched. The integration in a surface restricted area instead allows to consider only the nearly flat dispersion around the SBZ centre, giving a more intense peak upon integration.

In conclusion the *ab initio* LDOS suitably integrated in the SBZ can account for the experimental findings and can also give information on the spin character of the observed features.

In the STM measurements the tip spans the sample in order to produce a real space image of the surface topology. Two operating modes are possible: constant current and constant height mode. In the first the tip is vertically adjusted in such a way that the current always stays constant. As the current is proportional to the local density of states, the tip follows a contour of a constant density of states during scanning. A kind of a topographic image of the surface is generated by recording the vertical position of the tip.

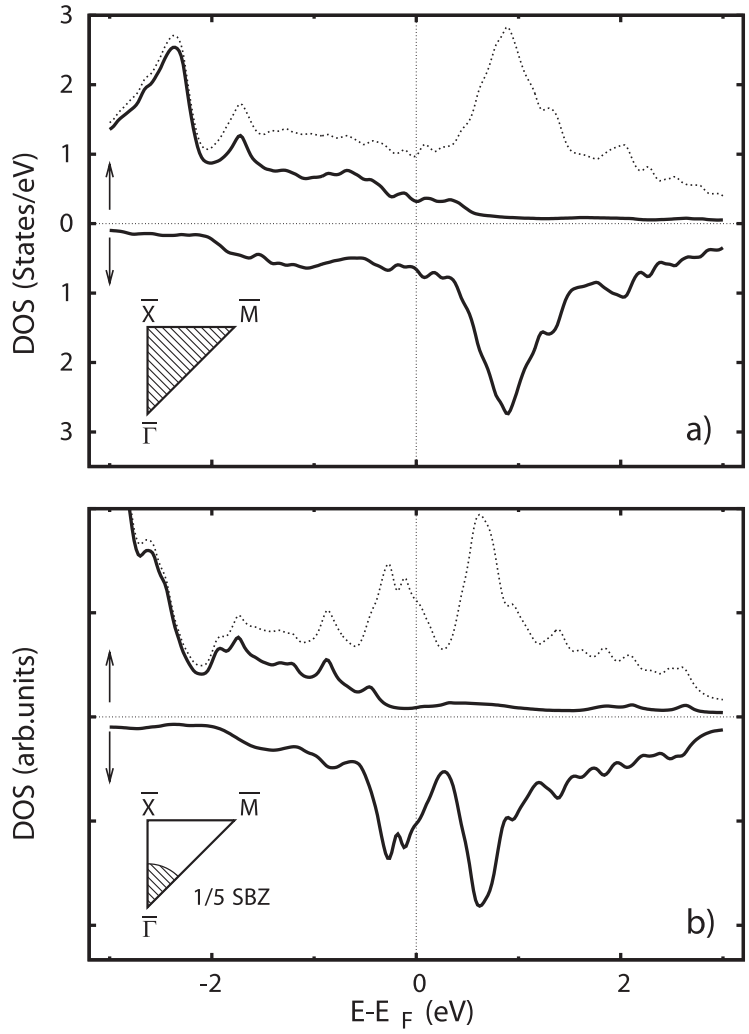


Figure 8.3: Theoretical simulation of the STS image of $p(1 \times 1)$-O/Fe(100).

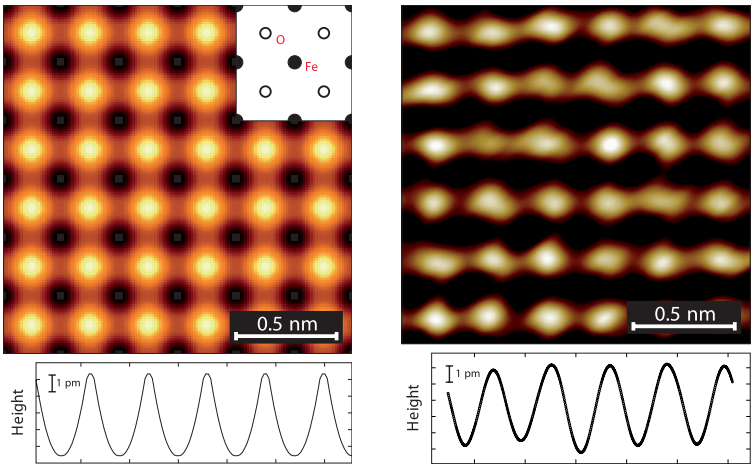


Figure 8.4: Constant current STM image of $p(1 \times 1)$-O/Fe(100) and theoretical simulation from Ref. (43)

In the constant height mode the vertical position of the tip is not changed. This mode is only appropriate for atomically flat surfaces as otherwise a tip crash would be inevitable. Among the STM disadvantages one can mention the complexity of the results interpretation for some surfaces since the surface image received in the STM investigation mode is determined not only by the surface relief but also by the density of states and by the decay of the electronic wave-functions in vacuum.

In the right panel of Fig. 8.4 is reported the constant-current STM image of the $p(1 \times 1)$-O/Fe(100) surface and the line profile along the horizontal direction across the bright spots. More details about the experimental set point can be found in Ref. (43). The assignment of the bright spots to O or Fe atoms is not obvious, being dependent both on the atomic protrusion and by the density of states at the Fermi level. A theoretical simulation can aid in this sense. In the right panel of Fig. 8.4 the simulation of constant current STM is reported. This can be obtained as a byproduct of the *ab initio* embedding calculation, evaluating the charge density, i.e. the integrated density of states, in an energy range from the Fermi level to $eV_{bias}$ (in this case $eV_{bias}$=0.1 eV). Simulating a constant current image, a cutoff value for the charge density is fixed and the constant density surfaces are plotted, that show the surface corrugation. Because

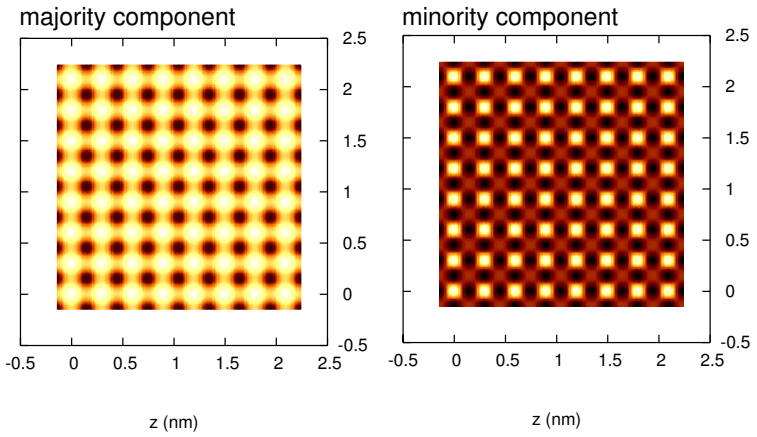


Figure 8.5: Theoretical simulation of spin-resolved STM image of $p(1 \times 1)$-O/Fe(100).

the position of the atoms in the surface cell is known and fixed as input data, the theoretical simulation allows to identify the bright spots with the oxygen atoms. This demonstrates that the geometrical aspect, i.e. the protrusion of the oxygen atoms in vacuum dominates electronic factors, i.e. the density of states at the Fermi level which is higher in the subsurface Fe atoms.

Nevertheless it has been demonstrated recently that this behaviour holds only for small distances (136).

Indeed the tip-surface distance in both the experimental and theoretical STM images shown above has been estimated of the order of 2 Å. Further experimental STM images have revealed a corrugation reversal, i.e. the inversion between bright and dark spots when the tip is at higher distances (larger than 5 Å). This evidence has been obtained using a defect as reference in the measurements. Although the theoretical simulation at larger distances is not reliable, due to the local nature of the GGA approximation used, that not allows to describe the long range behaviour of the charge density, some qualitative considerations can explain the physical nature of such corrugation reversal. The cause has to be found in what we have called previously *the electronic factor*. Indeed the electronic states at the Fermi level which are responsible for the tunneling current, display a different decay toward vacuum in front of O and Fe. In particular the

electrostatic potential that acts on the electrons outside the surface is lower in front of the Fe sites and higher on O. This is indeed due to the charge transfer from Fe to O. As a consequence the electronic wave-functions decay more slowly in front of Fe than on O and are more detectable at higher distances.

Another interesting information that can be furnished by the theoretical simulation is related to the spin character of the tunneling current. Indeed the DFT calculation treats separately the majority and minority component of the charge density so that two different images can be produced. They are reported in Fig. 8.5.

In the majority component the O atoms are imaged with brighter spots than in the minority one. In addition in the image on the right the dark spots are found along the [110] direction. In the minority component image they are along [100] and [010] directions while a local maximum is observed along the diagonal of the surface cell.

This kind of simulation has a predictive role for the spin dependent STM images that could be obtained with a spin polarized STM.

# Conclusions

Concluding this thesis work we would like to briefly summarize the step carried out in the treatment of adsorbates on metal surfaces and to make final remarks regarding the use of the embedding method to study the spectral properties of reduced symmetry systems.

In the first part of this thesis, after a general introduction on the embedding method, a theoretical framework for single adatom on metal surfaces has been presented.

The embedding approach for adsorption, already available for adatom on jellium, has been implemented for surfaces described by the modulated 1D Chulkov potential, that reproduces the experimental energy gap and the main surface states.

Within such a framework we have studied alkali adatoms on Cu(111) surface as a prototype system for adsorption, and a single Ba atom on the same surface as an example of two valence electron adatom.

The spectral properties of these systems have been characterized through the analysis of their local density of states and charge density distributions also as a function of the adsorption distance.

This first part was mainly focused on the conceptual problem of treating the single adatom adsorption from a theoretical point of view.

In this sense the embedding method represents a powerful tool because it allows us to describe an atom which is really isolated on the surface or, in other words, that interacts with a really semi-infinite solid.

The capability to describe the hybridization between atomic levels and continuous bulk bands enables the estimate of the elastic linewidth of the observed features. This is not the only advantage of the approach used in this thesis. A

further gain comes from the use of the Chulkov potential. Although this 1D potential is a quite simplified model for the surface, it accounts for the more relevant aspects of the spectral properties of single adatoms on surfaces. In particular it gives an appropriate description of the substrate band structure at $\overline{\Gamma}$ that is of primary importance for an accurate characterization of the adatom induced features.

On the other hand the lack of translational invariance upon single atom adsorption, that requires an integration on the whole surface Brillouin zone, justifies the use of a 1D potential that neglects the surface corrugation.

We have verified that the use of the Chulkov potential considerably improves the description of the spectral properties of single adatoms on metal surfaces. For example the correct reproduction of the work function allows a correct estimate of the binding energy of the atomic resonances. In addition the presence of an energy gap in the surface projected electronic structure of the substrate has notable consequences on the lifetime of the atomic resonances. The Chulkov potential allows us to consider this effect giving an elastic linewidth for the resonances that lie in the energy gap which is considerably smaller than in other approaches.

The second part of this thesis concerns to the study of overlayers on metal surfaces. Dealing with ordered bi-dimensional crystal structures the embedding implementation for realistic systems has been exploited. The electronic properties of $p(2 \times 2)$-K/Cu(111), $c(2 \times 2)$-Bi/Cu(100) and $p(1 \times 1)$-O/Fe(100) are characterized.

This second part has a more applicative aim with respect to the former. The theoretical analysis has been performed as a support of experimental findings regarding both the spectral properties of the overlayers, determined for example by AR-2PPE, and the surface topology of the studied systems. In particular for $p(2 \times 2)$-K/Cu(111) the $\mathbf{k}_{\|}$ dependence of the elastic linewidth of the overlayer features can be regarded as the most relevant result concerning this system, being strictly related to the characteristics of the method adopted. As a byproduct of the self consistent embedding calculation the Fermi surface of $c(2\times2)$-Bi/Cu(100) has been computed confirming the hypothesis of a CDW driven phase transition for this chemically modified metal surface. In addition STS and STM images of $p(1\times1)$-O/Fe(100 have been simulated in order to explain the experimental results

and then give additional information about the spin character of the recorded signals.

The theoretical analysis performed in the final chapters highlights the accuracy of the embedding approach in reproducing the experimental results and also the predictive capabilities of the method.

In conclusion this thesis work shows that an effective theoretical characterization of the electronic properties of reduced symmetry systems certainly requires a suitable description of the element responsible of the symmetry reduction (atom, overlayer, defect) but can not disregard an appropriate reproduction of the spectral properties of the underlying substrate.

# Acknowledgements

First of all I would like to acknowledge my PhD supervisor Dr. Mario Italo Trioni for his guidance, support, encouragement. In these years I have learned so much from him and it is also thanks to his efforts and suggestions that I have realized so many things during my PhD. Since we began working together, six years ago, I have been surprised by his wish of a human relationship with his co-workers. Despite the difficulties due to my work-oriented nature, I have to admit that, besides the scientific contents, I have learned much from him also in this sense.

I would like to express my gratitude to Prof. Eugeny V. Chulkov for his helpfulness and for all the interesting discussion I had the opportunity to have during my stay in San Sebastian. I would like to acknowledge also Prof. Gian Paolo Brivio and Dr. Guido Fratesi for their scientific support and suggestions during these years.

A special acknowledgments is to my husband Paolo, for his patient and lovely encouragement and to my beloved parents that have always believed in me. It is thanks to their support that I can realize myself every day.

# Appendix A

The transfer matrix technique is used to find the solution $\psi(z)$ of the unperturbed Schrödinger equation:

$$-\frac{1}{2}\frac{d^2\psi(z)}{dz^2} + V(z)\psi(z) = E\psi(z) \tag{A.1}$$

where V(z) is a periodic potential of period $a_s$ The required solution, that satisfy the Floquet-Bloch condition:

$$\psi(z + a_s) = \lambda\psi(z) \tag{A.2}$$

can be written as a linear combination of two independent solutions of A.1

$$\psi(x) = \alpha\phi_1(z) + \beta\phi_2(z) \tag{A.3}$$

where $\phi_1$ and $\phi_2$ satisfy:

$$\begin{cases} \phi_1(z + a_s) = & c_{11}\phi_1(z) + c_{12}\phi_2(z) \\ \phi_2(z + a_s) = & c_{21}\phi_1(z) + c_{22}\phi_2(z) \end{cases} \tag{A.4}$$

or in matrix notation:

$$\begin{pmatrix} \phi_1(a_s) \\ \phi_2(a_s) \end{pmatrix} = \mathbf{T}\begin{pmatrix} \phi_1(0) \\ \phi_2(0) \end{pmatrix}. \tag{A.5}$$

By choosing special boundary conditions:

$$\begin{array}{ll} \phi_1(0) = 0 & \phi_1'(0) = 1 \\ \phi_2(0) = 1 & \phi_2'(0) = 0 \end{array} \tag{A.6}$$

it is possible to relate the T-matrix coefficients to the values of the $\phi_1, \phi_2$ solutions at $a_s$:

$$\mathbf{T} = \begin{pmatrix} \phi_1(a_s) & \phi_2(a_s) \\ \phi_1'(a_s) & \phi_2'(a_s) \end{pmatrix}. \tag{A.7}$$

Applying condition A.2 to the A.3 and considering the coefficient of $\phi_1$ and $\phi_2$ on both sides one obtains:

$$\begin{aligned} \lambda\alpha &= c_{11}\alpha + c_{21}\beta \\ \lambda\beta &= c_{12}\alpha + c_{22}\beta \\ &. \end{aligned} \tag{A.8}$$

In matrix notation:

$$\begin{pmatrix} c_{11} & c_{21} \\ c_{21} & c_{22} \end{pmatrix} \begin{pmatrix} \alpha \\ \beta \end{pmatrix} = \lambda \begin{pmatrix} \alpha \\ \beta \end{pmatrix}. \tag{A.9}$$

For which there are non-trivial solution if $\det |C_{ij} - \lambda \mathbf{1}| = 0$.

Being the Wronskian $W(\phi_1, \phi_2)$ a constant quantity, the two eigenvalues $\lambda_1$ and $\lambda_2$ of the system satisfy:

$$\lambda_1 \lambda_2 = 1. \tag{A.10}$$

Combining this condition with the Floquet-Bloch solutions features the two eigenvalues can be defined as:

$$\lambda_1 = e^{ikz} \qquad \lambda_2 = e^{-ikz} \tag{A.11}$$

where $k$ is the generalized momentum.

The final step that provides the desired solution consists in determining the eigenvector $\alpha$, $\beta$ and consequently $\psi(z)$.

Being $\psi(z) = u_k(z)e^{ikz}$ one can easily obtain the $u_k(z)$ in order to decompose the logarithmic derivative in the following way:

$$G_0^{-1}(z_s, z_s, E) = ik + \left. \frac{d \log(u_k(z, E))}{dz} \right|_{z_s}. \tag{A.12}$$

# Bibliography


[1] http://mathworld.wolfram.com/Legendre-GaussQuadrature.html. 16

[2] J. Inglesfield, arXiv:1003.2282 (unpublished). 17

[3] http://mathworld.wolfram.com/IncompleteBetaFunction.html . 80

[4] S. Achilli, M. I. Trioni, E. V. Chulkov, P. M. Echenique, V. Sametoglu, N. Pontius, A. Winkelmann, A. Kubo, J. Zhao, and H. Petek. Spectral properties of Cs and Ba on Cu(111) at very low coverage: Two-photon photoemission spectroscopy and electronic structure theory. *Phys. Rev. B*, **80**, 245419, 2009. 64, 69

[5] D. L. Adler, I. R. Collins, X. Liang, S. J. Murray, G. S. Leatherman, K. D. Tsuei, E. E. Chaban, S. Chandavarkar, R. McGrath, E. D. Diehl, and P. H. Citrin. Top-site adsorption for K on Cu(111) and Ni(111) surfaces. *Phys. Rev. B*, **48**, 17445, 1993. 86

[6] P. W. Anderson. Localized magnetic states in metals. *Phys. Rev.*, **124**, 41, 1961. 30, 39

[7] D. A. Arena, F. G. Curti, and R. A. Bartinsky. Unoccupied electronic states of the Cs/Cu(100) and Cs/Cu(111) adsorption systems. *Phys. Rev. B*, **56**, 15404, 1997. 40, 83

[8] T. Aruga. Charge-density waves on metal surfaces. *J. Phys.: Condens. Matter*, **14**, 8393, 2002. 101, 108

[9] C. Baldacchini, L. Chiodo, F. Allegretti, C. Mariani, M. G. Betti, P. Monachesi, and R. del Sole. Cu(100) surface: High-resolution experimental and theoretical band mapping. *Phys. Rev. B*, **68**, 195109, 2003. 107

[10] M. Bauer, S. Pawlik, and M. Aeschlimann. Resonance lifetime and energy of an excited Cs state on Cu(111). *Phys. Rev. B*, **55**, 10040, 1997. 40, 45

[11] M. Bauer, S. Pawlik, and M. Aeschlimann. Decay dynamics of photoexcited alkali chemisorbates: Real-time investigations in the femtosecond regime. *Phys. Rev. B*, **60**, 5016, 1999. 40, 44, 47

[12] M. Bauer, S. Pawlik, R. Burgermeister, and M. Aeschlimann. Symmetry properties of an electronic alkali excitation at a noble metal surface as investigated by two-photon photoemission. *Surf. Sci.*, **402**, 62, 1998. 40

[13] G. A. Benesh and J. E. Inglesfield. An embedding approach for surface calculations. *J. Phys. C: Solid State Phys.*, **17**, 1595, 1984. 7

[14] A. J. Bennet and C. B. Duke. *Structure and Chemistry of Solid Surfaces*. Wiley, J., New York, 1969. 13

[15] A. J. Bennet and L. M. Falicov. Theory of the electronic configuration of a metallic surface-adsorbate system. *Phys. Rev.*, **151**, 512, 1966. 30, 39, 53

[16] H. P. Bonzel and A. M. Bradshaw. *Physics and chemistry of alkali metal adsorption*. Elsevier, Amsterdam, 1989. 83

[17] A. G. Borisov, J. P. Gauyacq, E.V. Chulkov, V. M. Silkin, and P. M. Echenique. Lifetime of excited electronic states at surfaces: Comparison between the alkali/Cu(111) systems. *Phys. Rev. B*, **65**, 235434, 2002. 44

[18] A. G. Borisov, A. K. Kazansky, and J. P. Gauyacq. Resonant charge transfer in ion-metal surface collisions: Effect of a projected band gap in the H/Cu(111) system. *Phys. Rev. B*, **59**, 10935, 1999. 40

[19] A. G. Borisov, A. K. Kazansky, and J. P. Gauyacq. Stabilisation of alkali-adsorbate induced states on Cu(111) surfaces. *Surf. Sci.*, **430**, 165, 1999. 41

[20] A. G. Borisov, V. Sametoglu, A. Winkelmann, A. Kubo, N. Pontius, J. Zhao, V. M. Silkin, J. P. Gauyacq, E. V. Chulkov, P. M. Echenique, and H. Petek. $\pi$ resonance of chemisorbed alkali atoms on noble metals. *Phys. Rev. Lett.*, **101**, 266801, 2008. 41

[21] J. Bormet, J. Neugebauer, and M. Scheffler. Chemical trends and bonding mechanisms for isolated adsorbates on Al(111). *Phys. Rev. B*, **49**, 17242, 1994. 38, 53, 61

[22] M. Breitholtz, V. Chis, B. Hellsing, S. Å Lindgren, and L. Wallden. Overlayer resonance and quantum well state of Cs/Cu(111) studied with angle-resolved photoemission, LEED, and first-principles calculations. *Phys. Rev. B*, **75**, 155403, 2007. 83, 92

[23] G. P. Brivio and M. I. Trioni. Adiabatic molecule-metal surface interaction. *Rev. Mod. Phys.*, **71**, 231, 1999. 30

[24] C. G. Broyden. A class of methods for solving nonlinear simultaneous set of equations. *Math. Comput.*, **16**, 577, 1965. 79

[25] G. Butti, S. Caravati, G. P. Brivio, M. I. Trioni, and H. Ishida. Image potential states and electronic structure of Na/Cu(111). *Phys. Rev. B*, **72**, 125402, 2005. 84, 95

[26] J. M. Carlsson and B. Hellsing. First-principles investigation of the quantum-well system Na on Cu(111). *Phys. Rev. B*, **61**, 13973, 2000. 83

[27] D. M. Ceperley and B. J. Alder. Ground state of the electron gas by a stochastic method. *Phys. Rev. Lett.*, **45**, 566, 1980. 13

[28] V. Chis, S. Caravati, G. Butti, M. I. Trioni, P. Cabrera-Sanfelix, A. Arnau, and B. Hellsing. Two-dimensional localization of fast electrons in p(2 × 2)-Cs/Cu(111). *Phys. Rev. B*, **76**, 153404, 2007. 83, 84, 92, 97

[29] V. Chis and B. Hellsing. Surface relaxation influenced by surface states. *Phys. Rev. Lett.*, **93**, 226103, 2004. 15

[30] S. R. Chubb and W. E. Pickett. First-principles determination of giant adsorption-induced surface relaxation in $p(1 \times 1)$-O/Fe(001). *Phys. Rev. Lett.*, **58**, 1248, 1987. 113, 114

[31] E. V. Chulkov, J. Kliewer, R. Berndt, V. M. Silkin, B. Hellsing, S. Crampin, and P.M. Echenique. Hole dynamics in a quantum-well state at Na/Cu(111). *Phys. Rev. B*, **68**, 195422, 20033. 95

[32] E. V. Chulkov, V. M. Silkin, and P. M. Echenique. Image potential states on metal surfaces: binding energies and wave functions. *Surf. Sci.*, **437**, 330, 1999. 13, 14, 17, 56

[33] A. Clarke, N. B. Brookes, P. D. Johnson, M. Weinert, B. Sinković, and N. V. Smith. Spin-polarized photoemission studies of the adsorption of O and S on Fe(001). *Phys. Rev. B*, **41**, 9659, 1990. 113

[34] C. Corriol, V. M. Silkin, D. Sanchez-Portal, A. Arnau, E. V. Chulkov, P. M. Echenique, T. M. von Hofe, J. Kliewer, J. Kröger, and R. Berndt. Role of elastic scattering in electron dynamics at ordered alkali overlayers on Cu(111). *Phys. Rev. Lett.*, **95**, 176802, 2005. 96

[35] S. Crampin. An embedding scheme for Dirac equation. *J. Phys.: Condens. Matter*, **16**, 8875, 2004. 7

[36] S. Crampin, M. Nekovee, and J. E. Inglesfield. Embedding method for confined quantum systems. *Phys. Rev. B*, **51**, 7318, 1995. 7

[37] S. Crampin, J. B. A. N. van Hoof, M. Nekovee, and J. E. Inglesfield. Full-potential embedding for surfaces and interfaces. *J. Phys.: Condens. Matter*, **4**, 1475, 1992. 7, 75, 76

[38] O. R. Davies and J. E. Inglesfield. Electronic structure and conductance of large molecules and DNA. *Prog. Surf. Sci.*, **74**, 161, 2004. 7

[39] O. R. Davies and J. E. Inglesfield. Embedding method for conductance of DNA. *Phys. Rev. B*, **69**, 195110, 2004. 7

[40] F. Delamare and G. E. Rhead. First stages of the deposition of bismuth on copper examined by LEED: I. the (100) substrate. *Surf. Sci.*, **35**, 172, 1973. 101

[41] R. D. Diehl and R. McGrath. Current progress in understanding alkali metal adsorption on metal surfaces. *J. Phys.: Condens. Matter*, **9**, 951, 1997. 83

[42] K. Doll. Density functional study of the adsorption of K on the Cu(111) surface. *Eur. Phys. J. B.*, **22**, 389, 2001. 86

[43] F. Donati, P. Sessi, S. Achilli, A. Li Bassi, M. Passoni, C. S. Casari, C. E. Bottani, A. Brambilla, A. Picone, L. Finazzi, M. ando Duó, M. I. Trioni, and F. Ciccacci. Scanning tunneling spectroscopy of the Fe(001)-$p(1 \times 1)$O surface. *Phys. Rev. B*, **79**, 195430, 2009. 118, 121

[44] P. M. Echenique, R. Berndt, E. V. Chulkov, Th. Fauster, A. Goldmann, and U. Höfer. Decay of electronic excitations at metal surfaces. *Surf. Sci. Rep.*, **52**, 219, 2004. 14, 95

[45] P. M. Echenique and J. B. Pendry. The existence and detection of Rydberg states at surfaces. *J. Phys. C: Solid State Phys.*, **11**, 2065, 1978. 18

[46] V. A. Ermoshin and A. K. Kazansky. Wave packet study of $H^-$ decay in front of a metal surface. *Phys. Rev. Lett. A*, **218**, 99, 1996. 40

[47] W. C. Fan and A. Ignatiev. Growth of an orientationally ordered incommensurate potassium overlayer and its order-disorder transition on the cu(111). *Phys. Rev. B*, **37**, 5274, 1988. 84, 85

[48] U. Fano. Effects of configuration interaction on intensities and phase shifts. *Phys. Rev.*, **124**, 1866, 1961. 39

[49] N. Fischer, S. Shuppler, Th. Fauster, and W. Steinmann. Coverage-dependent electronic structure of Na on Cu(111). *Surf. Sci.*, **314**, 89, 1994. 40, 83, 85, 90

[50] N. Fischer, S. Shuppler, R. Fischer, Th. Fauster, and W. Steinmann. Image states and the proper work function for a single layer of Na and K on Cu(111), Co(0001), and Fe(110). *Phys. Rev. B*, **47**, 4705, 1993. 97, 98

[51] A. J. Fisher. Methods of embedding for defect and surface problems. *J. Phys. C: Solid State Phys.*, **21**, 3229, 1988. 7

[52] A. J. Fisher. A modified form for the real-space embedding potential. *J. Phys.: Condens. Matter*, **2**, 6079, 1990. 7

[53] P. Fouquet and G. Witte. Observation of metallization transition of 2D alkali metal films. *Phys. Rev. Lett.*, **83**, 360, 1999. 38

[54] J. W. Gadzuk. Resonance-assisted, hot-electron-induced desorption. *Surf. Sci.*, **342**, 345, 1995. 40

[55] J. W. Gadzuk. Simple connections in alkali adsorption. *Phys. Rev. B*, **79**, 073411, 2009. 40

[56] J. W. Gadzuk, J. K. Hartman, and T. N. Rhodin. Approach to alkali-metal chemisorption within the Anderson model. *Phys. Rev. B*, **4**, 241, 1971. 39

[57] F. García-Moliner and J. Rubio. A new method in the quantum theory of surface states. *J. Phys. C: Solid State Phys.*, **2**, 1789, 1969. 32

[58] P. Gargiani, M. G. Izzo, F. Bussolotti, M. G. Betti, S. Achilli, and M. Trioni. Bi ordered phases on Cu(100): periodic arrays of dislocations influence the electronic properties. *J. Chem Phys.*, **132**, 174706, 2010. 102, 106

[59] J. P. Gauyacq, A. G. Borisov, and M. Bauer. Excited states in the alkali/noble metal surface systems: A model system to study of charge transfer dynamics at surfaces. *Progr. Surf. Sci.*, **82**, 244, 2007. 40, 41, 47

[60] J. P. Gauyacq, A. G. Borisov, and A. K. Kazansky. Impurity-induced localisation of the 2D surface-state continuum on a metal surface. *Appl. Phys. A*, **78**, 141, 2004. 43

[61] R. Gomer and L. W. Swanson. Field desorption of carbon monoxide from tungsten. *J. Chem. Phys.*, **39**, 2813, 1963. 30

[62] T. B. Grimley. Overlap effects in the theory of adsorption using Anderson's hamiltonian. *J. Phys. C: Solid State Phys.*, **3**, 1934, 1970. 39

[63] T. B. Grimley and C. Pisani. Chemisorption theory in the Hartree-Fock approximation. *J. Phys. C: Solid State Phys.*, **7**, 2831, 1974. 30

[64] O. Gunnarson, H. Hjelmberg, and B. I. Lundqvist. Binding energies for different adsorption sites of hydrogen on simple metals. *Phys. Rev. Lett.*, **37**, 292, 1976. 30

[65] O. Gunnarson and B. I. Lundquist. Exchange and correlation in atoms, molecules, and solids by the spin-density-functional formalism. *Phys. Rev. B*, **13**, 4274, 1976. 79

[66] R. W. Gurney. Theory of electrical double layers in adsorbed films. *Phys. Rev.*, **47**, 479, 1935. 30, 38

[67] D. Heskett, K.-H. Frank, E. E. Koch, and H.-J. Freund. Unoccupied electron band structure of Na overlayers on Al(111). *Phys. Rev. B*, **36**, 1276, 1987. 37

[68] T. Hirahara, T. Nagao, I. Matsuda, G. Bihlmayer, E. V. Chulkov, Yu. M. Koroteev, and S. Hasegawa. Quantum well states in ultrathin Bi films: Angle-resolved photoemission spectroscopy and first-principles calculations study. *Phys. Rev. B*, **75**, 035422, 2007. 101

[69] H. Hjelmberg, O. Gunnarson, and B. I. Lundqvist. Theoretical studies of atomic adsorption on nearly-free-electron-metal surfaces. *Surf. Sci.*, **68**, 158, 1977. 30

[70] G. Hoffmann, R. Berndt, and P. Johansson. Two-electron photon emission from metallic quantum wells. *Phys. Rev. Lett.*, **90**, 046803, 2003. 83

[71] Ph. Hofmann. The surfaces of bismuth: Structural and electronic properties. *Prog. Surf. Sci.*, **81**, 191, 2006. 101

[72] P. Hohenberg and W. Kohn. Inhomogeneous electron gas. *Phys. Rev.*, **136**, B864, 1964. 8

[73] A. Hohlfeld, M. Sunjic, and K. Horn. Electronic structure of cesium adsorbed on Al(111). *J. Vac. Sci. Technol. A: Vacuum, Surfaces, and Films*, **5**, 679, 1987. 37

[74] J. E. Inglesfield. Green functions, surfaces, and impurities. *J. Phys. C: Solid State Phys.*, **4**, L14, 1971. 32

[75] J. E. Inglesfield. Electronic structure of interstitial H in Cu. *J. Phys. F: Metal Phys.*, **11**, L287, 1981. 7

[76] J. E. Inglesfield. A method of embedding. *J. Phys. C: Solid State Phys.*, **14**, 3795, 1981. 7

[77] J. E. Inglesfield. The embedding method for electromagnetics. *J. Phys. A: Math. Gen.*, **31**, 8495, 1998. 7

[78] J. E. Inglesfield. Embedding at surfaces. *Comp. Phys. Comm.*, **137**, 89, 2001. 8

[79] J. E. Inglesfield, S. Crampin, and H. Ishida. Embedding potential definition of channel functions. *Phys. Rev. B*, **71**, 155120, 2005. 7

[80] H. Ishida. Electronic structure of alkali-metal overlayers on the semi-infinite jellium surface. *Phys. Rev. B*, **39**, 5492, 1988. 13, 39

[81] H. Ishida. Theory of the alkali-metal chemisorption on metal surfaces. *Phys. Rev. B*, **38**, 8006, 1988. 13, 53, 83

[82] H. Ishida. Surface-embedded green function calculation using non-local pseudopotentials. *Surf. Sci.*, **388**, 71, 1997. 7

[83] H. Ishida. Surface-embedded green-function method: A formulation using a linearized-augmented-plane-wave basis set. *Phys. Rev. B*, **63**, 165409, 2001. 7, 76

[84] H. Ishida. Embedded green-function calculation of the conductance of oxygen-incorporated Au and Ag monatomic wires. *Phys. Rev. B*, **75**, 205419, 2007. 7

[85] H. Ishida and A. Liebsch. Static and quasistatic response of Ag surfaces to a uniform electric field. *Phys. Rev. B*, **66**, 155413, 2002. 80

[86] H. Ishida and M. I. Trioni. Comparison of the embedding and Dyson-equation methods in the Green's-function calculation of a defect in solids. *Phys. Rev. B*, **63**, 155108, 2001. 7

[87] Bardeen J. Theory of the work function. *Phys. Rev.*, **490**, 653, 1936. 13

[88] W. Jacob, E. Bertel, and V. Dose. Potassium-induced empty electronic states on Ag(110). *Phys. Rev. B*, **35**, 5910, 1987. 39

[89] J. F. Janak, A. R. Williams, and V. L. Moruzzi. Local exchange-correlation potentials and the fermi surface of copper. *Phys. Rev. B*, **6**, 4367, 1972. 79

[90] T. Kan, K. Mitsukawa, T. Ueyama, M. Takada, T. Yasue, and T. Koshikawa. Secondary ion emission processes of sputtered alkali ions from alkali/Si(100) and Si(111). *Surf. Sci.*, **460**, 214, 2000. 37

[91] R. Kemp and J. E. Inglesfield. Embedding approach for rapid convergence of plane waves in photonic calculations. *Phys. Rev. B*, **65**, 115103, 2002. 7

[92] S. D. Kevan. Evidence for a new broadening mechanism in angle-resolved photoemission from Cu(111). *Phys. Rev. Lett.*, **50**, 526, 2001. 90

[93] K. H. Kingdon and I. Langmuir. *Phys. Rev.*, **21**, 380, 1923. 37

[94] W. Kohn and L. J. Sham. Self-consistent equations including exchange and correlation effects. *Phys. Rev.*, **140**, A1133, 1965. 8

[95] N. D. Lang. Self consisten properties of the electron distribution at a metal surface. *Solid State Comm.*, **7**, 1047, 1969. 13

[96] N. D. Lang. Theory of work-function changes induced by submonolayer alkali adsorption. *Solid State Comm.*, **9**, 1015, 1971. 13

[97] N. D. Lang and W. Kohn. Theory of metal surfaces: charge density and surface energy. *Phys. Rev. B*, **1**, 4555, 1970. 13

[98] N. D. Lang and W. Kohn. Surface-dipole barriers in simple metals. *Phys. Rev. B*, **8**, 4234, 1971. 13

[99] N. D. Lang and W. Kohn. Theory of metal surfaces: Induced surface charge and image potential. *Phys. Rev. B*, **7**, 3541, 1973. 81

[100] N. D. Lang and W. Kohn. Theory of work-function changes induced by alkali adsorption. *Phys. Rev. B*, **4**, 6010, 1973. 13

[101] N. D. Lang and A. R. Williams. Self-consistent theory of the chemisorp- tion of H, Li, and O on a metal surface. *Phys. Rev. Lett.*, **34**, 531, 1975. 13

[102] N. D. Lang and A. R. Williams. Chemical trends in atomic adsorption on simple metals. *Phys. Rev. Lett.*, **37**, 212, 1976. 13, 30

[103] N. D. Lang and A. R. Williams. Theory of atomic chemisorption on simple metals. *Phys. Rev. B*, **18**, 616, 1978. 13, 30, 38, 39

[104] K. O. Legg, F. Jona, D. W. Jepsen, and P. M. Marcus. Early stages of oxidation of the Fe001 surface: Atomic structure of the first monolayer. *Phys. Rev. B*, **16**, 5271, 1977. 113

[105] L. Limot, E. Pehlke, J. Kröger, and R. Berndt. Surface-state localization at adatoms. *Phys. Rev. Lett.*, **94**, 036805, 2005. 43

[106] S. Å Lindgren and L. Wallden. Discrete valence-electron states for Na overlayers on Cu(111). *Phys. Rev. B*, **38**, 3060, 1988. 83

[107] H. L. Meyerheim, M. De Santis, W. Moritz, and I. K. Robinson. Domain-wall interactions in Bi/Cu(001). *Surf. Sci.*, **418**, 295, 1998. 101, 102

[108] H. L. Meyerheim, H. Zajonz, W. Moritz, and I. K. Robinson. Surface alloying and dealloying in Bi/Cu(001) at low coverage. *Surf. Sci.*, **381**, L551, 1997. 101, 102

[109] M. Milun, P. Pervan, and D. P. Woodruff. Quantum well states in thin metal films: simple model physics in reality? *Rep. Prog. Phys.*, **65**, 99, 2002. 95

[110] J. P. Muscat and D. M. Newns. Valence electronic structure of alkalis adsorbed on free-electron like and transition metals. *Surf. Sci.*, **74**, 355, 1977. 40

[111] J. P. Muscat and D. M. Newns. Electronic structure of adsorbed alkali atoms for comparison with UPS data. *Surf. Sci.*, **84**, 262, 1978. 40, 45

[112] T. Nakagawa, G. I. Boishin, H. Fujioka, H. W. Yeom, I. Matsuda, N. Takagi, M. Nishijima, and T. Aruga. Fermi surface nesting

and structural transition on a metal surface: In /Cu(001). *Phys. Rev. Lett.*, **86**, 854, 2001. 101, 107, 108

[113] M. Nekovee and J. E. Inglesfield. Threshold behaviour of surface density of states at the vacuum level. *Europhys. Lett.*, **19**, 535, 1992. 80

[114] M. Nekovee and J. E. Inglesfield. Theory of image states at magnetic surfaces. *Progr. Surf. Sci.*, **50**, 149, 1996. 80

[115] D. M. Newns. Self-consistent model of hydrogen chemisorption. *Phys. Rev.*, **178**, 1123, 1969. 30, 37

[116] K. Niedfeldt, E. A. Carter, and P. Nordlander. Influence of surface band gaps on the lifetimes of charge transfer states. *Surf. Sci.*, **600**, L291, 2006. 48

[117] H. B. Nielsen and W. Thowladda. Position and linewidth of the K-induced 4*s* resonance on Ag(100): a two-photon photoemission study. *Surf. Sci. Lett.*, **284**, L426, 1993. 44, 45

[118] A. Nilsson, L. Pettersson, and J. K. Norskov. *Chemical bonding at surfaces and interfaces*. Elsevier, Amsterdam, 2007. 30

[119] P. Nordlander and J. C. Tully. Energy shift and broadening of atomic levels near metal surfaces. *Phys. Rev. B*, **42**, 5564, 1990. 39, 45

[120] J. K. Norskov. Chemisorption on metal surfaces. *Rep. Prog. Phys.*, **53**, 1253, 1990. 29

[121] E. M. Oelling and R. Miranda. New experimental studies on the adsorption of K on Si(100) and Si(111). *Surf. Sci.*, **177**, L947, 1986. 37

[122] S. Ogawa, H. Nagano, and H. Petek. Phase and energy relaxation in an antibonding surface state: Cs/Cu(111). *Phys. Rev. Lett.*, **82**, 1931, 1999. 40

[123] G. Pacchioni and P. S. Bagus. Alkali adsorbates on metal surfaces: observable consequences of the ionic K/Cu(100) interaction. *Surf. Sci.*, **286**, 317, 1993. 53, 54, 83

[124] L. Padilla-Campos and Toro-Labbé. Monte carlo simulations of the adsorption of potassium on a Cu(111) surface. *J. Chem. Phys.*, **108**, 6458, 1998. 86

[125] L. Padilla-Campos, A. Toro-Labbé, and J. Maruani. Theoretical investigation of the adsorption of alkali metals on a Cu(111) surface. *Surf. Sci.*, **385**, 24, 1997. 86

[126] I. Panas, J. Schüle, P. E. M. Siegbah, and U. Wahlgren. On the cluster convergence of chemisorption energies. *Chem. Phys. Lett.*, **149**, 265, 1988. 31

[127] C. A. Papageorgopoulos. Studies of separate adsorption and coadsorption of Cs and$O_2$ on Cu(100). *Phys. Rev. B*, **25**, 3740, 1982. 37

[128] R. G. Parr and W. Yang. *Density-Functional Theory of Atoms and Molecules*. Oxford University Press, Oxford, 1994. 13

[129] M. Passoni, F. Donati, A. Li Bassi, C. S. Casari, and C. E. Bottani. Recovery of local density of states using scanning tunneling spectroscopy. *Phys. Rev. B*, **79**, 045404, 2009. 118

[130] J. Paul. Alkali overlayers on aluminum, alumina, and aluminum carbide. *J. Vac. Sci. Technol. A: Vacuum, Surfaces, and Films*, **5**, 664, 1987. 37

[131] R. E. Peierls. *Quantum Theory of solids*. Clarendon, Oxford, 1955. 101, 108

[132] J. P. Perdew, K. Burke, and M. Ernzerhof. Generalized gradient approximation made simple. *Phys. Rev. Lett.*, **77**, 3865, May 1996. 79

[133] J. P. Perdew, E. R. McMullen, and A. Zunger. Density-functional theory of the correlation energy in atoms and ions: A simple analytic model and a challenge. *Phys. Rev. A*, **23**, 2785, 1981. 13, 79

[134] J. P. Perdew and Y. Wang. Accurate and simple analytic representation of the electron-gas correlation energy. *Phys. Rev. B*, **45**, 13442, 1992. 79

[135] H. Petek, H. Nagano, M. J. Weida, and S. Ogawa. Surface femtochemistry: Frustrated desorption of alkali atoms from noble metals. *J. Phys. Chem. B*, **105**, 6767, 2001. 40

[136] A. Picone, G. Fratesi, A. Brambilla, P. Sessi, F. Donati, S. Achilli, L. Maini, M. I. Trioni, C. S. Casari, M. Passoni, A. Li Bassi, M. Finazzi, L. Duò, and F. Ciccacci. Atomic corrugation in scanning tunneling microscopy images of the Fe(001)-$p(1 \times 1)$O surface. *Phys. Rev. B*, **81**, 115450, 2010. 122

[137] D. Pines. *Elementary Excitations in Solids.* Benjamin, New York, 1964. 108

[138] A. J. Sargood, C. W. Jowett, and A. J. Hopkins. A relationship between surface potential and electronegativity for adsorption on tungsten single crystals. *Surf. Sci.*, **22**, 343, 1970. 64

[139] J. Schäfer, D. Schrupp, E. Rotenberg, S. D. Kevan, and R. Claessen. Electronic interactions and phase transitions at surfaces and in low dimensions. *Appl. Phys. A*, **80**, 965, 2005. 108

[140] M. Scheffler, Ch. Droste, A. Fleszar, F. Máca, G. Wachutka, and G. Barzel. A self-consistent surface-green function (SSGF) method. *Physica B*, **172**, 143, 1991. 29, 38, 55, 60

[141] F. Schiller, M. Corso, M. Urdanpilleta, T. Ohta, A. Bostwick, J. L. McChesney, E. Rotenberg, and E. Ortega. Quantum well and resonance-band split off in a K monolayer on Cu(111). *Phys. Rev. B*, **77**, 153410, 2008. 84, 85, 90, 92, 95, 96, 98

[142] P. E. M. Siegbah, L. G. M. Petterson, and U. Wahlgren. A theoretical study of atomic fluorine chemisorption on the Ni(100) surface. *J. Chem. Phys.*, **94**, 4024, 1991. 31

[143] B. Simon. The bound state of weakly coupled Schrödinger operators in one and two dimensions. *Ann. Phys.*, **97**, 279, 1976. 43

[144] D. J. Singh. *Planewaves, pseudopotentials and the LAPW method*. Kluwer Academic Publishers, Boston, 1994. 78

[145] G. A. Somorjai. *Introduction to surface chemistry and catalysis*. Wiley, New York, 1994. 113

[146] C. Stampfl and M. Scheffler. Theory of alkali-metal adsorption on close-packed metal-surfaces. *Surf. Rev. Lett.*, **2**, 317, 1995. 83

[147] J. Stoer and R. Bulirsch. *Introduction to Numerical Analysis*. Springer-Verlag, New York, 1980. 42

[148] K. Swamy, A. Menzel, R. Beer, and E. Bertel. Charge-density waves in self-assembled halogen-bridged metal chains. *Phys. Rev. Lett.*, **86**, 1299, 2001. 107

[149] D. Tang and D. Heskett. Unoccupied electronic structure of Na/Ni(111). *Phys. Rev. B*, **47**, 10695, 1993. 40, 44

[150] J. B. Taylor and I. Langmuir. The evaporation of atoms, ions and electrons from caesium films on tungsten. *Phys. Rev.*, **44**, 423, 1933. 37

[151] G. te Velde and E. J. Baerends. Slab versus cluster approach for chemisorption studies. CO on Cu (100). *Chem. Phys.*, **177**, 399, 1993. 31

[152] D. Teillet-Billy and J. P. Gauyacq. Position and width of a negative ion state in front of a surface: formation of $C^-(^4S)$ ions by electron capture. *Surf. Sci.*, **239**, 343, 1990. 40

[153] G. S. Tompa, M. Seidl, W. C. Ermler, and W. E. Carr. Work function of cesium-covered polycrystalline beryllium. *Surf. Sci.*, **185**, L453, 1987. 37

[154] M. I. Trioni, G. P. Brivio, S. Crampin, and J. E. Inglesfield. Embedding approach to the isolated adsorbate. *Phys. Rev. B*, **53**, 8052, 1996. 30, 33

[155] Vladimir A. Ukraintsev. Data evaluation technique for electron-tunneling spectroscopy. *Phys. Rev. B*, **53**, 11176, 1996. 117

[156] C. A. F. Vaz, J. A. C. Bland, and G. Lauhoff. Magnetism in ultrathin film structures. *Rep. Prog. Phys.*, **71**, 056501, 2008. 113

[157] U. Von Barth and L. Hedin. A local exchange-correlation potential for the spin polarized case. *J. Phys. C: Solid State Phys.*, **5**, 1629, 1972. 79

[158] G. K. Wertheim, D. M. Riffe, and P. H. Citrin. Nature of the charge localized between alkali adatoms and metal substrates. *Phys. Rev. B*, **49**, 4834, 1993. 53

[159] J. A. Wilson. Bands, bonds, and charge-density waves in the $NbSe_3$ family of compounds. *Phys. Rev. B*, **19**, 6456, 1979. 108

[160] E. Wimmer. All-electron local density functional study of metallic monolayers: I. alkali metals. *J. Phys. F: Metal Phys.*, **13**, 2313, 1983. 93

[161] D. Wortmann, H. Ishida, and S. Blügel. Embedded green-function approach to the ballistic electron transport through an interface. *Phys. Rev. B*, **66**, 075113, 2002. 7

[162] D. Wortmann, H. Ishida, and S. Blügel. *Ab initio* green-function formulation of the transfer matrix: Application to complex band structures. *Phys. Rev. B*, **65**, 165103, 2002. 7, 76, 78

[163] P. Wynblatt, D. Chatain, and A. Ranguis. STM study of Bi-on-Cu(100). *Surf. Sci.*, **601**, 1623, 2007. 101

[164] Y. Yamada, K.-H. Rieder, and W. Theis. Surface phase transition in H/W(110) induced by tuning the fermi surface nesting vector by hydrogen loading. *Phys. Rev. Lett.*, **99**, 196105, 2007. 108

[165] S. Yamamoto. Fundamental physics of vacuum electron sources. *Rep. Prog. Phys.*, **69**, 181, 2006. 64

[166] J. Zhao, N. Pontius, A. Winkelmann, V. Sametoglu, A. Kubo, A. G. Borisov, D. Sánchez-Portal, V. M. Silkin, E. V. Chulkov, P. M. Echenique, and H. Petek. Electronic potential of a chemisorption interface. *Phys. Rev. B*, **78**, 085419, 2008. 40, 41, 43, 44

[167] M. Ziegler, J. Kröger, R. Berndt, A. G. Borisov, and J. P. Gauyacq. Linewidth of a cesium adatom resonance on Ag(111). *Phys. Rev. B*, **79**, 075401, 2009. 45